Inner Cassini States of the Moon, and their Implications for a Mechanically Generated Dynamo

By

Christopher P. Stys

A thesis submitted in partial fulfillment of the requirements for the degree of

Master of Science

in

Geophysics

Department of Physics
University of Alberta

Abstract

We present a model of the precession dynamics of the Moon that comprises a fluid outer core and a solid inner core. We show that three Cassini states associated with the inner core exist. The tilt angle of the inner core in each of these states is determined by the ratio between the free inner core nutation frequency (ω_{ficn}) and the precession frequency $\Omega_p = 2\pi/18.6$ yr $^{-1}$. All three Cassini states are possible if $|\omega_{ficn}| > 2\pi/16.4$ yr $^{-1}$, but only one is possible otherwise. Assuming that the lowest energy state is favoured, this transition marks a discontinuity in the tilt angle of the inner core, transiting from $-33°$ to $17°$ as measured with respect to the mantle figure axis, where negative angles indicate a tilt towards the orbit normal. Possible Lunar interior density structures cover a range of ω_{ficn}, from approximately half to twice as large as Ω_p, so the precise tilt angle of the inner core remains unknown, though it is likely large because Ω_p is within the resonant band of ω_{ficn}. Adopting one specific density model, we suggest an inner core tilt of approximately $-17°$. Viscoelastic deformations within the inner core and melt and growth at the surface of a tilted inner core, both neglected in our model, should reduce this amplitude. If the inner core is larger than approximately 200 km, it may contribute by as much as a few thousandths of a degree on the observed mantle precession angle of $1.543°$.

A natural extension of our Cassini state model is to investigate the impact of the rotational dynamics of the Lunar interior on the generation of an ancient Lunar magnetic field. Purely thermally driven convective dynamo models have had a difficult time explaining the paleomagnetic intensities recorded in Lunar rocks. Mechanical stirring from differential rotation at the core mantle boundary (CMB) and inner core boundary (ICB) can generate large viscous dissipation, potentially sufficiently large in the Lunar past to have powered a dynamo. We present estimates of the paleomagnetic field intensities B_{cmb} and B_{icb} based on dynamos associated with viscous dissipation at the CMB and ICB, respectively. We show that B_{cmb} may have been larger than 25 μT early in Lunar history, although the dynamo would have shut off around 3.9 Gyr ago. We also show that

the inner core radius must be larger than approximately 100 km for viscous dissipation at the ICB to be above the dynamo threshold. B_{icb} can be as large as approximately 8.5 μT, weaker than B_{cmb}, but a dynamo from dissipation at the ICB may have persisted until very recently.

Preface

Chapter 2 along with appendix A and B have been published as Stys, C., & Dumberry, M., "The Cassini state of the Moon's inner core", Journal of geophysical research, volume 123, 2868-2892, 2018. I was responsible for the construction of our computer model, generation of data as well as helping with the manuscript composition.

Acknowledgments

I would like to thank my parents, Erika, Julian and Luke for their unwavering support, and Professor Dumberry for his constant guidance, patience and mentorship over the past three years.

Contents

List of Tables

List of Figures

Chapter 1

Introduction

Being our closest celestial neighbour, the study of the Moon began thousands of years ago, but it wasn't until the arrival of the space age that high precision observations of the Moon could be taken. Satellite missions starting in 1959 have revealed an abundance of data far beyond observations made from Earth, with even more being discovered through the manned missions to the Moon beginning in 1969. Retroreflector arrays placed on the surface allowed for centimetre accuracy in measurements of the orientation and motions of the Lunar surface, and along with dozens of other instruments, has allowed us to study the Moon like never before.

Despite the wealth of knowledge now available, certain aspects of the Moon and its past are still ambiguous. Many different models of the Lunar interior exist, with varying fluid outer core radii and densities. The presence of a solid inner core has also been detected although its existence is still under dispute. The rotational dynamics of these interior structures cannot be measured directly and instead are left to mathematical modelling. The ancient Lunar magnetic field has also been a point of contention. Most conventional dynamo mechanisms have failed to explain either the magnitude or the longevity seen in the paleomagnetic observations. Many other uncertainties involving the Moon and its history exist, but for this study we will focus mainly on the ones mentioned above. We will develop a model in order to calculate the rotational dynamics of the Moon and its interior given a wide range of Lunar parameters. An extension of this model into the past allows us to investigate alternate processes that could have theoretically led to dynamo generation and hopefully provide insight into the uncertain ancient Lunar magnetic field.

1.1 Exploration of the Moon

Prior to space travel all observations of our celestial neighbourhood were made using ground based methods. The arrival of the space age introduced new methods of data acquisition. We were now able to gather much higher quality data of our closest celestial neighbour with the use of Lunar orbiters and probes [*Heiken et al.*, 1991]. Unhindered by interference of the Earth's atmosphere, these probes yielded clearer photographs of the Lunar surface at higher resolutions. In addition to superior image quality, the use of complex instrumentation provided bountiful new data beyond simple photography. Luna 10 was the first spacecraft to map the chemical composition of the Moon from orbit, with many more spacecraft in the later months of 1966 measuring selenodesy, radiation environment and soil mechanics. The year of 1966 was concluded by Luna 13 returning the first analysis from soil samples after making a successful soft landing on the Lunar surface.

The following years leading up to 1969 were dominated by the Lunar Orbiter program, a series of 5 unmanned spacecraft sent to the Moon with the purpose of mapping potential landing sites in preparation for the future manned Apollo missions. Photographic measurements were made of both sides of the Moon with resolutions of 60 m or better [*Heiken et al.*, 1991]. In conjunction with photographs, observations of the Lunar radiation environment as well as selenodesy and meteoroids were also made to affirm that space travel to the Moon was indeed a possibility.

Through 1969 to 1972, six manned Apollo missions were launched with each subsequent mission revealing more about the Lunar environment and providing insightful evidence into the Lunar past. The Apollo Lunar Surface Experiment Package (ALSEP) described a collection of scientific instruments used by the Apollo missions which relayed detailed measurements of various Lunar phenomena and properties back to Earth. ALSEP contained several scientific instruments such as seismometers, retroreflector arrays, charged particle flux detectors, atmospheric composition and pressure detectors, thermal subsurface devices, gravimeter, magnetometer and solar wind spectrometer instruments. It was placed by the astronauts at the landing site of each respective mission, excluding Apollo 11 which contained a smaller package with fewer instruments. Most of the ALSEP experiments were shut off by September 30th, 1977 primarily due to budget restrictions, however the retroreflector arrays are still in use today in measurements of Lunar motions [*Dickey et al.*, 1994]. In total, the Apollo missions returned 381.7 kg of samples from the Moon, and an abundance of measurements of the Lunar environment for years to come.

Since 1972 there have been a few dozen satellite missions to the Moon, though none

have been manned since Apollo 17. Nevertheless, valuable data has been acquired from these missions, the most recent and notable of which were the Gravity Recovery and Interior Laboratory (GRAIL) which produced a high quality mapping of the Moon's gravitational field (2011-2012), the Lunar Atmosphere and Dust Environment Explorer (LADEE), purposed with studying the Lunar exosphere (2013) in addition to a few Chinese lead missions. While the frequency of Lunar missions has decreased over the last few decades, plans for many more are underway in the near future.

1.2 Lunar history

The origin of the Moon is still a highly debated subject, however one consensus is ubiquitous: the moon had a violent and energetic birth. The first postulate of the Moon's origin, conceived by *Darwin* [1879], describes the Moon as a product of fission from a larger body. A rapidly spinning primordial Earth could create centrifugal forces large enough to counteract gravitational forces at its equator. Through the help from resonant amplification from the tidal forcing of the sun and rotational instabilities of the Earth resulting from either its atmosphere or core [*Cameron and Marsden*, 1966], a large mass could have separated from the resulting equatorial bulge. This hypothesis quickly began to raise suspicion as *Chamberlin and Moulton* [1909] showed the insufficient angular momentum available to cause such a dramatic chain of events, with Earth currently possessing only 10-20% of the required angular momentum to form the Jacobian ellipsoid resulting in fission. A further study done by *Jeffreys* [1930] suggested that the tidal bulge would be damped by internal friction, which further demonstrated that while most qualitative features of the Moon could be explained by this hypothesis, there was more to the birth of the Moon than the simple fission hypothesis.

A more modern version of the fission hypothesis was proposed by *Wise* [1963] which states that a homogeneous proto-Earth could have reached supercritical rotation when gravitational differentiation of the body occurred (Fig. 1.1). As the heavier elements coalesced to the centre, the moment of inertia would have decreased thereby increasing the rotation rate. However the fission hypothesis in general is still regarded with prudence as it does not address its most significant pitfall of insufficient angular momentum.

Decades after Darwin proposed his widely popular theory, alternate hypotheses began to surface. Amongst these, the two predominant ones suggest that either the Moon formed along side the Earth as a sister planet or was gravitationally trapped from somewhere else in the solar system. Although seemingly plausible, each of these classical hypotheses fall short of explaining a few key abnormalities. First, the lack of iron present in the
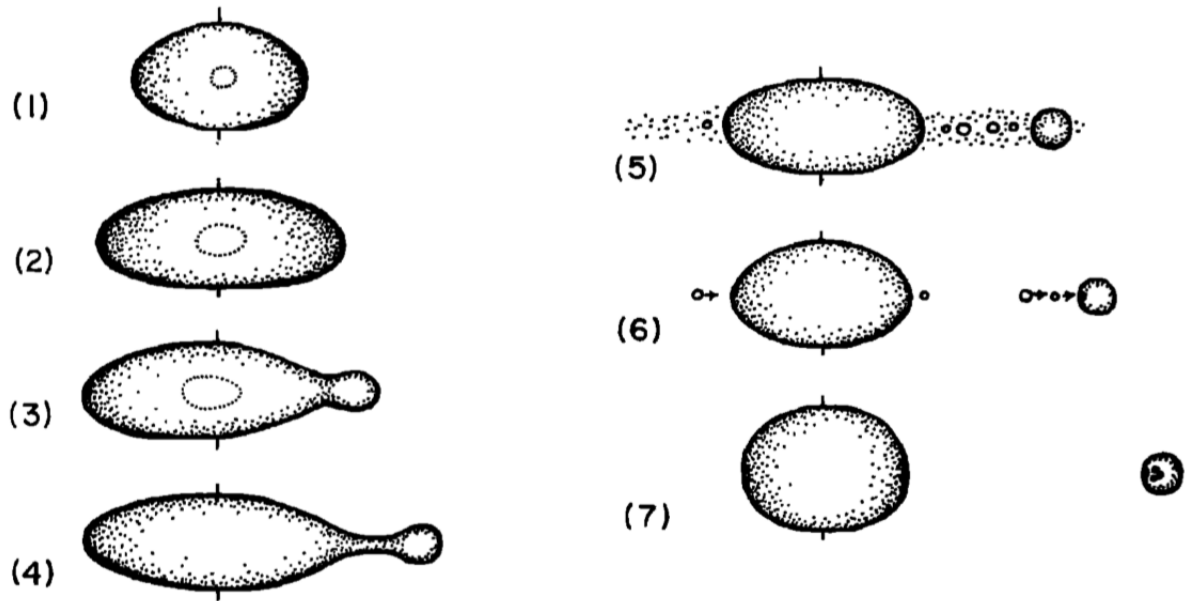
Figure 1.1: Sequence of events leading to Moon formation through fission from a larger proto-Earth. From *Wise* [1963].

Lunar rock suggests that it did not form alongside the Earth as a separate body since this would not explain the striking similarity of the Moon to that of the Earth's mantle. Secondly, the probability of a body as large as the Moon getting trapped in a stable orbit around a relatively small body such as the Earth is rather low [*Hartmann and Davis*, 1975].

The most widely accepted hypothesis today involves an impact scenario. A collision between a large body, approximately the size of Mars, and the proto-Earth could have created enough ejecta in order to accrete as a satellite around the Earth. Numerical simulations done by *Kipp and Melosh* [1986] examine the resulting interaction between two colliding planets. Both planets are assumed to be gravitationally differentiated to contain iron cores with radii equal to one half of the planets' radii. The simulation is run from the moment of impact to 12.5 minutes afterwards and shows a large portion of the proto-Earth's mantle being ejected while the iron cores of each respective body remain relatively untouched (Fig. 1.2). The numerical model was concerned primarily with the collision between two proto-planets and did not provide much insight to the accretion post-collision.
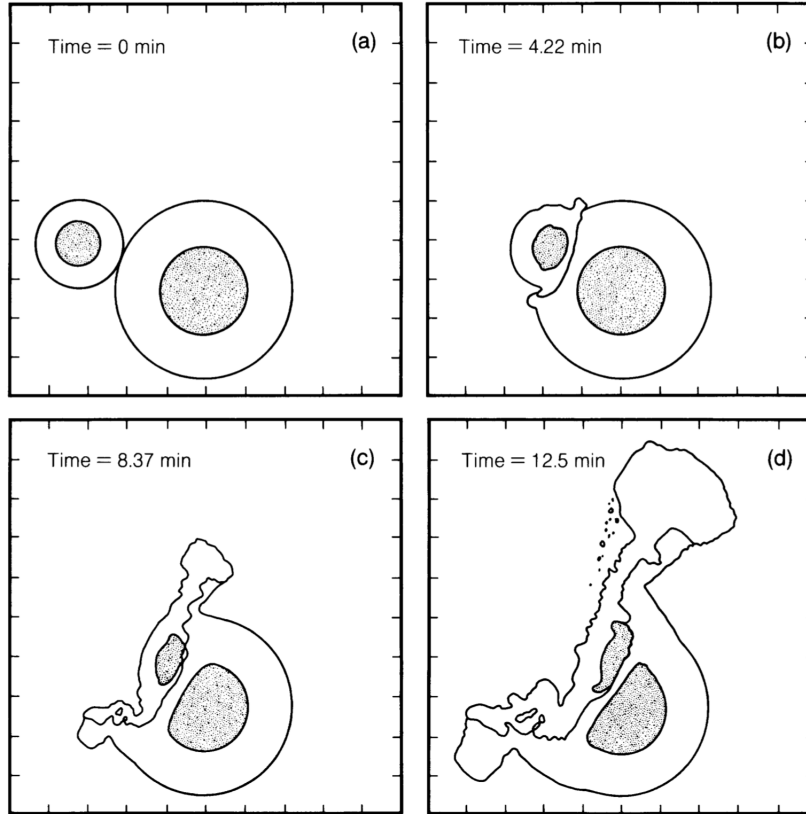
Figure 1.2: A simulation of colliding planets with small iron cores from moment of impact to 12.5 minutes post impact. From *Kipp and Melosh* [1986]

Further studies of the collision hypothesis were done by *Canup and Asphaug* [2001] using Smooth Particle Hydrodynamics (SPH) simulations to examine the interactions of colliding planets (Fig. 1.3). The focus of this study was the effect of relatively small impactors with values $\gamma < 0.115$ where $\gamma = \frac{M_{imp}}{M_t}$, M_t being the total mass of the system, and M_{imp} being the mass of the impactor. Both the proto Earth and impactor were assumed to have small iron cores. The main constraint was matching the iron abundance in the debris disk to be approximately equal to the mass fraction of the Lunar core ($\frac{M_{Fe}}{M_D} = 0.03$) where M_D is the total mass in the debris disk and M_{Fe} is the total mass of iron in the disk. In addition, the resulting debris disk and post impact planet must have had a similar mass to that of the present-day Moon. It was found that large impactors ($\gamma > 0.115$) could produce large debris disks, but resulted in a system with too much angular momentum to satisfy the present-day Earth Moon system. Conversely, in order for a small impactor ($0.08 < \gamma < 0.09$) to produce enough ejecta to match the Lunar

mass, a glancing impact would need to occur, resulting in too much iron in the debris disk. The most successful impacts were those of an impactor to total mass ratios of $0.1 > \gamma > 0.11$, about the mass of Mars. Despite the angular momentum problem of high mass impactors, in a followup study, *Canup* [2012] showed that large impactors ($\gamma > 0.4$) were also a viable theory, given that the angular momentum of the Earth-Moon system was decreased by a factor of 2-2.5 through resonant evection with the sun, which was shown to be a possibility through the work of *Cuk and Stewart* [2012].
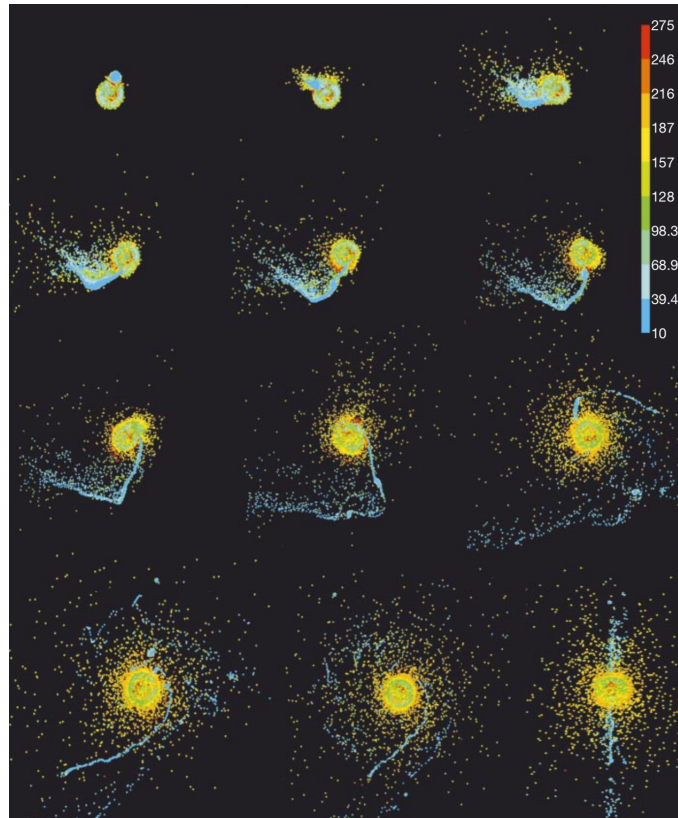
Figure 1.3: Simulation between two colliding proto-planets from moment of impact to 23 hours post collision. The color represents internal energy in units of 6.67×10^8 erg g^{-1}. From *Canup and Asphaug* [2001].

This modern collision hypothesis explains the Moon's similar composition to that of the Earth's without imposing contrived scenarios of capture or formation. Whether a collision between two planetary bodies of this size in the early solar system was plausible depends on the abundance of such planetary bodies at the time of solar system formation. A study by *Hartmann and Davis* [1975] explores the evolution of planetary bodies in the

early solar system and possible sizes of neighbouring planets. It was found that secondary planetesimals in the vicinity of the primary planet were quite common and could have been quite sizeable even relative to the primary planet. These large bodies could have struck the Earth within 10^7 - 10^8 years of formation, ejecting the iron-deficient mantle of the proto-Earth into orbit (and beyond as well). The ejected material would have quickly settled in the equatorial plane where a satellite could have formed [*Canup and Asphaug*, 2001].

Despite the controversy surrounding the origin of the Moon, one conclusion can be drawn: much more data is needed in order to confidently surmise the origin of the Moon. The Apollo missions were thought to have brought this answer to the surface but instead revealed that the Moon is a more complex body than we previously thought.

1.3   Lunar Laser Ranging

The orbital motion and orientation of the Moon have been extensively studied, especially in the decades following the Apollo missions where retroreflectors arrays placed on the surface allowed for centimetre measurement accuracy of the motions of the surface through a method called Lunar Laser Ranging (LLR). The first observatory to acquire LLR data was the McDonald observatory near Fort Davis, Texas and the Lick observatory in California. The premise of LLR itself is technologically challenging [*Dickey et al.*, 1994]. The outgoing laser is collimated to 3-4 arcseconds which translates to an area with a diameter of about 7 km on the surface of the Moon. The retroreflectors reflect the photons back along the paths of incidence (deviating by up to 10 arcseconds due to diffraction), however intercept only 10^{-9} of the incident ray, meaning that the overall signal loss is on the order of 10^{-21}. At the time, 3 Watts (10^{19} photons/s) was the maximum available power of such lasers, so receiving such an attenuated signal was no easy feat and required single photon detection. Nevertheless, abundant amounts of data has been accumulated over the duration of this project, with four stations still actively acquiring LLR data: Apache Point observatory, New Mexico, US, McDonald Laser Ranging Station, Texas, US, Observatoire de la Côte d'Azur, France and Matera, Italy [*Munhemezulu et al.*, 2016].

The orbital and rotational dynamics of the Moon are highly sensitive to its many parameters, meaning LLR can provide insight into many Lunar properties [*Williams et al.*, 2014]. For example, LLR provides a measure of moment of inertia differences

through measurements of physical librations:

$$\beta = \frac{C - A}{B} \ , \tag{1.1a}$$

$$\gamma = \frac{B - A}{C} \ , \tag{1.1b}$$

where A and B are the equatorial moments of inertia, and C is the polar moment of inertia. The second degree gravity coefficients J_2 and C_{22} can be related to the moment differences through:

$$J_2 + 2C_{22} = \frac{C - A}{MR^2} \ , \tag{1.2a}$$

$$J_2 - 2C_{22} = \frac{C - B}{MR^2} \ , \tag{1.2b}$$

$$4C_{22} = \frac{B - A}{MR^2} \ , \tag{1.2c}$$

where M is the Lunar mass and R is the mean radius. The total moment of inertia of the Moon was found to be 1.6 % less than that of a homogenous sphere [*Williams et al.*, 2014] meaning any denser core would be relatively small. At the end of the 1970's, LLR detected dissipation on the Moon, which was found through a slight misalignment in the orientation of the precessing mantle's figure axis. The dissipation has since been attributed to solid body tides, as well as power dissipation at the core-mantle boundary. Tidal deformation has also been detected through the Love numbers h_2 (vertical tides) and l_2 (horizontal tides) which can be determined through the displacement of the retroreflector arrays.

While LLR has been paramount in the study of the Moon, it does not detect the rotational dynamics of internal structures, at least not above the accuracies we have today. The interior dynamics have therefore been left to mathematical modelling.

1.4 Lunar interior

Love numbers and moments of inertia found through LLR support the existence of a liquid core with a radius of 250 - 430 kilometers [*Wieczorek et al.*, 2006]. In addition to LLR, Lunar seismology has also aided in constraining Lunar interior structures however little is certain about the deep Lunar interior to this day. The four seismometers depend entirely on passive seismic events. While global seismology on Earth yields abundant information about its interior structure, the same cannot be said for the Moon. Most seismic events occur deep within the Moon (700-1200 km in depth), up to 4 in magnitude, but are often far less energetic [*Heiken et al.*, 1991]. What can be surmised however

is that there is a region of high attenuation in the lowermost mantle consistent with partial melt and a fluid core with a radius ranging between 310-350 km [*Weber et al.*, 2011]. Another strong reflection is seen at 240±10 km in radius, and the lack of SH signal suggests the presence of a solid inner core, although its existence is still equivocal [*Garcia et al.*, 2011] as gathering seismic data from the Moon's deep interior has proved to be a challenge and has resulted in noisy data. A possible interior structure of the Moon is shown in Fig. 1.4, though it needs to be emphasized that the thickness of each region remains poorly constrained. Additional seismic and gravitational data is needed in order to further constrain the structures of the Lunar interior.
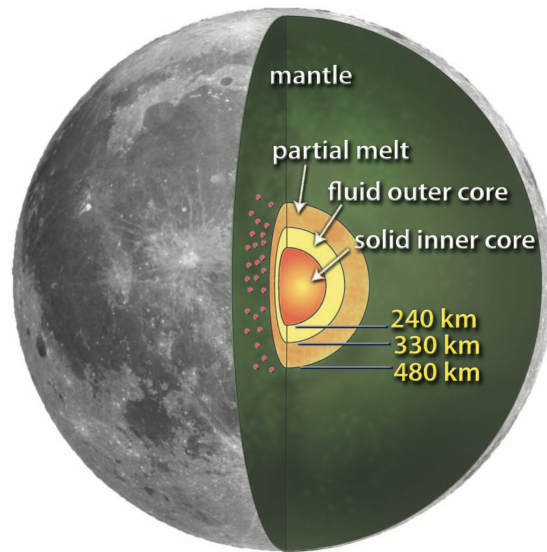
Figure 1.4: Subsurface Lunar profile from seismic array-processing methods including a solid inner core. From *Weber et al.* [2011]

For the purpose of this study, we assume the existence of a solid inner core, with radii varying between 10-250 kilometers, as well as a fluid outer core with sizes ranging from 300 to 420 kilometers in radius, both of which are in agreement with the seismic data.

1.5 Lunar rotational and orbital dynamics

The Moon orbits around the Earth once every 27.3 days, and rotates around itself with the same period. This results in a tidally locked orbit, meaning the same face of the Moon is always pointing towards the Earth throughout its orbital motion. Its orbital plane is inclined by 5.145° with respect to the ecliptic plane and is slightly eccentric (e=0.0549),

Interaction Type	Amplitudes
Ellipticity	20905 km
Solar perturbations	3699 & 2956 km
Jupiter perturbations	1.06 km
Venus perturbations	0.73, 0.68 & 0.6 km
Earth J_2	0.46 and 0.45 km
Moon J_2 & C_{22}	0.2 m
Earth C_{22}	0.5 mm
Lorentz contraction	0.95 m
Solar potential	6 cm
Time transformation	5 cm
Other relativity	5 cm
Solar radiation pressure	4 mm

Table 1.1: Sources of radial variation in the Lunar orbit

perturbed strongly by the solar gravitational field, Jupiter to a lesser extent and by numerous other negligible sources (table 1.1)[*Williams and Dickey*, 2002; *Chapront-Touzé and Chapront*, 1983].

The symmetry axis of the Moon is tilted by 1.543° with respect to the ecliptic plane (Fig. 1.5). The Moon is in a Cassini state which is described by the last of Cassini's three laws as a stable configuration of its spin-symmetry and orbital axes, both of which are coplanar with the ecliptic normal [*Peale*, 1969]. Due to the longevity of the LLR project, the precessional motion of the Moon has also been well constrained. Both the spin-symmetry axis and orbital plane normal precess in a retrograde motion with a period of 18.6 years, meaning that the Cassini state is preserved throughout the precessional motion. The precession of the Moon is most strongly influenced by the solar gravitational field, and weakly by Earth's ellipticity coefficient (J_2) along with other less significant sources listed in table 1.2 [*Williams and Dickey*, 2002].

In truth the Moon isn't in a perfect Cassini state, it's spin-symmetry axis is ahead by 0.26 arc seconds, a lead most likely caused by a dissipation mechanism at the core-mantle boundary or solid body tidal friction, or a combination of the two [*Yoder*, 1981]. However it is such a minute amount that, at least for this study, we will assume that this offset is negligible. As successful as the LLR project is, the technique is only sensitive to the

Interaction Type	dω/dt "/yr	dΩ/dt "/yr
Solar perturbations	146 425.38	-69 671.67
Earth J_2	6.33	-5.93
Planetary perturbations	2.47	-1.44
Moon J_2 & C_{22}	-0.0176	-0.1705
Relativity	0.0180	0.0190

Table 1.2: Sources of precession of the Earth-Moon system, described in arcseconds per year.

surface motions of the Moon, meaning the rotational dynamics of the interior are not constrained directly.

Whether the fluid outer core follows the precessional motions of the overlying mantle depends on its free precession mode, or the free core nutation (FCN). The FCN is the free precessional motion of the fluid outer core when it is misaligned from the mantle's figure axis. If the frequency of the FCN is faster than the precession frequency of the mantle, the fluid outer core is locked to the movement of the mantle. Conversely, if the FCN frequency is slower than the precession frequency, the fluid outer core is not efficiently entrained by the mantle's precessional motion and instead remains aligned with the ecliptic normal. Unfortunately the period of the FCN for the Moon cannot be measured directly, but it depends on the interior density structure of the Moon and is estimated to be likely longer than 150 years [*Petrova et al.*, 2008]. The FCN period is much greater than the 18.6 year precessional period of the mantle suggesting that the fluid outer core is largely decoupled with from mantle's movement and hence it should be nearly aligned with the ecliptic normal [*Meyer and Wisdom*, 2011].

An analogous mode exists for the inner core, with its own free precession, a free mode referred to as the free inner core nutation (FICN). As with the FCN, its period cannot be observed directly, but based on plausible models of the Moon's interior, its period is estimated to be anywhere between a few years to a few decades [*Dumberry and Wieczorek*, 2016], comparable to the precessional period of mantle. We therefore expect, through resonant amplification, that the tilt angle of the inner solid core could be quite large (upwards of 10°).

A model to compute the Cassini state of a Moon that comprises a fluid core and solid
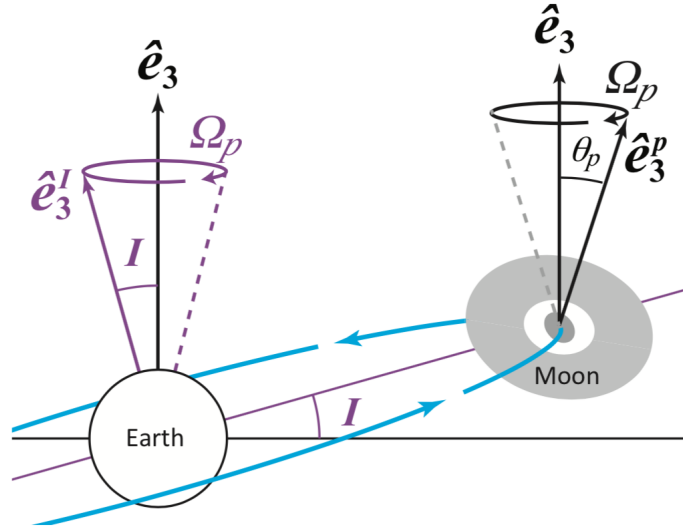
Figure 1.5: The Earth-Moon orbital dynamics. The plane of the Moon's 27.322 day orbit around the Earth (light blue) is inclined by an angle $I = 5.145°$ with respect to the ecliptic normal (pointing in the direction $\hat{e}_3$). The orientation of the orbital plane (normal vector pointing in the direction $\hat{e}_3^I$) precesses in a retrograde direction at a frequency of $\Omega_p = 2\pi/18.6 \text{ yr}^{-1}$ about $\hat{e}_3$. The symmetry axis of the Moon's mantle (pointing in the direction $\hat{e}_3^p$) is inclined by $\theta_p = 1.543°$ with respect to the ecliptic normal, in the same plane as I but in the opposite direction, and is also precessing at the frequency Ω_p.

inner core was presented in *Dumberry and Wieczorek* [2016]. The model was developed under the assumption of small angles of precession. Although this is suitable for the present-day mantle tilt of 1.543°, it is not valid in the past when the Moon was closer to the Earth and the mantle tilt might have been as high as 49° [*Ward*, 1975]. Furthermore, because of the proximity of the forcing frequency to being in resonance with the FICN, the inner core could have a relatively large angle of misalignment with the mantle. One of the objectives of this study is to develop a model of the internal Cassini states of the Moon that is more general than the one developed in *Dumberry and Wieczorek* [2016], one which remains valid for large angles of misalignment. Besides the general aim of furthering our understanding of the precession dynamics of planetary bodies, constraining the rotational dynamics of the Moon may provide insight into the mechanisms of ancient dynamo action. More specifically, the tilt angles of the fluid outer core and solid inner core are connected to the ancient Lunar dynamo, as detailed in the following section.

1.6   Ancient Lunar magnetism

Measurements of the Lunar magnetic field taken by the Apollo 15 sub-sattelites concluded that the only source of magnetism at present is from crustal magnetization causing an extremely weak field [*Runcorn*, 1975]. Paleomagnetic analyses of Lunar crustal rocks have suggested the existence of an ancient dynamo generated magnetic field up to 4.5 Gyr ago, declining by an order of magnitude by 3.3 Gyr ago (see Fig. 1.6) [*Weiss and Tikoo*, 2014]. The strength of the ancient field at its highest was up to 120 μT, at the surface of the Moon, implying a highly energetic dynamo source. Observations have also deduced that a long period of low intensity magnetism ($\sim 5 \mu$T) was present well past 2 Gyr. Given the thickness of the Lunar mantle, heat flux from the core was likely insufficient to sustain a purely thermo-chemical convective dynamo for an extended period of time [*Konrad and Spohn*, 1997; *Stegman et al.*, 2003]. For an anhydrous Lunar mantle, a purely thermal convective dynamo can sustain such a magnetic field up until at most 4.1 Gyr ago, however the introduction of water at 40 ppm can lengthen this period to 3.4 Gyr. Furthermore, based on dynamo scaling laws, the upper bound for the field intensity of a convective dynamo is an order of magnitude smaller than the paleointensities inferred from Lunar rock samples. This has raised suspicion that convection may not be the only source of the ancient Lunar magnetic field (Fig. 1.6) [*Weiss and Tikoo*, 2014].

An alternative dynamo mechanism proposed by *Williams et al.* [2001] is based on a precessing mantle driving mechanical stirring of the underlying fluid outer core. A recent study by *Dwyer et al.* [2011] has shown that mantle precession can produce enough power dissipation at the core mantle boundary (CMB) potentially explaining the intensity and longevity of the ancient magnetic field (Fig. 1.7). The power available to generate a dynamo can be assessed by the viscous dissipation associated with differential rotation at the CMB. The latter depends on the angle of offset between the rotation of the mantle and the fluid outer core:

$$P \propto \Omega_0^3 \sin^3 \theta_f \ , \tag{1.3}$$

where θ_f is the angle of misalignment between the mantle and the fluid outer core, and while the mantle and fluid core are in close rotation at present, the misalignment could have been much larger in the past [*Ward*, 1975]. Ω_0, the rotation rate of the mantle, would also have been faster in the past, therefore increasing the power dissipation. The non-spherical shape of the CMB may further amplify this stirring effect.

However mechanical stirring at the CMB still falls slightly short of explaining the largest paleointensities, as seen in Fig. 1.7. In addition to this, the dynamo from differential rotation at the CMB is expected to shut off at around 2.7 billion years ago
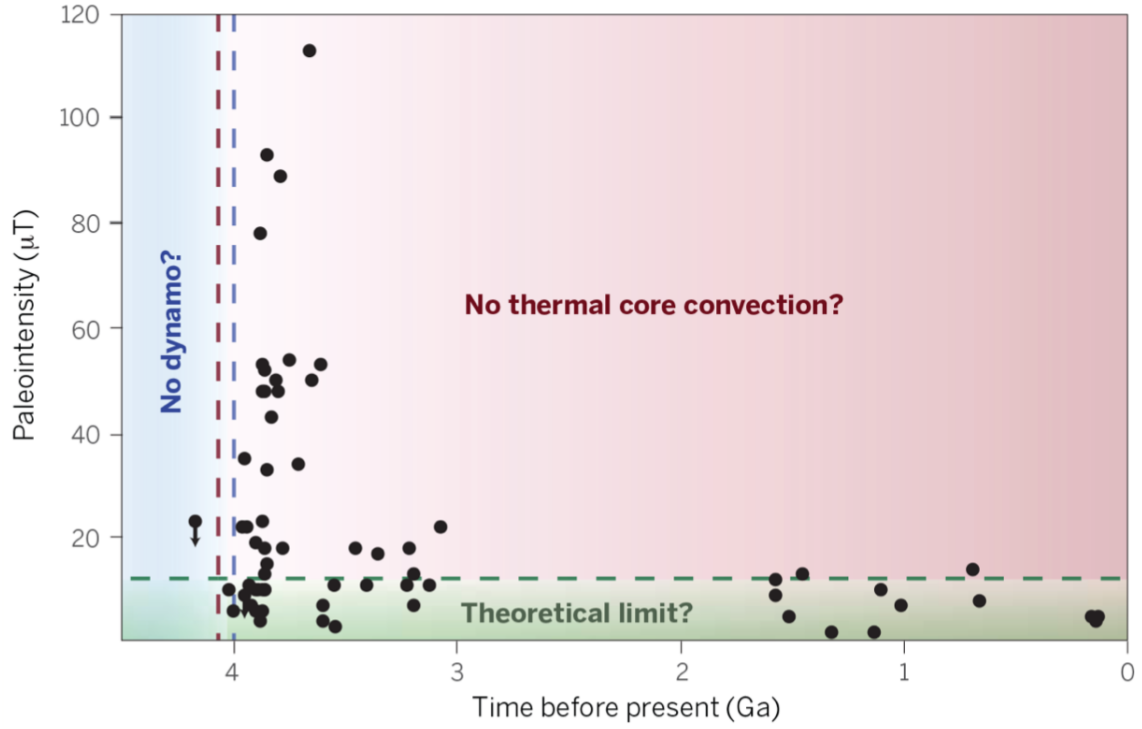
Figure 1.6: Paleointensity of the dynamo generated Lunar magnetic field as a function of time before present. These estimates are based on remnant magnetization recorded in Lunar rock samples. The green dashed line shows the estimated intensity limit of a purely thermochemical convective dynamo. From *Weiss and Tikoo* [2014]

[*Dwyer et al.*, 2011], leaving the most recent paleomagnetic measurements unexplained.

One objective of this thesis is to investigate whether differential rotation at the inner core boundary (ICB) may be a possible explanation for the ancient Lunar dynamo. As mentioned in the previous section, the 18.6 year precession period of the mantle lies within the FICN resonance band, so relatively large angles of offset between the fluid outer core and solid inner core rotation vectors $(\theta_f - \theta_s)$ are expected. Given that the dissipation depends on $\sin^3 (\theta_f - \theta_s)$, the stirring effect at the ICB could potentially be quite large.

The derivation of magnetic field intensity from power dissipation used in *Dwyer et al.* [2011] is based on a scaling law derived from convection dynamos. Heat dissipated at the CMB cannot drive convection, hence raising the question as to whether the magnetic field amplitudes predicted are valid. However, heat dissipated at the ICB can subsequently
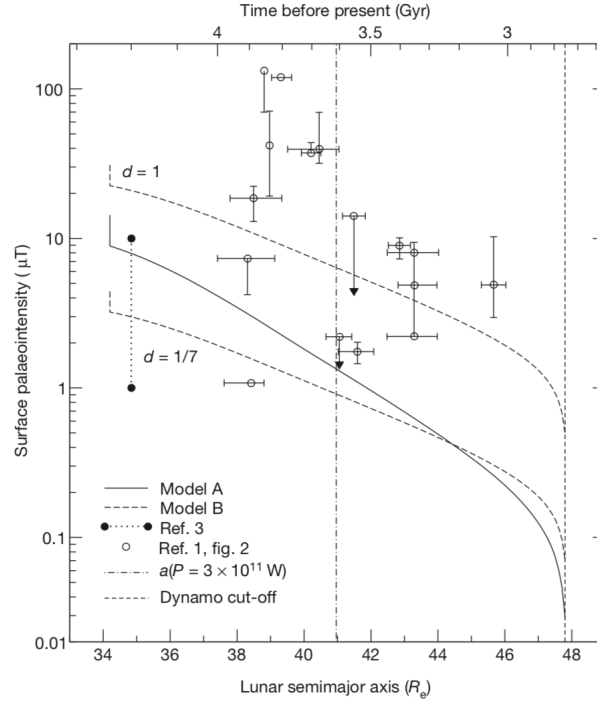
Figure 1.7: Magnetic field intensity as a function of Lunar semi-major axis predicted on the basis of dynamo generated by the precession of the Lunar mantle. The two dashed curves are close variants of one model, whereas the solid curve is a different model all together. Data points with error bars both in intensity and age are from Lunar rocks collected during the Apollo missions. From *Dwyer et al.* [2011]

lead to convection rendering these dynamo scaling laws at least more appropriate for our stirring model.

Explaining the longevity of the low intensity field has been an area of contention as well, considering that thermal convection has been shown to be largely inadequate over long periods of time. Mechanical stirring at the ICB could potentially explain this phenomenon as well. Since the FICN of the solid inner core was estimated to range between a few years to a few decades, the forcing frequency of the Lunar system would have been in this range throughout most of its history. Consequently, resonant amplification could have been a long lasting phenomenon on the solid inner core, resulting in large angles of offset for a long period of time, possibly explaining this extended period of low intensity magnetism (Fig. 1.6).

1.7   Main objectives of this thesis

The primary objective of this thesis is to develop a model of the Cassini state of a Moon comprised of a mantle, fluid outer core and solid inner core. That is, a model which allows us to predict the angle of tilt of both the fluid core and inner core in their 18.6 year precession. We developed our model so that the tilt angles can be predicted for a given interior density structure of the Moon.

By varying the orbital parameters of the Earth-Moon system, our Cassini state model can be extended to earlier periods in Lunar history. A natural extension of our model allows us to investigate how viscous dissipation at both the CMB and ICB may have changed as a function of time (or Earth-Moon distance). Based on this, the second objective of this thesis is to build estimates of the strength of the magnetic field that may have been generated by mechanical stirring at the CMB and ICB.

The second chapter of this thesis is focused on the development of the model of the Cassini state of the Moon. We investigate the effects that the various Lunar parameters have on the internal rotational dynamics and on the tilt angles of the fluid core and inner core.

In chapter three we will discuss the process of extending our Cassini state model in the Lunar past and the resulting dissipation and paleomagnetic intensities as they vary over Earth-Moon distance. We will also investigate how the resulting magnetic field changes as a function of Lunar model at various times in Lunar history.

Chapter 4 will conclude this thesis and discuss discuss the potential outlook of this project.

Chapter 2

The Cassini states of the Lunar inner core[1]

2.1 Theory: Orbital dynamics

The rotational model of the Moon that we develop below is based on the model presented in *Dumberry and Wieczorek* [2016], hereinafter referred to as DW16, which is itself an adaptation of a model developed to study Earth's nutations. The original nutation model is presented in detail in *Mathews et al.* [1991].

The procedure that we follow is, first, to define a reference interior model of the Moon (section 2.1.1). This interior model is constructed under the assumption that no external torque acts on the Moon. We then place this reference model in orbit about Earth, subject to its gravitational field, and consider how the alignment of the symmetry axes and rotation vectors of each region is altered in the Cassini state. To do so, we must properly define each of these vectors in the reference frame attached to the rotating mantle, the frame in which the nutation model is developed. This is done in section 2.1.2. The rotational model is then developed in section 2.1.3.

2.1.1 The interior density model of the Moon

We assume a simple model of the Moon of mass M with an external radius R, a solid inner core of radius r_s, a fluid outer core of radius r_f, a crust of thickness h_c, and a mantle with an outer radius of $r_m = R - h_c$. The densities of the solid inner core (ρ_s), fluid core (ρ_f), mantle (ρ_m) and crust (ρ_c) are assumed uniform. Adopting uniform

---

[1]This chapter has been published: Stys, C. & Dumberry, M. (2018). The Cassini state of the Moon's inner core. *Journal of Geophysical Research: Planets*, 123.

density layers amounts to neglecting compressibility effects from increasing pressure with depth. Given the small pressures in the Moon's interior (less than about 5 GPa), this is a good first order description.

The precession model that we develop below involves the principal moments of inertia of each region. The latter are related to the spherical harmonic degree two coefficients of the gravity field of the Moon. For convenience, we assume a reference model in which the principal moments of inertia of each region are aligned. Although in reality this is unlikely to be the case because the surface topography of degree two is not aligned with the degree two gravity field [*Araki et al.*, 2009; *Smith et al.*, 2010], this assumption greatly simplifies our reference model. Since we assume uniform density layers, all contributions to the non-spherical gravity field (i.e. all mass anomalies) are caused by topography at region boundaries. The principal moments of inertia of each region are then connected to the degree two topography at region boundaries, more specifically to the polar and equatorial flattening. We define the polar flattening as the difference between the equatorial and polar radius, divided by the mean spherical radius. Likewise, we define the equatorial flattening as the difference between the maximum and minimum equatorial radius, divided by the mean spherical radius. We denote the polar flattening at the inner core boundary (ICB), core-mantle boundary (CMB), crust-mantle boundary and surface by ϵ_s, ϵ_f, ϵ_m, and ϵ_r, respectively. The difference between the equatorial and polar radius at each of these interfaces is then $r_s\epsilon_s$, $r_f\epsilon_f$, $r_m\epsilon_m$, and $R\epsilon_r$, respectively. The equatorial flattening at the same boundaries are denoted by ξ_s, ξ_f, ξ_m and ξ_r, respectively. The difference between the maximum and minimum equatorial radius at each of these interfaces is then $r_s\xi_s$, $r_f\xi_f$, $r_m\xi_m$, and $R\xi_r$, respectively.

The polar and equatorial flattenings of each region are connected to the principal moments of inertia of the whole Moon ($C > B > A$), fluid core ($C_f > B_f > A_f$) and solid inner core ($C_s > B_s > A_s$). In particular, they are connected to the degree two coefficients of the gravity potential J_2 and C_{22} by

$$J_2 = \frac{C - \bar{A}}{MR^2} = \frac{8\pi}{15}\frac{1}{MR^2}\left[(\rho_s - \rho_f)r_s^5\epsilon_s + (\rho_f - \rho_m)r_f^5\epsilon_f + (\rho_m - \rho_c)r_m^5\epsilon_m + \rho_c R^5\epsilon_r\right],$$
(2.1a)

$$C_{22} = \frac{B - A}{4MR^2} = \frac{8\pi}{15}\frac{1}{4MR^2}\left[(\rho_s - \rho_f)r_s^5\xi_s + (\rho_f - \rho_m)r_f^5\xi_f + (\rho_m - \rho_c)r_m^5\xi_m + \rho_c R^5\xi_r\right].$$
(2.1b)

where $\bar{A}$ is the mean equatorial moment of inertia of the whole Moon. The latter, and the mean equatorial moments of the fluid core ($\bar{A}_f$) and inner core ($\bar{A}_s$) are defined as

$$\bar{A} = \frac{1}{2}(A + B), \quad \bar{A}_f = \frac{1}{2}(A_f + B_f), \quad \bar{A}_s = \frac{1}{2}(A_s + B_s). \tag{2.2}$$

From these, we define the dynamical ellipticities of the whole Moon (e), fluid core (e_f) and solid inner core (e_s),

$$e = \frac{C - \bar{A}}{\bar{A}} \quad e_f = \frac{C_f - \bar{A}_f}{\bar{A}_f} \quad e_s = \frac{C_s - \bar{A}_s}{\bar{A}_s}. \tag{2.3}$$

These dynamical ellipticities are important parameters of our model and the way in which they are calculated is explained in more detail in section 2.2.

Although the density discontinuity at the crust-mantle boundary is taken into account in the interior mass distribution, the solid outer shell region that comprises both the crust and mantle constitute a single body in terms of the rotational dynamics. For short, in the development of the rotational model below, we will refer to this outer region as the mantle. If we define the direction of the figure axis of this "mantle" by $\hat{e}_3^p$, then the ellipsoidal figures of each region of our reference model are aligned, and are in uniform rotation at the sidereal frequency $2\pi/27.322$ day^{-1} about $\hat{e}_3^p$.

2.1.2 Definition of the reference frames, symmetry axes and rotation vectors

The focus of our study is to describe the equilibrium Cassini state of the Moon. As such, we focus on the long timescale dynamics, and only consider the response of the Moon to the gravitational torque by Earth averaged over one orbit. In other words, we neglect the modulation of the torque over one orbit and the small latitudinal and longitudinal librations of the Moon that result from it. This assumption is implicit in the presentation of our model and in the discussion of all our results.

To describe the Cassini state of the Moon, we must first define the possible reference frames in which to view the orbital and rotational dynamics. We use three different reference frames in our study. The first is the inertial reference frame, defined by unit vectors $(\hat{e}_1, \hat{e}_2, \hat{e}_3)$, with $\hat{e}_3$ aligned with the ecliptic normal. The second is a reference frame attached to the rotating mantle, defined by unit vectors $(\hat{e}_1^p, \hat{e}_2^p, \hat{e}_3^p)$. We have already defined $\hat{e}_3^p$ to be aligned with the maximum (polar) moment of inertia of the mantle. $\hat{e}_1^p$ and $\hat{e}_2^p$ are aligned, respectively, with the minimum and intermediate moments of inertia (both in equatorial directions). This is the frame in which we develop our dynamical model. As mentioned in the introduction, the Cassini state is characterized by a tilt of $\hat{e}_3^p$ from $\hat{e}_3$, though both remain co-planar with the orbit normal $(\hat{e}_3^I)$. It is convenient to refer to the plane which contains all three as the "Cassini plane". Viewed

in the inertial frame, the Cassini plane is rotating in the retrograde direction at frequency Ω_p about an axis aligned with the ecliptic normal ($\hat{e}_3$). A third reference frame in which to view the rotational dynamics is then one attached to this Cassini plane. We refer to this reference frame as the Cassini frame, defined by unit vectors ($\hat{e}_1^c$, $\hat{e}_2^c$, $\hat{e}_3^c$). Direction $\hat{e}_3^c$ is aligned with the ecliptic normal, and the Cassini plane coincides with the surface defined by $\hat{e}_1^c$ and $\hat{e}_3^c$. Direction $\hat{e}_2^c$ is perpendicular to the Cassini plane and is aligned with the line of the descending node of the Lunar orbit on the ecliptic plane.

When viewed in the Cassini frame, the orientation of the orbit normal ($\hat{e}_3^I$) and mantle figure axis ($\hat{e}_3^p$) remain at fixed orientations with respect to the ecliptic normal ($\hat{e}_3^c = \hat{e}_3$) (Fig. 2.1a). As defined earlier, the angle of tilt between $\hat{e}_3^p$ and $\hat{e}_3^c$ is denoted by θ_p and LLR observations suggest that it is equal to $\theta_p = 1.543°$. This tilt is caused by the gravitational torque that the Earth exerts on the ellipsoidal shape of the mantle and, secondarily, by internal torques from the inner core and the fluid core. It is the tilt angle that allows to balance the total torque acting on the mantle with a change in its angular momentum at the same rate as the precession of the orbit, and therefore to maintain a stationary configuration in the Cassini frame.

Likewise, the ellipsoidal inner core is also subject to a gravitational torque from Earth and to internal torques from the mantle and fluid core. For the inner core, the internal torque – especially the gravitational torque from the fluid core and mantle – is much more important than the torque from Earth (DW16). As is the case for the mantle, the orientation of the figure axis of the inner core (denoted by $\hat{e}_3^s$) should evolve to that which allows to balance the torque acting on it with a change in its angular momentum at the same rate as the orbit precession. In other words, the inner core is also in a Cassini state and, viewed in the Cassini frame, the orientation of $\hat{e}_3^s$ remains fixed. We expect $\hat{e}_3^s$ to differ from $\hat{e}_3^p$ because the inner core is subject to a different torque balance than the mantle. We define the angle of inner core tilt θ_n as the angle of misalignment of $\hat{e}_3^s$ with respect to the mantle figure axis $\hat{e}_3^p$.

The rotation and symmetry axes of the mantle – and similarly those of the inner core – are expected to remain in close alignment, but they do not coincide exactly. The rotation vector of the fluid core is expected to be misaligned from that of the mantle, remaining instead in a close alignment with the ecliptic normal. Each of these rotation vectors lie on the Cassini plane and their orientations remain fixed when viewed in the Cassini frame (Fig. 2.1b). We define the rotation vector of the mantle as $\boldsymbol{\Omega}$, misaligned by an angle θ_m with respect to the mantle figure axis. The rotation vectors of the fluid core and inner core are defined as $\boldsymbol{\Omega_f}$ and $\boldsymbol{\Omega_s}$. Their misalignment angles, respectively θ_f and θ_s, are defined with respect to the mantle rotation vector $\boldsymbol{\Omega}$ (Fig. 2.1b).

To be formal in our definition of the different angles of misalignment, I is defined positive pointing from $\hat{e}_3^c$ to $\hat{e}_3^I$. Angles θ_p, θ_n, θ_m, θ_f and θ_s are defined positive in the clockwise direction when viewed in the Cassini frame. According to this convention, θ_f as depicted in Fig. 2.1 is negative, and we expect this to be the case since $\boldsymbol{\Omega}_f$ should be closely aligned with the ecliptic normal ($\hat{e}_3^c = \hat{e}_3$).

The mean gravitational torque that Earth exerts on the mantle, averaged over one orbit, can be replaced by that produced by a ring of mass equivalent to that of Earth encircling the Moon on a plane with normal vector $\hat{e}_3^I$. Viewed in the Cassini frame, the amplitude of this mean torque remains constant and in direction $-\hat{e}_2^c$ (the direction of the line of the ascending node), perpendicular to the Cassini plane. Likewise, the gravitational torque that Earth exerts on the inner core is also perpendicular to the Cassini plane. The direction of the torque depends on the sign of the sum of $(I + \theta_p + \theta_n)$: if it is positive, the torque is in direction $-\hat{e}_2^c$; if it is negative, the torque is instead in direction $\hat{e}_2^c$.

Although the mantle figure axis $\hat{e}_3^p$ remains at a fixed orientation in the Cassini frame, the two equatorial directions $\hat{e}_1^p$ and $\hat{e}_2^p$ do not since the mantle is rotating about $\hat{e}_3^p$. Viewed in the Cassini frame, the period of rotation of $\hat{e}_1^p$ and $\hat{e}_2^p$ around $\hat{e}_3^p$, must be equal to the time it takes for the Moon to return to the ascending node of its orbit. The frequency of this rotation, which we denote Ω_c, is equal to $2\pi/27.212$ day^{-1}.

We develop our rotational model in a frame attached to the rotating mantle. As seen by an observer on the mantle, the longitudinal orientation of the Cassini plane is rotating in the retrograde direction about $\hat{e}_3^p$ at frequency Ω_c (Fig. 2.1c,d). The unit vectors $\hat{e}_3^I$, $\hat{e}_3^c$ and $\hat{e}_3^s$ and the rotation vectors $\boldsymbol{\Omega}$, $\boldsymbol{\Omega}_f$ and $\boldsymbol{\Omega}_s$ remain at fixed orientations, but are precessing about $\hat{e}_3^p$ in the retrograde direction at frequency Ω_c. Since the gravitational torque by Earth remains perpendicular to the Cassini plane, as seen by an observer on the mantle, this torque is periodic, with a retrograde frequency equal to Ω_c. Following the nutation model of , it is convenient to introduce a frequency factor ω, connected to Ω_c by $\Omega_c = -\omega\Omega_o$, where $\Omega_o = 2\pi/27.322$ day^{-1} is the amplitude of the rotation vector of the mantle. To a good approximation, Ω_o is related to Ω_c and Ω_p by

$$\Omega_o = \Omega_c - \Omega_p \cos(\theta_p)\,. \tag{2.4}$$

The frequency factor ω is then equal to

$$\omega = -\frac{\Omega_c}{\Omega_o} = -1 - \cos(\theta_p)\,\delta\omega\,, \tag{2.5}$$

where $\delta\omega = \Omega_p/\Omega_o$ = 27.322 days / 18.6 yr = 4.022×10^{-3} is the Poincaré number,

expressing the ratio of precession to rotation frequency. ω represents then the frequency of the periodic gravitational forcing that Earth applies on the Moon, expressed in units of cycles per Lunar day, as seen by an observer on the mantle.

The time-dependent longitudinal orientation of the Cassini plane, as seen by an observer on the mantle, and expressed in terms of ω, can be written as

$$\hat{e}^p_\perp(t) = \cos(\omega\Omega_o t)\hat{e}^p_1 + \sin(\omega\Omega_o t)\hat{e}^p_2 \,, \tag{2.6}$$

where t is time and direction $\hat{e}^p_1$ has been chosen to be aligned with the projection of $\hat{e}^c_1$ onto the equator of the mantle at $t = 0$ (Fig. 2.1c,d). It can be shown that

$$\frac{d}{dt}\hat{e}^p_\perp(t) = \omega\Omega_o\Big(\hat{e}^p_3 \times \hat{e}^p_\perp(t)\Big) \,, \tag{2.7}$$

where the time derivative is taken in the mantle frame. Note that the direction of $\hat{e}^p_3 \times \hat{e}^p_\perp(t) = \hat{e}^c_2$ (see Fig. 2.1c,d). Since ω is negative, the time derivative of $\hat{e}^p_\perp(t)$ points in direction $-\hat{e}^c_2$, the same direction as the gravitational torque from Earth on the mantle.

Using the definition of $\hat{e}^p_\perp(t)$ in Eq. (2.6), we can express the direction of the normal to the ecliptic $\hat{e}_3$ and the figure axis of the inner core $\hat{e}^s_3$, as seen in the mantle frame, by

$$\hat{e}_3 = \hat{e}^c_3 = \cos\theta_p\,\hat{e}^p_3 - \sin\theta_p\,\hat{e}^p_\perp(t) \,, \tag{2.8a}$$

$$\hat{e}^s_3 = \cos\theta_n\,\hat{e}^p_3 + \sin\theta_n\,\hat{e}^p_\perp(t) \,. \tag{2.8b}$$

In appendix A, we present the definitions of the rotation vectors of the mantle, fluid core and inner core for the tidally locked spin-orbit configuration of the Moon. The amplitude of each of these rotation vectors differ from one another, although the difference between them is small (at most of the order of $\delta\omega$) and it is convenient for the development of our model to approximate all three vectors as having the amplitude Ω_o defined in Eq. (2.4). The rotation vectors of the mantle, fluid core and inner core can be written, respectively, as

$$\boldsymbol{\Omega} = \Omega_o\bigg(\cos\theta_m\,\hat{e}^p_3 + \sin\theta_m\,\hat{e}^p_\perp(t)\bigg) \,, \tag{2.9a}$$

$$\boldsymbol{\Omega_f} = \Omega_o\bigg(\cos(\theta_m + \theta_f)\hat{e}^p_3 + \sin(\theta_m + \theta_f)\hat{e}^p_\perp(t)\bigg) \,, \tag{2.9b}$$

$$\boldsymbol{\Omega_s} = \Omega_o\bigg(\cos(\theta_m + \theta_s)\hat{e}^p_3 + \sin(\theta_m + \theta_s)\hat{e}^p_\perp(t)\bigg) \,. \tag{2.9c}$$
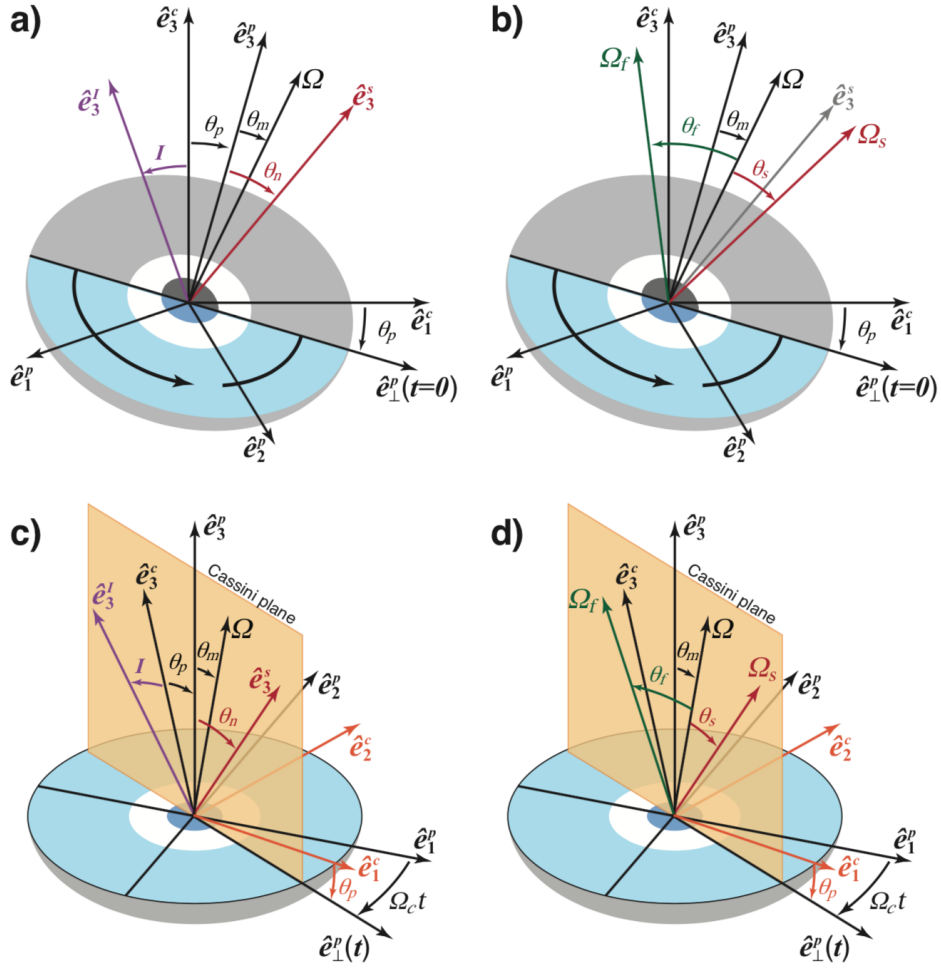
Figure 2.1: The Cassini state of the Moon viewed (a, b) in the Cassini frame and (c, d) in a frame attached to the rotating mantle. The Cassini frame is defined by unit vectors $(\hat{e}_1^c, \hat{e}_2^c, \hat{e}_3^c)$, the mantle frame by unit vectors $(\hat{e}_1^p, \hat{e}_2^p, \hat{e}_3^p)$. Viewed in the Cassini frame (a, b), the orbit normal $(\hat{e}_3^I)$, the symmetry axes of the mantle $(\hat{e}_3^p)$ and inner core $(\hat{e}_3^s)$, and the rotation vectors of the mantle $(\mathbf{\Omega})$, fluid core $(\mathbf{\Omega}_f)$ and inner core $(\mathbf{\Omega}_f)$ remain at fixed orientations. The light grey, white, and dark grey ellipsoid in panels (a) and (b) represent a polar cross-section of the mantle, fluid core and inner core, respectively. Blue shaded parts show the equatorial cross section. The black curved arrow in the equatorial plane of panels (a) and (b) indicates the direction of rotation, at frequency Ω_c, of the mantle frame axes $\hat{e}_1^p$ and $\hat{e}_2^p$ about $\hat{e}_3^p$. Viewed in the frame attached to the rotating mantle (c, d), the Cassini plane is rotating at frequency $-\Omega_c$ in the longitudinal direction. The unit vector $\hat{e}_\perp^p(t)$ captures the time-dependent longitudinal orientation of the Cassini plane as seen in the mantle frame; it points in the direction of the projection of $\hat{e}_1^c$ on the equatorial plane of the mantle.

It is further convenient to introduce $\boldsymbol{\omega}_f$ and $\boldsymbol{\omega}_s$, the perturbation in the rotation of the fluid core and inner core, respectively, with respect to that of the mantle, defined as

$$\boldsymbol{\omega}_f = \boldsymbol{\Omega}_f - \boldsymbol{\Omega}\,, \tag{2.10a}$$

$$\boldsymbol{\omega}_s = \boldsymbol{\Omega}_s - \boldsymbol{\Omega}\,. \tag{2.10b}$$

2.1.3 The rotational model

Our goal is to determine the Cassini state of the whole of the Moon. That is, to determine the precession dynamics of our reference interior model of the Moon when placed in orbit around Earth and subject to its gravitational torque. In short, our goal is to determine the five angles θ_p, θ_n, θ_m, θ_f and θ_s for a given Lunar interior density structure. These angles obey a system of five equations. The first three describe respectively the evolution of the angular momentum of the whole Moon ($\boldsymbol{H}$), the fluid outer core ($\boldsymbol{H_f}$) and solid inner core ($\boldsymbol{H_s}$) in the reference frame rotating with the mantle,

$$\frac{d}{dt}\boldsymbol{H} + \boldsymbol{\Omega} \times \boldsymbol{H} = \boldsymbol{\Gamma}\,, \tag{2.11a}$$

$$\frac{d}{dt}\boldsymbol{H_f} - \boldsymbol{\omega_f} \times \boldsymbol{H_f} = \boldsymbol{0}\,, \tag{2.11b}$$

$$\frac{d}{dt}\boldsymbol{H_s} + \boldsymbol{\Omega} \times \boldsymbol{H_s} = \boldsymbol{\Gamma_s}\,, \tag{2.11c}$$

where $\boldsymbol{\Gamma}$ is the gravitational torque from Earth acting on the whole Moon and $\boldsymbol{\Gamma_s}$ is the total gravitational and pressure torque exerted on the inner core. The final two equations of the model are kinematic relations, one to express the change in the orientation of the inner core figure resulting from its own differential rotation, and the second describing the invariance of the ecliptic normal in the inertial frame as seen in the frame attached to the mantle. They are respectively,

$$\frac{d}{dt}\hat{e}_3^s + \hat{e}_3^s \times \boldsymbol{\omega_s} = \boldsymbol{0}\,, \tag{2.12a}$$

$$\frac{d}{dt}\hat{e}_3 + \boldsymbol{\Omega} \times \hat{e}_3 = \boldsymbol{0}\,. \tag{2.12b}$$

The combination of Eqs. (2.11) and (2.12a) forms the foundation of the nutation model of that takes into account internal coupling between inner core, fluid core and

mantle subject to an external torque. Eq. (2.12b) allows us to connect this model to the tilt of the figure axis of the Moon's mantle to the ecliptic. Note that Eq. (2.12a) is different from the one used in DW16; we use here the original equation of the nutation model of *Mathews et al.* [1991] (see their equation 19). Also note that in DW16, Eq. (2.12b) was replaced by a second dynamical equation for the Moon, similar to Eq. (2.11a), but viewed in the ecliptic frame. It was shown that the two dynamical equations for the Moon were tied by the condition expressed in Eq. (2.12b), introduced by *Eckhardt* [1981], and it is more convenient to simply use the latter here.

Definitions for $\boldsymbol{H}$, $\boldsymbol{H_f}$ and $\boldsymbol{H_s}$ are given by

$$\boldsymbol{H} = \boldsymbol{\mathcal{I}} \cdot \boldsymbol{\Omega} + \boldsymbol{\mathcal{I}_f} \cdot \boldsymbol{\omega}_f + \boldsymbol{\mathcal{I}_s} \cdot \boldsymbol{\omega}_s \tag{2.13a}$$

$$\boldsymbol{H}_f = \boldsymbol{\mathcal{I}_f} \cdot \boldsymbol{\Omega}_f \tag{2.13b}$$

$$\boldsymbol{H}_s = \boldsymbol{\mathcal{I}_s} \cdot \boldsymbol{\Omega}_s \tag{2.13c}$$

where $\boldsymbol{\mathcal{I}_s}$, $\boldsymbol{\mathcal{I}_f}$, and $\boldsymbol{\mathcal{I}}$ are the moment of inertia tensors of the solid inner core, fluid core and the whole Moon, respectively. Explicit definitions for these are given in Eq. A9 of DW16; they involve the principal moments of inertia of the whole Moon, fluid core and solid inner core.

We neglect the triaxial shape of the Moon in the development of the expression of the angular momentum vectors of each region. In other words, we assume that the two equatorial moments of inertia are equal to one another and given by the mean values defined in Eq. (2.2). We also neglect elastic deformations. Proceeding this way, the expansion of the angular momentum vectors gives

$$
\begin{aligned}
\boldsymbol{H_s} &= \bar{A}_s \Omega_o \Big[\cos(\theta_m + \theta_s) \hat{\boldsymbol{e}}_{\boldsymbol{3}}^{\boldsymbol{p}} + \sin(\theta_m + \theta_s) \hat{\boldsymbol{e}}_{\perp}^{\boldsymbol{p}}(t) \Big] \\
&\quad + \bar{A}_s e_s \Omega_o \cos(\theta_n - \theta_m - \theta_s) \Big[\cos(\theta_n) \hat{\boldsymbol{e}}_{\boldsymbol{3}}^{\boldsymbol{p}} + \sin(\theta_n) \hat{\boldsymbol{e}}_{\perp}^{\boldsymbol{p}}(t) \Big] ,
\end{aligned}
\tag{2.14a}
$$

$$
\begin{aligned}
\boldsymbol{H_f} &= \bar{A}_f \Omega_o \Big[(1 + e_f) \cos(\theta_m + \theta_f) \hat{\boldsymbol{e}}_{\boldsymbol{3}}^{\boldsymbol{p}} + \sin(\theta_m + \theta_f) \hat{\boldsymbol{e}}_{\perp}^{\boldsymbol{p}}(t) \Big] \\
&\quad - \alpha_1 \bar{A}_s e_s \Omega_o \cos(\theta_n - \theta_m - \theta_f) \Big[\cos(\theta_n) \hat{\boldsymbol{e}}_{\boldsymbol{3}}^{\boldsymbol{p}} + \sin(\theta_n) \hat{\boldsymbol{e}}_{\perp}^{\boldsymbol{p}}(t) \Big] , \\
&\quad + \alpha_1 \bar{A}_s e_s \Omega_o \cos(\theta_m + \theta_f) \hat{\boldsymbol{e}}_{\boldsymbol{3}}^{\boldsymbol{p}}
\end{aligned}
\tag{2.14b}
$$

$$
\boldsymbol{H} = \Omega_o \Big[(C - C_f - C_s) \cos(\theta_m) \hat{\boldsymbol{e}}_{\boldsymbol{3}}^{\boldsymbol{p}} + (\bar{A} - \bar{A}_f - \bar{A}_s) \sin(\theta_m) \hat{\boldsymbol{e}}_{\perp}^{\boldsymbol{p}}(t) \Big] + \boldsymbol{H_f} + \boldsymbol{H_s} ,
\tag{2.14c}
$$

where α_1 is related to the density contrast between the solid and fluid core. The coefficient α_1 and the related coefficient $\alpha_3 = 1 - \alpha_1$ that we introduce below are defined

in Eq. A8 of DW16. For uniform density layers, they simplify to

$$\alpha_1 = \frac{\rho_f}{\rho_s}, \qquad \alpha_3 = 1 - \frac{\rho_f}{\rho_s}. \tag{2.15}$$

As explained in the previous section, the gravitational torque from Earth points in direction $-\hat{e}_3^p \times \hat{e}_\perp^p(t)$. Hence, we can write the gravitational torque acting on the whole of the Moon as

$$\boldsymbol{\Gamma} = -\Gamma \left(\hat{e}_3^p \times \hat{e}_\perp^p(t) \right), \tag{2.16a}$$

where Γ is the amplitude of the torque averaged over one orbit. Valid to second order in ellipticity, it is equal to

$$
\begin{aligned}
\Gamma = {} & \frac{3}{2} \frac{\mathcal{M}n^2}{(1-e_L^2)^{3/2}} \left[(C-A) - (C_s - A_s)\alpha_3 \right] \sin(I+\theta_p)\cos(I+\theta_p) \\
& + \frac{3}{2} \frac{\mathcal{M}n^2}{(1-e_L^2)^{3/2}} \left[(C_s - A_s)\alpha_3 \right] \sin(I+\theta_p+\theta_n)\cos(I+\theta_p+\theta_n) \\
& + \frac{3}{8}\mathcal{M}n^2 \left[(B-A) - (B_s-A_s)\alpha_3 \right] \left(1 - \frac{5}{2}e_L^2 - \left(1+\frac{11}{2}e_L^2\right)\cos(I+\theta_p) \right)\sin(I+\theta_p) \\
& + \frac{3}{8}\mathcal{M}n^2 \left[(B_s-A_s)\alpha_3 \right] \left(1 - \frac{5}{2}e_L^2 - \left(1+\frac{11}{2}e_L^2\right)\cos(I+\theta_p+\theta_n) \right)\sin(I+\theta_p+\theta_n),
\end{aligned}
\tag{2.16b}
$$

where e_L is the orbit eccentricity, n is the mean motion of the Moon, and $\mathcal{M} = M_E/(M+M_E)$, where M_E is the mass of Earth. In the absence of an inner core ($C_s = B_s = A_s = 0$), the torque in Eq. (2.16b) is equal to that given in *Peale* [1969]. Because of the synchronous rotation of the Moon around Earth, the torque involves the full triaxial definition of the moment of inertia. For small $(I+\theta_p)$, the last two terms of Eq. (2.16b) are small compared to the first two terms, and they were neglected in DW16.

Likewise, the torque acting on the inner core can be written as

$$\boldsymbol{\Gamma_s} = -\Gamma_s \left(\hat{e}_3^p \times \hat{e}_\perp^p(t) \right). \tag{2.17a}$$

Valid to second order in ellipticity, the amplitude of the torque Γ_s is

$$\Gamma_s = \frac{3}{2}\frac{\mathcal{M}n^2}{(1-e_L^2)^{3/2}}(C_s - A_s)\alpha_3 \sin(I + \theta_p + \theta_n)\cos(I + \theta_p + \theta_n)$$

$$+ \frac{3}{8}\mathcal{M}n^2(B_s - A_s)\alpha_3 \left(1 - \frac{5}{2}e_L^2 - \left(1 + \frac{11}{2}e_L^2\right)\cos(I + \theta_p + \theta_n)\right)\sin(I + \theta_p + \theta_n)$$

$$+ \Omega_o^2 \bar{A}_s e_s \alpha_3 \alpha_g \sin(\theta_n)\cos(\theta_n)$$

$$+ \Omega_o^2 \bar{A}_s e_s \alpha_1 \sin(\theta_m + \theta_f - \theta_n)\cos(\theta_m + \theta_f - \theta_n)\,, \tag{2.17b}$$

where the coefficient α_g captures the strength of gravitational coupling by the rest of the Moon on a tilted inner core. This coefficient is derived in, and is also defined in Eq. A14b of DW16; for uniform density layers, it simplifies to

$$\alpha_g = \frac{8\pi G}{5\Omega_o^2}\left[\rho_c(\epsilon_r - \epsilon_m) + \rho_m(\epsilon_m - \epsilon_f) + \rho_f\epsilon_f\right]\,, \tag{2.18}$$

where G is the gravitational constant. The first two terms that enter Eq. (2.17b) represent the gravitational torque from Earth. The last two represent, respectively, the gravitational torque from the mantle and fluid core and the pressure torque at the inner-core boundary. In contrast to the torque from Earth, these internal torques involve the mean equatorial moment of inertia. This is because these torques result from the precession between the different layers. Thus, over one orbit, they involve an average of the torque about A_s and B_s.

Using the definition of the torques in Eqs. (2.16) and (2.17), the three angular momentum equations of Eqs. (2.11) and the two kinematic relations of Eqs. (2.12) form the following set of five conditions,

$$\bar{A}\left[\left(\omega - e\cos(\theta_m)\right)\sin(\theta_m)\right]$$

$$+ \bar{A}_f\left[\sin(\theta_f) + \omega\left(\sin(\theta_m + \theta_f) - \sin(\theta_m)\right) - e_f\sin(\theta_m)\left(\cos(\theta_m + \theta_f) - \cos(\theta_m)\right)\right]$$

$$+ \bar{A}_s\left[\sin(\theta_s) + \omega\left(\sin(\theta_m + \theta_s) - \sin(\theta_m)\right) - e_s\sin(\theta_m)\left(\alpha_1\cos(\theta_m + \theta_f) - \cos(\theta_m)\right)\right]$$

$$+ \bar{A}_s e_s \alpha_3 \cos(\theta_n - \theta_m - \theta_f)\left(\omega\sin(\theta_n) + \sin(\theta_n - \theta_m)\right)$$

$$= -\Phi_\beta^p\left(\bar{A}\beta - \bar{A}_s\beta_s\alpha_3\right) - \Phi_\beta^n\bar{A}_s\beta_s\alpha_3 - \Phi_\gamma^p\left(\bar{A}\gamma - \bar{A}_s\gamma_s\alpha_3\right) - \Phi_\gamma^n\bar{A}_s\gamma_s\alpha_3\,, \tag{2.19a}$$

$$\bar{A}_f \Big[\sin(\theta_f) + \omega \sin(\theta_m + \theta_f) + e_f \cos(\theta_m + \theta_f)\Big(\sin(\theta_m + \theta_f) - \sin(\theta_m)\Big)\Big]$$
$$+ \bar{A}_s e_s \alpha_1 \Big[\cos(\theta_n - \theta_m - \theta_f)\Big(-\omega \sin(\theta_n) - \sin(\theta_n - \theta_m) - \sin(\theta_m + \theta_f - \theta_n)\Big)\Big]$$
$$+ \bar{A}_s e_s \alpha_1 \Big[\cos(\theta_m + \theta_f)\Big(\sin(\theta_m + \theta_f) - \sin(\theta_m)\Big)\Big] = 0\,, \tag{2.19b}$$

$$\Big[\sin(\theta_s) + \omega \sin(\theta_m + \theta_s) + e_s \alpha_3 \alpha_g \sin(\theta_n) \cos(\theta_n)\Big]$$
$$+ e_s \cos(\theta_n - \theta_m - \theta_s)\Big[\omega \sin(\theta_n) + \sin(\theta_n - \theta_m)\Big]$$
$$- e_s \cos(\theta_n - \theta_m - \theta_f)\Big[\alpha_1 \sin(\theta_n - \theta_m - \theta_f)\Big]$$
$$= -\Phi_\beta^n \beta_s \alpha_3 - \Phi_\gamma^n \gamma_s \alpha_3\,, \tag{2.19c}$$

$$\omega \sin(\theta_n) + \sin(\theta_m + \theta_s - \theta_n) - \sin(\theta_m - \theta_n) = 0\,, \tag{2.19d}$$

$$\omega \sin(\theta_p) + \sin(\theta_m + \theta_p) = 0\,, \tag{2.19e}$$

where we have defined

$$\Phi_\beta^p = \frac{3}{2}\frac{\mathcal{M}}{(1 - e_L^2)^{3/2}} \sin(I + \theta_p) \cos(I + \theta_p)\,, \tag{2.20a}$$

$$\Phi_\beta^n = \frac{3}{2}\frac{\mathcal{M}}{(1 - e_L^2)^{3/2}} \sin(I + \theta_p + \theta_n) \cos(I + \theta_p + \theta_n)\,, \tag{2.20b}$$

$$\Phi_\gamma^p = \frac{3}{8}\mathcal{M}\left(1 - \frac{5}{2}e_L^2 - \left(1 + \frac{11}{2}e_L^2\right)\cos(I + \theta_p)\right)\sin(I + \theta_p)\,, \tag{2.20c}$$

$$\Phi_\gamma^n = \frac{3}{8}\mathcal{M}\left(1 - \frac{5}{2}e_L^2 - \left(1 + \frac{11}{2}e_L^2\right)\cos(I + \theta_p + \theta_n)\right)\sin(I + \theta_p + \theta_n)\,, \tag{2.20d}$$

and

$$\beta = \frac{C - A}{B} \approx \frac{C - A}{\bar{A}}\,, \qquad \beta_s = \frac{C_s - A_s}{B_s} \approx \frac{C_s - A_s}{\bar{A}_s}\,, \tag{2.21a}$$

$$\gamma = \frac{B - A}{B} \approx \frac{B - A}{\bar{A}}\,, \qquad \gamma_s = \frac{B_s - A_s}{B_s} \approx \frac{B_s - A_s}{\bar{A}_s}\,. \tag{2.21b}$$

Note that the mantle rotation rate Ω_o is approximately equal to the sidereal frequency n and we have set $n = \Omega_o$, which removes a factor of n^2/Ω_o^2 multiplying the right-hand sides of Eqs. (2.19a) and (2.19c). The five conditions of Eqs. (2.19) constitute the set of non-linear conditions on the five angles θ_p, θ_n, θ_m, θ_f and θ_s that must be simultaneously satisfied to determine the complete Cassini state of the Moon. In the limit of small angles,

$$\cos(\theta_i) \to 1\,, \qquad \sin(\theta_i) \to \theta_i\,, \tag{2.22}$$

and for $\Phi_\gamma^p = \Phi_\gamma^n = 0$, we retrieve the linear system of equations presented in DW16, where the parameter $\mathcal{M}$ was omitted, and where the parameter β_s that appears in Eqs. (2.19a) and (2.19c) was approximated as e_s.

For a Moon model with no core, the system of conditions reduces to

$$\bar{A}\Big(\omega - e\cos(\theta_m)\Big)\sin(\theta_m) = -\Phi_\beta^p \bar{A}\beta - \Phi_\gamma^p \bar{A}\gamma\,, \tag{2.23a}$$

$$\omega\sin(\theta_p) + \sin(\theta_m + \theta_p) = 0\,, \tag{2.23b}$$

which can be combined to form

$$\bar{A}\Big(\omega - e\cos(\theta_m)\Big)\Big(-\omega - \cos(\theta_m)\Big)\tan(\theta_p) = -\Phi_\beta^p \bar{A}\beta - \Phi_\gamma^p \bar{A}\gamma\,. \tag{2.23c}$$

Using $C = \bar{A}(1 + e)$, ω defined in Eq. (2.5), and also that $\Omega_p/\Omega_o \ll 1$ and $\theta_m \ll 1$, we retrieve (in our notation) the condition on θ_p given in Eq. (19) of that defines the Cassini state of a single body Moon

$$C\frac{\Omega_p}{\Omega_o}\sin(\theta_p) = \Phi_\beta^p \bar{A}\beta + \Phi_\gamma^p \bar{A}\gamma\,. \tag{2.23d}$$

A condition similar to Eq. (2.23d) but for the inner core of the Moon can be derived. Before we do this, it is convenient to introduce here the frequency of the FICN, ω_{ficn}, which as we show below, turns out to be a fundamental component of the Cassini state of the inner core. The FICN describes the free precession of the spin-symmetry axis of the inner core when it is misaligned from the mantle. The FICN frequency depends on the sum of the torques exerted on the inner core and, when expressed in cycles per Lunar day, it is approximately equal to (see DW16)

$$\omega_{ficn} = e_s\alpha_1 - e_s\alpha_g\alpha_3 - \frac{3}{2}\frac{\beta_s\alpha_3}{(1 - e_L^2)^{3/2}}(\cos^2 I - \sin^2 I)\,. \tag{2.24}$$

For the Moon, the gravitational torque exerted by the fluid core and mantle on the inner core (second term on the right-hand side of Eq. 2.24) is much larger than the pressure torque at the ICB and the gravitational torque from Earth (first and third terms of Eq. 2.24, respectively), so ω_{ficn} is negative and the FICN mode is retrograde.

It is also convenient to derive alternate forms of conditions (2.19d) and (2.19e). First, using the definition of ω in Eq. (2.5) and $\cos(\theta_m) \to 1$ allows one to write the condition of Eqs. (2.19e) as

$$\sin(\theta_m) = \delta\omega \, \sin(\theta_p) \, . \tag{2.25a}$$

This expresses the connection between the misalignment of the rotation vector of the mantle from its figure axis and the tilt of the latter with respect to the ecliptic normal. They are related by the Poincaré number $\delta\omega$. Because the Poincaré number is small, $\theta_m \ll \theta_p$. Using this, the condition of Eq. (2.19d) can be written as

$$\sin(\theta_m + \theta_s - \theta_n) = \delta\omega \, \sin(\theta_p + \theta_n) \, , \tag{2.25b}$$

which is the analogous relationship for the inner core, connecting in the same manner the angle of misalignment of its rotation vector from its figure axis $(\theta_m + \theta_s - \theta_n)$ to the tilt of its figure axis with respect to the ecliptic normal.

The Cassini state of the inner core can be derived on the basis of its angular momentum balance (Eq. 2.19c). Using Eqs. (2.25a-2.25b), and setting $\theta_s \approx \theta_n$ (see DW16), one can show that

$$\sin(\theta_s) + \omega \sin(\theta_s + \theta_m) \approx -\delta\omega \sin(\theta_p + \theta_n) \, , \tag{2.25c}$$

$$e_s \cos(\theta_n - \theta_m - \theta_s) \left[\omega \sin(\theta_n) + \sin(\theta_n - \theta_m)\right] \approx -e_s \delta\omega \sin(\theta_p + \theta_n) \, , \tag{2.25d}$$

so that Eq. (2.19c) can be written as

$$- (1 + e_s) \, \delta\omega \, \sin(\theta_p + \theta_n) \, + \, e_s \alpha_3 \alpha_g \sin(\theta_n) \cos(\theta_n)$$
$$- \, e_s \alpha_1 \cos(\theta_n - \theta_m - \theta_f) \sin(\theta_n - \theta_m - \theta_f) = -\Phi_\beta^n \beta_s \alpha_3 - \Phi_\gamma^n \gamma_s \alpha_3 \, . \tag{2.26a}$$

On using $\delta\omega = \Omega_p/\Omega_o$, $C_s = \bar{A}_s(1 + e_s)$, $\theta_m + \theta_f \approx -\theta_p$ (expressing the fact that the rotation vector of the fluid core remains almost aligned with the ecliptic normal), Eq. (2.26a) becomes

$$\frac{C_s}{\bar{A}_s} \frac{\Omega_p}{\Omega_o} \sin(\theta_p + \theta_n) =$$

$$\Phi^n_\beta \beta_s \alpha_3 \,+\, \Phi^n_\gamma \gamma_s \alpha_3 \,+\, e_s \alpha_3 \alpha_g \sin(\theta_n) \cos(\theta_n) \,-\, e_s \alpha_1 \sin(\theta_n + \theta_p) \cos(\theta_n + \theta_p) \,.$$

$$(2.26b)$$

This last equation determines the Cassini state of the inner core of the Moon. Because internal torques dominate the gravitational torque from Earth in the present-day Moon (DW16), Eq. (2.26b) can be further simplified if we set $\Phi^n_\beta = \Phi^n_\gamma = 0$. As our results will confirm, θ_n is typically much larger than $\theta_p = 1.543°$, so we can approximate $\sin(\theta_n + \theta_p) \cos(\theta_n + \theta_p)$ as $\sin(\theta_n) \cos(\theta_n)$. Furthermore, since the dynamical ellipticity of the inner core is small, $C_s \approx \bar{A}_s$. Upon using the expression of the FICN frequency ω_{ficn} given by Eq. (2.24), the Cassini state of the inner core of the Moon simplifies to

$$\frac{\Omega_p}{\Omega_o} \sin(\theta_p + \theta_n) + \omega_{ficn} \sin(\theta_n) \cos(\theta_n) \,=\, 0 \,. \qquad (2.26c)$$

As we will show, this last equation provides a very good prediction of the tilt angle of the inner core θ_n. Importantly, it shows that the interior density structure of the Lunar interior influences θ_n only through the way in which it affects ω_{ficn}; different interior models of the Moon that share the same ω_{ficn} have the same θ_n.

Before we present results, a few points about our model are worth noting. First, we have neglected all elastic deformations in our derivation, assuming that solid regions are perfectly rigid. The k_2 Love number of the Moon is small, approximately 0.02 [*Williams et al.*, 2014], thus assuming a rigid mantle is not a bad approximation. However, elastic (or viscoealstic) deformations deep inside the Moon may be important.

Second, we have adopted an oversimplified representation of flow motion in the fluid core, restricted to a simple solid body rotation. In truth, the fluid core can sustain different types of waves, including inertial waves, which can interact with, and alter the FCN and FICN precession modes [*Rogister and Valette*, 2009].

Third, although we have retained the triaxial shape of the Moon in the expression of the mean torque from Earth, the angular momentum response is based on axially symmetric model. The convenience of doing this is that, for each region, we can combine the two equatorial angular momentum equations into a single equation. To first order, considering the fully triaxial shape of the Moon should not alter much the frequency of the FCN [*Van Hoolst and Dehant*, 2002]. By extension, we assume here that the other free precession mode with a retrograde period close to one Lunar day (when seen in the rotating mantle frame), the FICN, is also not significantly altered by triaxiality.

Since the orientations of the fluid core spin axis and the inner core spin-symmetry axis are primarily determined by the FCN and FICN frequencies, respectively, our axially symmetric model should, to first order, capture the salient features of the Cassini state.

2.2 Results

2.2.1 Interior Moon models

The numerical values for the Lunar parameters used in our calculations are listed in Table 2.1. To compute all other parameters that enter our rotational model, we need to build models of the interior density structure of the Moon. The first step involves to determine the radial density structure. We assume a mean Lunar radius of $R = 1737.151$ km [*Williams et al.*, 2014]. We then choose values for the inner core radius (r_s), fluid core radius (r_f) and crustal thickness (h_c) and values for the density of the inner core (ρ_s) and crust (ρ_c). The density of the mantle (ρ_m) is then determined by matching the moment of inertia of the solid Moon I_{sm}. The value of I_{sm} from *Williams et al.* [2014] listed in Table 2.1 in principle includes a contribution from the inner core, though it is small compared to that of the outer shell (mantle and crust). Here, we assume that I_{sm} represents the moment of inertia of the mantle and crust alone and calculate ρ_m using Eq. (13) of DW16. The density of the fluid core (ρ_f) is then found by matching the bulk mass of the Moon $M = (4\pi/3)\bar{\rho}R^3$, where $\bar{\rho}$ is the mean density, using Eq. (12) of DW16. Once all radii and densities are defined, the mean equatorial moments of inertia $\bar{A}$, $\bar{A}_f$ and $\bar{A}_s$ are calculated from Eq. (14) of DW16. The second step is to determine the polar (ϵ) and equatorial (ξ) flattenings at all boundaries. These are determined on the basis of the reference Moon model defined in section 2.1 in which the principal moments of inertia of each regions are aligned. We assume that both the ICB and CMB are at hydrostatic equilibrium, in which case their flattenings can be written in terms of the flattenings at the surface and crust-mantle boundary as given by Eqs. (18-20) of DW16. Under this assumption, the expression for J_2 given by Eq. (2.1a) can be written in terms of ϵ_r and ϵ_m, and likewise, C_{22} given by Eq. (2.1b) can be written in terms of ξ_r and ξ_m. We use the surface flattenings $\epsilon_r = 1.2899 \times 10^{-3}$ and $\xi_r = 2.4346 \times 10^{-4}$ corresponding to the (normalized) topography spherical harmonic coefficients c_{20} and c_{22} taken from *Araki et al.* [2009]. The values of ϵ_m and ξ_m are then determined by matching the observed values of J_2 and C_{22} (see Table 2.1). The values of (ϵ_s, ξ_s) and (ϵ_f, ξ_f) are then computed from (ϵ_r, ξ_r) and (ϵ_m, ξ_m) based on the assumption of hydrostatic equilibrium. Once the polar flattening of each boundary is known, α_g can be determined from Eq. (2.18) and the dynamical ellipticities e_s, e_f and e defined in Eq. (2.3) are then computed from Eq. (15) of DW16.

The parameters β and γ defined in Eq. (2.21) that are involved in the torque from Earth are related to J_2 and C_{22} by

Moon Parameter	Numerical value
rotation rate, Ω_o	2.6617×10^{-6} s^{-1}
orbit precession rate, Ω_p	$2\pi/18.6$ yr^{-1}
Poincaré number, $\delta\omega = \Omega_p/\Omega_o$	4.022×10^{-3}
mean planetary radius, R	1737.151 km
mass, M	7.3463×10^{22} kg
mean density, $\bar{\rho}$	3345.56 kg m^{-3}
moment of inertia of solid Moon, I_{sm}	$0.393112 \cdot MR^2$
J_2	2.03504×10^{-4}
C_{22}	2.24482×10^{-5}
polar surface flattening, ϵ_r	1.2899×10^{-3}
equatorial surface flattening, ξ_r	2.4346×10^{-4}

Table 2.1: Reference parameters for the Moon. The values of R, M, $\bar{\rho}$, I_{sm}, J_2 and C_{22} are taken from *Williams et al.* [2014]. The values for the unnormalized potential coefficients J_2 and C_{22} include the permanent tide from synchronous rotation with Earth, and are obtained after multiplying the reported values in *Williams et al.* [2014] by a factor 1.000978 to take into account our choice of using the mean planetary radius as the reference radius for our calculations instead of the reference radius of 1738 km used in the GRAIL-derived gravity field. ϵ_r and ξ_r are taken from *Araki et al.* [2009] and converted to our choice of normalization.

$$\beta = e\left(1 + 2\frac{C_{22}}{J_2}\right), \qquad \gamma = 4e\frac{C_{22}}{J_2}. \tag{2.27}$$

The parameters β_s and γ_s are directly related to the polar and equatorial flattenings at the ICB through

$$\beta_s = \epsilon_s + \frac{\xi_s}{2}, \qquad \gamma_s = \xi_s. \tag{2.28}$$

There is a small inconsistency in our procedure that must be pointed out. The contribution of the inner core to J_2 and C_{22}, as written in Eq. (2.1), assumes an inner core aligned with the mantle. These expressions should really involve the average over one orbit of the polar and equatorial flattenings of a tilted inner core. However, these depend on the angle of tilt of the inner core, which a-priori we do not know. This implies that the amplitude of the torque from Earth on the inner core determined by β_s and γ_s in Eq. 2.28 is slightly incorrect. However, because the torque that the mantle and fluid core exerts on a tilted inner core is much larger than the torque from Earth, this inconsistency has little influence on the results presented in the next section.

2.2.2 The Cassini states associated with the inner core

The set of five conditions in Eqs. (2.19a-2.19e) is solved by a Newton-Raphson method for nonlinear systems. Each solution presented below is obtained with initial guesses for θ_p, θ_m and θ_f taken as $1.5°$, $0°$ and $-1.5°$, respectively. The initial guess for θ_n is set equal to θ_s and chosen randomly between $-90°$ and $90°$. For each set of model parameters, to ensure all possible solutions are found, we repeat the search with a number of random initial guesses for θ_n (typically 50). Solutions for which any of the five angles falls outside the bounds of $[-90°, 90°]$ are discarded.

We also present results based on a small-angle limit of our model, by taking $\cos(\theta_i) \approx 1$ and $\sin(\theta_i) \approx \theta_i$ for each of the five angles, and using the following approximations

$$\sin(I + \theta_p)\cos(I + \theta_p) \approx \cos I \sin I + \left(\cos^2 I - \sin^2 I\right)\theta_p, \tag{2.29a}$$

$$\sin(I + \theta_p + \theta_n)\cos(I + \theta_p + \theta_n) \approx \cos I \sin I + \left(\cos^2 I - \sin^2 I\right)(\theta_p + \theta_n), \tag{2.29b}$$

$$\sin(I + \theta_p) \approx \sin I + (\cos I)\theta_p. \tag{2.29c}$$

In this small-angle limit, the model is now linear in the five unknown angles. Note that this small-angle solution is very close, but not exactly equal to that from the model presented in DW16. The difference is caused by the addition here of the γ and γ_s terms

in the torque from Earth, the inclusion of the factor $\mathcal{M}$ in the amplitude of the torque, and because in DW16 the parameter β_s was approximated as e_s.

Fig. 2.2 shows θ_n, θ_f, θ_p and θ_m obtained from our generalized model and in the small-angle limit. θ_s is not shown, as it is virtually identical to θ_n (the relative difference between the two is of the order of $\delta\omega$). Results are shown for a Moon model with a crust of thickness $h_c = 38.5$ km and density $\rho_c = 2550$ kg m^{-3} an inner core of radius $r_s = 200$ km and density $\rho_s = 7700$ kg m^{-3} [*Matsuyama et al.*, 2016], and a range of possible outer core radius between $r_f = 310$ km and 400 km compatible with seismic studies [*Weber et al.*, 2011; *Garcia et al.*, 2011]. As explained in the previous section, the densities of the fluid core and mantle change for each value of r_f, so as to match M and I_{sm}; from $r_f = 310$ to 400 km, ρ_f changes from 7355.7 to 4772.5 kg m^{-3}, and ρ_m changes from 3376.1 to 3377.9 kg m^{-3}.

The range of r_f values covered in Fig. 2.2 samples different interior Lunar density distributions which in turn samples different frequencies of the FICN, ω_{ficn}. As predicted by Eq. 2.26c, the tilt angle of the inner core should be primarily controlled by ω_{ficn}. The way in which ω_{ficn} (computed from Eq. 2.24) changes for each choice of r_f is shown on the top axis in each panels of Fig. 2.2. For small r_f, ω_{ficn} is slower (in the retrograde direction) than $\delta\omega = \Omega_p/\Omega_o = 4.022 \times 10^{-3}$, the Poincaré number, or the retrograde frequency of the forced precession expressed in cycles per Lunar day. For large r_f, the retrograde ω_{ficn} is instead faster than $\delta\omega$.

The dominant contribution to ω_{ficn}, as given by Eq. (2.24), is from the gravitational coupling term, $-e_s\alpha_3\alpha_g$. The change in ω_{ficn} with r_f shown in Fig. 2.2 is a consequence of the change in ρ_f with r_f in our interior models, which results in a change in both α_3 (see Eq. 2.15) and α_g (see Eq. 2.18). From $r_f = 310$ to 400 km, α_3 changes from 0.0447 to 0.3802, and α_g changes from 105.75 to 85.76. The dynamical ellipticity of the inner core e_s also changes with r_f, but the change is modest, from 1.7865×10^{-4} to 1.8286×10^{-4}.

When $\omega_{ficn} = -\delta\omega$, which occurs at $r_f \approx 347$ km in Fig. 2.2, the FICN mode is in perfect resonance with the forcing period. At that location, solutions in the small-angle limit diverge towards $\pm\infty$. In contrast, solutions from our general model remain finite, even in the proximity of the FICN resonance. Furthermore, although only one solution is possible when $|\omega_{ficn}| < \delta\omega$, three possible solution branches exist for $|\omega_{ficn}| > \delta\omega$. This is analogous to the different possible Cassini states of a single-body Moon first highlighted by *Peale* [1969] who identified four possible states, numbered 1 to 4. *Ward* [1975] showed (his Fig. 2) an example of how states 1, 2 and 4 may have evolved as a function of Earth-Moon distance. State 3 features a tilt angle larger than $\pm 90°$, so a rotation direction opposite to the orbital rotation, and is believed to be unstable when
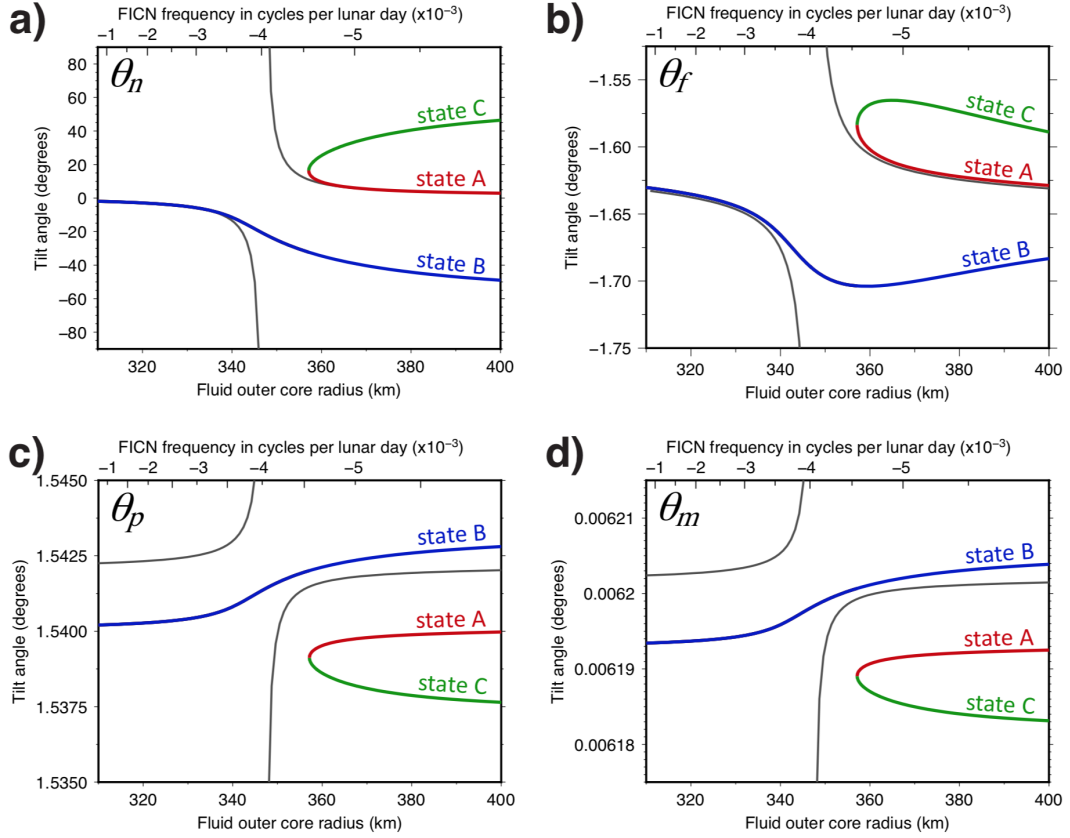
Figure 2.2: The tilt angles (a) θ_n, (b) θ_f, (c) θ_p and (d) θ_m as a function of the fluid core outer radius (bottom axis) and FICN frequency (top axis). The red, blue and green lines correspond to the states A, B and C, respectively, of our general model. The grey line is the solution of the linear system in the small-angle limit. θ_p is measured with respect to the ecliptic normal; θ_n, and θ_m are measured with respect to the mantle frame; θ_f is measured with respect to the mantle frame plus θ_m. Solid inner core radius set at 200 km.

tidal dissipation is taken into account [*Peale*, 1974]. Currently, the Moon – or more formally, the outer solid shell made up of its mantle and crust – occupies state 2, the only state possible when the frequency of the free retrograde precession of the Moon (ω_{fp}) is smaller (in magnitude) than the Poincaré number $\delta\omega$. But in the past when $|\omega_{fp}| > \delta\omega$, states 1, 2, and 4 were all possible solutions. The number of possible Cassini states, and the angle of mantle precession θ_p for each, depends essentially on how ω_{fp} compares with $\delta\omega$ [*Peale*, 1974].

By analogy, the different branches shown on Fig. 2.2 show the different possible Cassini states that are associated with the inner core. The controlling factor to determine which states are possible, and the angle θ_n in each of these states, is how the FICN frequency compares with $\delta\omega$ (see Eq. 2.26c). We have labelled these states A, B and C to avoid a possible confusion with the Cassini states associated with the mantle and crust. State B, the only state possible when $|\omega_{ficn}| < \delta\omega$, features negative values of θ_n: as seen in the Cassini frame, the inner core is tilted away from the mantle, in the direction of the orbit normal. States A and C, which are only possible when $|\omega_{ficn}| > \delta\omega$, instead have $\theta_n > 0$: the inner core is tilted further away than the mantle from the orbit normal. A state which features $90° < |\theta_n| < 180°$ is also a solution (the analogy of state 3 of the solid shell of the Moon), though we deem such a state impossible as it would feature an inner core rotating in reverse direction with the rest of the Moon.

The point of merging between states A and C (at $r_f \approx 357$ km in Fig. 2.2) correspond to a saddle-point bifurcation. States A and C exist for $r_f < 357$ km but as purely imaginary solutions, complex conjugates of one another. Although for $r_f > 357$ km all three states are valid mathematical solutions, state A is preferred because tidal dissipation is expected to drive the system towards its lowest energy state [*Peale*, 1974]. The inner core core would then be in state B for $r_f < 357$ km and state A for $r_f > 357$ km. The transition at $r_f \approx 357$ km marks the location of the maximum possible precession angle of the inner core in each of these states. The solutions shown in Fig. 2.2a suggest that θ_n could be as large as 17° if in state A, or as large as −33° (in the reverse direction) if in state B. The exact value depends on the FICN frequency of the Moon.

The Cassini state of the inner core manifests itself on the other precession angles. θ_f (Fig. 2.2b) shows variations correlated with the variations in θ_n, though much smaller in amplitude. At the transition between states A and B, θ_f varies from −1.59° to −1.71°, a change in amplitude of $\Delta\theta_f = 0.12°$ that is attributable to the inner core. Likewise, θ_p and θ_m (Fig. 2.2c,d) are also adjusted. At the transition between states A and B, the change in amplitude of θ_p attributable to the inner core from state A to B is $\Delta\theta_p = 0.003°$. Note that in all solutions on Fig. 2.2, θ_f is always larger in amplitude than θ_p. In other

words, as seen in the Cassini frame, the spin axis of the fluid core is not exactly aligned with the ecliptic normal, but is tilted towards the orbit normal by a small angle of the order of 0.05° to 0.17° with respect to the ecliptic normal.

Away from the FICN resonance, states A and B converge to the solution in the small angles limit. In fact, provided $|\theta_n| \leq 10°$, or equivalently, provided ω_{ficn} differs from $\delta\omega$ by more than approximately 15%, the small angle approximation is reasonably accurate. Note that there is a small offset between the general solutions and the small angle approximation solutions of θ_p and θ_m. This is caused by the approximations of Eqs. (2.29a-2.29c). Also note that away from the FICN resonance, the solution that we obtain for $\theta_p \approx 1.540°$ does not match the observed mantle tilt angle of 1.543°. This small difference is caused primarily by the omission in our model of the Solar torque acting on the Moon.

According to Eq. 2.26c, the tilt angle of the inner core that characterizes its Cassini state depends on the interior density structure of the Moon but only insofar as it influences the frequency of the FICN. To demonstrate this, Fig. 2.3 shows how θ_n varies as a function of ω_{ficn} for three different choices of inner core radii: 100, 180 and 250 km. In each case, the same range of $r_f = [320, 400]$ km is used. Although the range of ω_{ficn} values that is accessed by each choice of r_s is different, the solution for θ_n versus ω_{ficn} remains unchanged. Eq. 2.26c provides a very good fit to the variations of θ_n as a function of ω_{ficn} shown in Fig. 2.3.

Eq. (2.26c) also reveals why the transition from one to three Cassini states is connected to ω_{ficn}. When the magnitude of ω_{ficn} is smaller than $\delta\omega$ (on the right-hand side of the dashed line in Fig. 2.3), $\sin(\theta_p + \theta_n)$ must be smaller than $\sin(\theta_n)\cos(\theta_n)$, which is only possible if θ_n is negative (state B). Conversely, when the magnitude of ω_{ficn} is larger than $\delta\omega$, $\sin(\theta_p + \theta_n)$ must be larger than $\sin(\theta_n)\cos(\theta_n)$. For θ_n of the same order as θ_p, this is only possible if θ_n and θ_p add up to a larger angle, in other words, if θ_n is positive (state A on Fig. 2.3). For $\theta_n \gg \theta_p$, Eq. (2.26c) becomes

$$\delta\omega + \omega_{ficn}\cos(\theta_n) = 0 \,, \tag{2.30}$$

and this balance is only possible for $|\omega_{ficn}| > \delta\omega$, and admits a pair of solutions $\pm\theta_n$; these are the solutions of states B and C on the left-hand side of the dashed line on Fig. 2.3. Eq. (2.26c) also explains why the transition from one to three Cassini states does not occur precisely at the location of the FICN resonance as it involves trigonometric functions of θ_p and θ_n. The transition is instead displaced to a larger retrograde value of $\omega_{ficn} \approx -0.00455$ in cycles per Lunar day, or $\omega_{ficn} \approx -2\pi/16.4$ yr^{-1}.

Though the branches of solutions of θ_n versus ω_{ficn} are independent of the interior
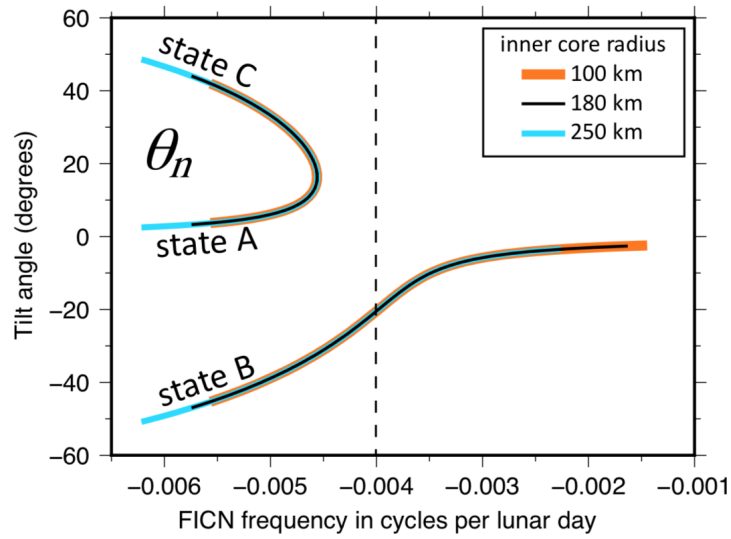
Figure 2.3: The tilt angle of the inner core θ_n as a function of the FICN frequency ω_{ficn}, computed for a range of outer core radii $r_f = [320, 400]$ km and three different choices of inner core radius r_s: 100 km (orange), 180 km (black) and 250 km (light blue). The thickness of each line is varied to reveal that solutions overlie one another. The location of the FICN resonance is indicated by the vertical dashed line.

density structure, it is not the case for θ_p, θ_f and θ_m. For the latter three angles, the degree of separation of the solutions into three distinct branches reflects how the mantle and fluid core adjust in response to a tilted inner core. The amplitude of this response depends on the importance of the inner core in the angular momentum balance of the Moon. To illustrate this, Fig. 2.4 shows how the amplitude of the transition between states A and B for θ_p and θ_f (denoted $\Delta\theta_p$ and $\Delta\theta_f$, respectively) changes as a function of inner core radius. The larger the inner core, the more important its influence is in the angular momentum dynamics of the Moon. Therefore, the greater the manifestation of the Cassini state associated with the inner core is on θ_f and θ_p. For an inner core smaller than 100 km, the Cassini state of the inner core has a vanishingly small influence on θ_f and θ_p. But for an inner core as large as 250 km, $\Delta\theta_p$ gets close 0.01°. This implies that, for a large inner core, the observed mantle tilt angle of 1.543° could include a small though non-negligible contribution from the inner core, the exact amount depending on the inner core size and how close to resonance the frequency of the FICN is. A large inner core has a more dramatic influence on θ_f because the moment of inertia of the fluid core is much smaller than that of the solid shell. For an inner core radius of 250 km, $\Delta\theta_f$ gets as large as approximately 0.5°.

Lastly, it is instructive to show how the shape of the branches of solution change when the geometry of torque by Earth is modified. Fig. 2.5 shows how the branches of solutions of θ_n are altered for three different choices of the orbital inclination: $I = 5.145°$, $I = 2°$ and $I = 0.01°$. As I approaches zero, the point of merging between states A and C approaches the location of the FICN resonance and the transition from three to one state approaches the shape of a pitchfork bifurcation. Eq. (2.26c) remains a very good approximation to the solutions shown in Fig. 2.5; the change in the shape of the solutions occurs because as $I \to 0$, $\theta_p \to 0$.
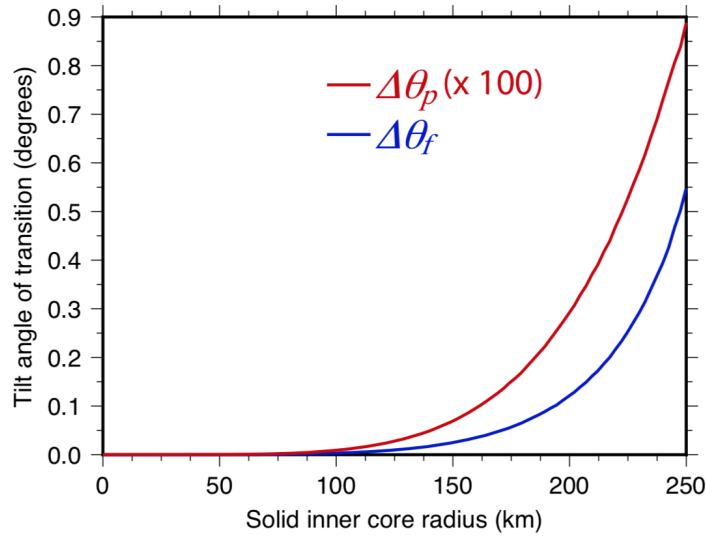
Figure 2.4: The amplitude of change of θ_p (red, multiplied by a factor 100) and θ_f (blue) at the transition between Cassini states A and B associated with the inner core as a function of inner core radius.
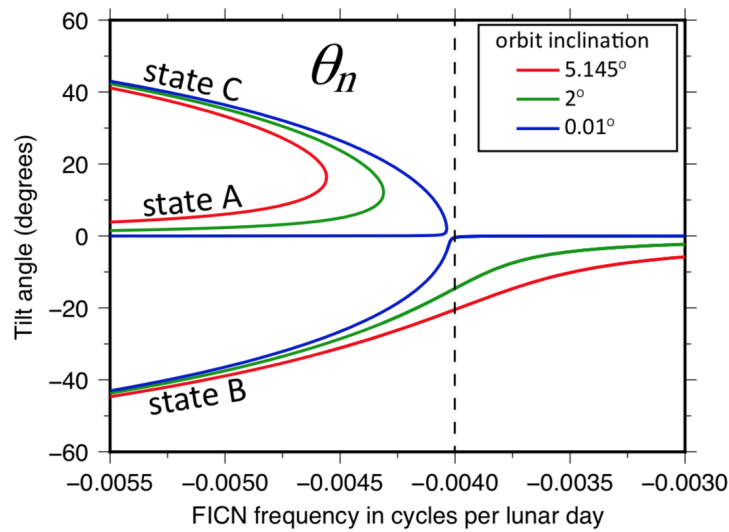

Figure 2.5: The tilt angle of the inner core θ_n as a function of the FICN frequency ω_{ficn} for three different choices of the orbital inclination: $I = 5.145°$ (red); $I = 2°$ (green); $I = 0.01°$ (blue). The location of the FICN resonance is indicated by the vertical dashed line.

2.3 Discussion

We showed in this study that the angle of tilt of the inner core of the Moon that characterizes its Cassini state depends on the frequency of the FICN, ω_{ficn}. More specifically, that it depends on how the magnitude of ω_{ficn} compares with the Poincaré number $\delta\omega = \Omega_p/\Omega_o$. For the present-day Moon, with its rotation rate of $\Omega_o = 2\pi/27.322$ days^{-1} and precession frequency $\Omega_p = 2\pi/18.6$ yr^{-1}, we can cast our results in terms of a comparison between ω_{ficn} and Ω_p both given in frequency units. Denoting the tilt angle of the inner core with respect to the mantle as θ_n, our results show that if $|\omega_{ficn}| \gg \Omega_p$, θ_n is positive but approaches zero (state A on Fig. 2.3 and see also DW16): the inner core remains closely aligned with mantle. If instead $|\omega_{ficn}| \ll \Omega_p$, θ_n is negative and small (state B on Fig. 2.3), but does not converge to zero: a small misalignment with the mantle remains (see DW16). In between these two extremes, θ_n can be large, as the inner core precession is resonantly amplified by the proximity of ω_{ficn} to the forcing frequency Ω_p. Assuming the lowest energy state is favoured, the largest positive θ_n in state A is 17° and the largest negative θ_n in state B is −33°. The transition between these two extremes does not occur exactly at $\omega_{ficn} = -\Omega_p$, but instead at $\omega_{ficn} = -2\pi/16.4$ yr^{-1}.

The precise angle of tilt of the inner core depends then on the knowledge of ω_{ficn}, which in turn depends on the knowledge of the interior structure of the Moon. The uncertainty in the latter is large enough that a considerable range of ω_{ficn} values are possible, from approximately half to twice as large as Ω_p (DW16). This places ω_{ficn} within the resonance band of the forced 18.6 yr precession. Consequently, we expect the inner core to be substantially misaligned with the mantle. As an illustrative example, let us calculate the FICN frequency for one possible interior structure model. We pick as a basis one of the model presented in *Matsuyama et al.* [2016], specifically the model in their Table 2 without a low velocity layer at the bottom of the mantle, and constrained to match the Lunar mass, the moment of inertia, and the observed values of k_2 and h_2 (and the model for which h_2 is derived from LLR). Using the central values for the density and radius of each layer, the central values for the densities of the inner core and crust, we find ρ_m= 3358 kg/m^3 and ρ_f= 5878.6 kg/m^3 from fitting I_{sm} and M by the method described in section 3.1. These are compatible with the range of values of ρ_m and ρ_f given in Table 2 of *Matsuyama et al.* [2016]. The FICN frequency that we calculate for this specific model is $\omega_{ficn} = -2\pi/19.48$ yr^{-1}. According to our adopted denomination, the inner core would be in state B and its tilt angle (predicted by Eq. 2.26c) would be approximately −17.16°. That is, as seen in the Cassini frame, the inner core is offset from the mantle axis by $\sim$ 17°, towards the ecliptic normal (Fig. 2.6).
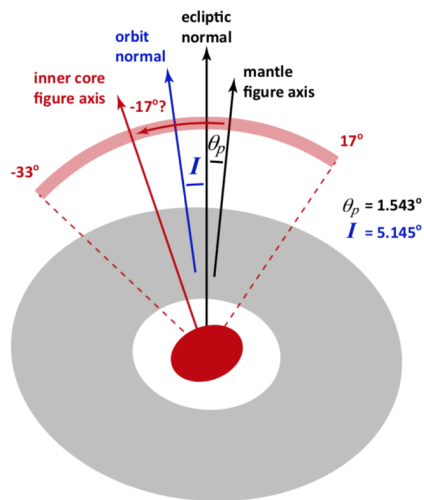
Figure 2.6: The Cassini state of the inner core, as seen in the Cassini frame. The red shaded arc shows the possible range of inner core precession angles, from $+17°$ to $-33°$, measured with respect to the mantle figure axis. Adopting a Lunar interior density model close to that of *Matsuyama et al.* [2016] gives a precession angle of $-17°$. Angles, ellipticities and region thicknesses are not drawn to scale.

However, because of the proximity of ω_{ficn} to Ω_p, the precise value of the inner core tilt is very sensitive to small changes in the interior density structure. So we must emphasize that the uncertainty on the inner core precession angle remains large, and it could take any values between $-33°$ and $17°$ (Fig. 2.6). Additionally, we have assumed here the mantle to be a simple one layer model. The latest models of the Lunar interior allow for a higher density, low seismic velocity layer at the bottom of the mantle [*Weber et al.*, 2011; *Matsuyama et al.*, 2016], which would further influence the exact frequency of the FICN, and thus the tilt angle of the inner core.

Our results also indicate that if the inner core is sufficiently large, it can contribute to the observed tilt angle of the solid outer shell of the Moon of $\theta_p = 1.543°$. By exactly how much depends on the inner core size and how close the FICN frequency is to resonance. Because the inner core tilt can be either positive (if in state A) or negative (if in state B), it can lead to either a negative or a positive contribution to θ_p, respectively. For an inner core as large as 250 km, this contribution could be of the order of $\pm0.005°$. Conversely, this implies that parameters inferred from fitting the observed θ_p can take different numerical values when determined on the basis of a Moon model with a large inner core versus one with a small or no inner core. This is the case notably for the parameter β given in Eq. (2.21). Since β involves the moments of inertia, a change in its numerical value corresponds to a different constraint on the Moon's interior structure. Consequently, interior models constructed on the basis of this constraint would then also be altered.

Likewise, a large inner core can induce a substantial change in the orientation of the rotation vector of the fluid core. The latter is typically assumed to be closely aligned with the ecliptic because the frequency of the FCN is much smaller than the forcing precession frequency [*Meyer and Wisdom*, 2011]. But as we have shown here, if the FICN frequency is very close to the resonance, a large inner core can entrain a significant misalignment of the fluid core spin axis from the ecliptic of the order of $\pm0.2°$. One improvement to our model would be to include elastic deformations, which we have neglected. The prediction of the mantle tilt angle in our model is $\theta_p \approx 1.540°$, off by approximately 0.19% from the observed tilt of $\theta_p = 1.543°$, dominantly because we have neglected the torque from the Sun. Including elastic deformations would not contribute to a large additional correction to θ_p, but changes in the tilt angles of the inner core and fluid core could be more important. The largest force acting on a tilted inner core is from gravitational coupling with the mantle and fluid core. Elastic deformations would act to realign the inner core with the mantle, so would lead to a decrease in the inner core tilt angle. The range of possible inner core tilt angles quoted above, from $-33°$ to

$17°$, could be slightly diminished.

Perhaps more importantly, viscous relaxation within the lower portion of the mantle [*Harada et al.*, 2014] or within the inner core may also substantially alter our results. In particular, an inner core that can deform viscously would realign its shape to match the surface of hydrostatic equilibrium imposed by the mantle gravity field. As was shown in DW16, if the viscous relaxation timescale of the inner core is of the order of one Lunar day, gravitational coupling with the mantle would prevent a misalignment of the inner core of more than $1°$.

Another process that acts to realign the ICB to the surface of hydrostatic equilibrium imposed by the mantle is melting and crystallizing at the top of the inner core. Within the fluid core, hydrostatic equilibrium implies that surfaces of constant gravitational potential, density and pressure are all aligned. Linked to pressure and density by an equation of state, surfaces of constant temperature follow the same alignment. The ICB marks the transition from the solid to liquid phase of the core Fe-alloy, so at equilibrium its temperature should coincide with the liquidus (melting temperature). A tilted ellipsoidal inner core however has its ICB misaligned from the liquidus (Fig. 2.7). Parts of the ICB that are at a higher radius than the liquidus undergo melting, parts that are at a lower radius are the seat of crystal growth. A tilted inner core is precessing at frequency $\omega\Omega_o$ in the frame of the mantle, so over the course of one Lunar orbit around Earth, a given point on the ICB goes through a cycle of melting and crystallizing. At each moment in this cycle, melt or growth of the ICB is always directed towards an alignment with the liquidus. Over a long period of time, this should act to realign the shape of the ICB with the liquidus, and thus to realign the figure axis of the inner core with that of the mantle.

These considerations have not been taken into account in our model. A more proper determination of the tilt angle of the inner core would involve a balance between two characteristic timescales: the timescale of realignment of the ICB to the liquidus by melt and growth versus the timescale for the inner core to assume the tilt angle of its Cassini state when starting from an alignment with the mantle.

The important point to stress is that both viscous relaxation and the process of melting and solidification of the ICB act to reduce the amplitude of the inner core tilt predicted by our simple model. Indeed, this may be part of the reason why the periodic degree 2 and order 1 gravity signal associated with the inner core, which is expected to be above detection level [*Williams*, 2007; *Zuber et al.*, 2013], has so far remained undetected [*Williams*, 2015]. In fact, for the interior model with a predicted inner core tilt of $-17°$ presented above, this signal should be of the order of $2 - 3 \times 10^{-10}$, large enough enough to be detected. The non-detection of this gravity signal may then reflect
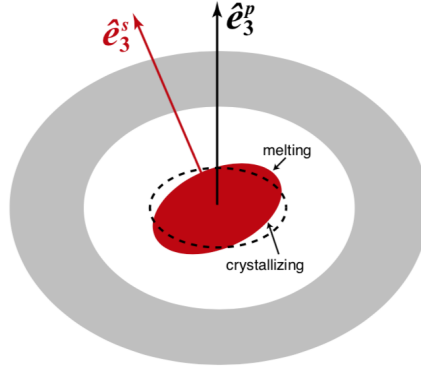
Figure 2.7: The surface of a tilted ellipsoidal inner core (red) with respect to the mantle figure (grey) is misaligned with the liquidus temperature (dashed line). Regions of the inner core boundary at a larger (smaller) radius than the liquidus experience melting (crystallizing). Ellipticities and region thicknesses are not drawn to scale.

the importance of viscous relaxation or melting/solidification acting to reduce the inner core tilt. Alternately, the non-detection may be because the inner core is too small, the density contrast at the ICB is too small, or that the FICN frequency is not near the resonance so the inner core tilt is too small.

We have applied our model of the Cassini state of the inner core to the present-day orbital configuration of the Moon. But the orbit of the Moon has evolved with time. The rotation rate of the 1:1 spin-orbit resonance has decreased as the Earth-Moon distance increased. This implies a change in the FICN frequency with time. Likewise, the orbital precession frequency, and thus the forced precession frequency, is also changing in time. For a fixed Lunar interior structure, the changing ratio of ω_{ficn} to Ω_p implies that the tilt angle of the inner core is expected to also change in time. It is even possible that a transition from one Cassini state to another may have occurred in the past, or will occur in the future. In fact, Fig. 2 of *Ward* [1975] illustrates precisely this, showing how the different Cassini states associated with the solid outer shell of the Moon have evolved as a function of the Earth-Moon distance. The transition between states 1 ($\theta_p < 0$) and 2 ($\theta_p > 0$) marks the resonance crossing of the free precession of the Lunar mantle in space. This will be investigated in the next chapter.

These results are important in regards to the origin of the past Lunar dynamo [*Weiss and Tikoo*, 2014]. One suggestion that has been proposed is that the dynamo may have

been sustained by mechanical forcing from differential rotation at the CMB [*Williams et al.*, 2001; *Dwyer et al.*, 2011], when the tilt angle of the spin symmetry axis of the mantle with respect to the ecliptic was larger [*Ward*, 1975]. In this model, the fluid core spin axis is assumed to be perfectly aligned with the ecliptic normal. But as we showed in our study, the fluid core spin axis may be sufficiently offset from the ecliptic if the inner core is large and the FICN frequency is close to resonance. Furthermore, in the past, the FCN frequency was larger, principally because of the faster rotation rate of the Moon [*Meyer and Wisdom*, 2011], and thus the FCN was closer to being in resonance with the forced precession frequency. Consequently, even for a small or no inner core, the offset of the fluid core spin axis with the ecliptic was larger in the past, thus enhancing the power available to drive a mechanical Lunar dynamo. The factor of enhancement depends on the Lunar interior model and on the details of the evolution of the Lunar orbit.

Since, as we have illustrated in our study, the spin vectors of the solid and fluid cores are likely misaligned, it follows then that the resulting differential rotation at the ICB may also potentially lead to a dynamo by mechanical stirring. Clearly, if this mechanism is possible, then the differential velocity at the ICB at present is too small for dynamo action, either because the inner core is too small, or because the differential precession angle between the inner core and the spin axis of the fluid core is too small, or both. But if it is because of the latter, the different ratio between ω_{ficn} and Ω_p in the past may have lead to a much larger inner core tilt – even possibly a resonance crossing of the FICN – and a sufficiently large differential rotation at the ICB for dynamo action. Whether this may have occurred depends on the evolution of the Lunar orbit parameters, the Lunar interior structure and on how the latter may have evolved (for instance by inner core growth). This will also be a point of focus of the next chapter.

Chapter 3

Mechanical stirring as a source of dynamo action

One of the proposed mechanisms to explain the ancient dynamo of the Moon is that it may have been produced by mechanical stirring from the precessional motion of the fluid outer core with respect to the mantle. Because of the elliptical shape of the CMB and secondarily because of the viscous friction, a precession of the fluid core cannot be represented by a simple rigid body rotation [*Tilgner*, 2015]. A boundary layer flow must be present, which may be confined to the boundaries but may destabilize the flow in the whole volume. Moreover the Reynolds number of the core precession is of the order of 10^{10} [*Williams et al.*, 2001] and turbulent instabilities are expected to develop. The geometry of the flow is important to generate and maintain a magnetic field by dynamo action [*Jones*, 2015]. Whether a dynamo can be produced by precession and the form of the flows that are most suited to do so is an active area of research [*Tilgner*, 2005; *Malkus*, 1968; *Cébron et al.*, 2018]. An example of such a flow driven by precession is displayed in Fig. 3.1. The magnetic field resulting from such a system is rarely dipolar. Due to the turbulence at the CMB, the dynamo is instead dominated by small scale magnetic fields [*Cébron et al.*, 2018].

Here, instead of investigating the details of the flow that can generate a dynamo, we look at the basic energy balance. The power required to generate a dynamo must be equal to the ohmic dissipation in the core [*Nimmo*, 2015]. Hence, without investigating whether the flows generated by the precession can sustain a dynamo, a simpler question is to ask whether there is sufficient energy.

This was the purpose of the study done by *Dwyer et al.* [2011]. They used the dissipation from viscous torque at the CMB predicted from LLR [*Williams et al.*, 2001]
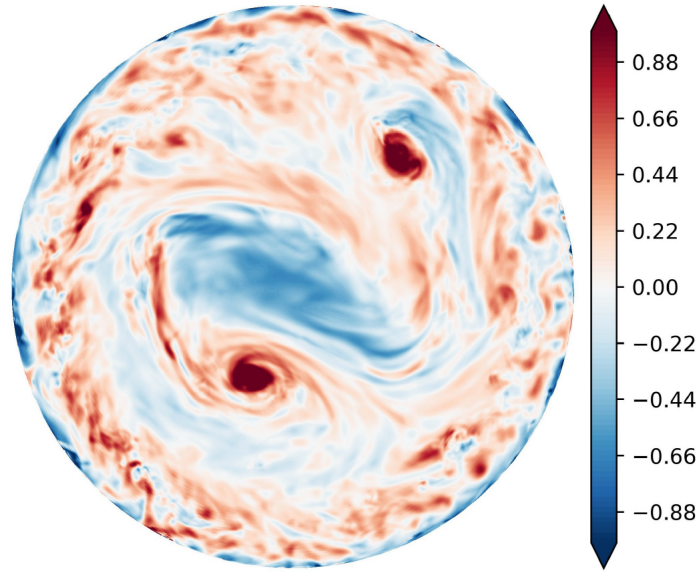
Figure 3.1: An example of a flow pattern resulting from a precessing spherical shell, represented as vorticity along the fluid's rotational axis, without the presence of a solid inner core. From *Cébron et al.* [2018].

and estimated a magnetic field strength in the Lunar past based on the basis of a power scaling law derived from convective dynamos. In this chapter, we extend this idea to differential motion at the ICB. We investigate whether the precessional motion of the inner core and fluid core may have lead to sufficient dissipation in the past to have generated a dynamo, and if so, what was the strength of the magnetic field.

3.1.1 Viscous torque from laminar flow

Estimates of the power dissipation can be derived from the viscous torque at the CMB and ICB. Let us first explore the viscous torque based on the assumption of laminar flow. While we do not expect the flow in the fluid outer core to be laminar, it provides a good foundation for the derivation of the turbulent torque at the CMB and ICB that will be presented in the next section. We begin with the definition of viscous shear stress, representing the traction exerted on a solid boundary

$$\boldsymbol{\tau} = \rho_f \nu \frac{\partial}{\partial z} \mathbf{u} \,, \tag{3.1}$$

where ρ_f is the density of fluid core, ν is the kinematic viscosity and $\mathbf{u}$ is the velocity profile of the flow. For rotating flows, the latter is assumed to be of the form [*Pedlosky, 1987*],

$$\boldsymbol{u}(z) = \left[1 - e^{-z/\delta}\cos\frac{z}{\delta}\right]\boldsymbol{u_0} + \sin\frac{z}{\delta}e^{-z/\delta}\hat{\boldsymbol{z}} \times \boldsymbol{u_0} \ , \tag{3.2}$$

where z is the vertical distance away from the boundary and into the fluid, $\delta = \sqrt{\nu/\Omega_0}$ is the Ekman depth, and $\mathbf{u_0}$ is the flow in the mean stream. The differential velocity between the solid boundary and the bulk of the flow is thus equal to $\mathbf{u_0}$. For the rotational flows involved in precession, the maximum differential velocity at the CMB and ICB can be written as

$$\left|\mathbf{u_0^{cmb}}\right| = r_f\Omega_0\left|\sin\theta_f\right| \ , \tag{3.3a}$$

$$\left|\mathbf{u_0^{icb}}\right| = r_s\Omega_0\left|\sin\left(\theta_f - \theta_s\right)\right| \ . \tag{3.3b}$$

Taking the derivative of Eq. (3.2) with respect to z we obtain an expression for the viscous shear stress in terms of the differential velocity $\mathbf{u_0}$,

$$\boldsymbol{\tau} = \rho\sqrt{\nu\Omega_0}[\mathbf{u_0} + \hat{\mathbf{z}} \times \mathbf{u_0}] \ . \tag{3.4}$$

Integrating the viscous shear stress over a sphere gives the torque exerted on the solid boundary at that radius. The viscous torques exerted on the mantle at the CMB (Γ_{cmb}) and on the inner core at the ICB (Γ_{icb}) can be written as [*Mathews and Guo*, 2005]

$$\Gamma_{cmb} = i\Omega_0^2\bar{A}_f\mathcal{K}_{cmb}\sin\theta_f \ , \tag{3.5a}$$

$$\Gamma_{icb} = i\Omega_0^2\bar{A}_s\mathcal{K}_{icb}\sin\left(\theta_f - \theta_s\right) \ , \tag{3.5b}$$

where the non-dimensional coupling constants $\mathcal{K}_{cmb}$ and $\mathcal{K}_{icb}$ are given by:

$$\mathcal{K}_{cmb} = \frac{1}{\sqrt{2}}\pi\frac{r_f^5\rho_f^{cmb}}{A_f}E_{cmb}^{\frac{1}{2}}(0.195 - 1.976i) \ , \tag{3.6a}$$

$$\mathcal{K}_{icb} = \frac{1}{\sqrt{2}}\pi\frac{r_s^5\rho_f^{icb}}{A_s}E_{icb}^{\frac{1}{2}}(0.195 - 1.976i) \ . \tag{3.6b}$$

In the above expressions, E_{cmb} and E_{icb} are the Ekman numbers based on the CMB and ICB radii respectively, given by

$$E_{cmb} = \frac{\nu}{r_f^2\Omega_0} \ , \qquad E_{icb} = \frac{\nu}{r_s^2\Omega_0} \ . \tag{3.7}$$

An equivalent form for the coupling constants is then

$$\mathcal{K}_{cmb} = \frac{\pi}{\sqrt{2}} \frac{r_f^4 \rho_f^{cmb}}{A_f} \frac{1}{\Omega_0} \sqrt{\nu \Omega_0} (0.195 - 1.976i) \ , \tag{3.8a}$$

$$\mathcal{K}_{icb} = \frac{\pi}{\sqrt{2}} \frac{r_s^4 \rho_f^{icb}}{A_s} \frac{1}{\Omega_0} \sqrt{\nu \Omega_0} (0.195 - 1.976i) \ . \tag{3.8b}$$

3.1.2 Viscous coupling from turbulent flow

In the case of turbulent flow, the shear stress at the boundary can be written as

$$\boldsymbol{\tau} = f\rho \left| \mathbf{u_0} \right| \mathbf{u_0} \ , \tag{3.9}$$

where f is a dimensionless coefficient of friction, and $\mathbf{u_0}$ again is the mean stream flow away from the boundary layer. A comparison between Eqs. (3.4) and (3.9) reveals that the expression for the traction in the direction of $\mathbf{u_0}$ in the turbulent case involves substituting a term $\sqrt{\nu \Omega_0}$ by $f \left| \mathbf{u_0} \right|$. Using the same substitution in the expressions for the coupling constants (Eq. (3.8)), they become

$$\mathcal{K}_{cmb}^t = \frac{\pi}{\sqrt{2}} \frac{r_f^5 \rho_f^{cmb}}{A_f} f \left| \sin \theta_f \right| (0.195 - 1.976i) \ , \tag{3.10a}$$

$$\mathcal{K}_{icb}^t = \frac{\pi}{\sqrt{2}} \frac{r_s^5 \rho_f^{icb}}{A_s} f \left| \sin (\theta_f - \theta_s) \right| (0.195 - 1.976i) \ . \tag{3.10b}$$

The friction coefficient f depends on the surface roughness and may be different at the ICB versus the CMB. In the next section we show how f can be estimated from LLR observations. In principle, we can include the viscous torques in our angular momentum system defined in Eq. (2.11). However dissipation in the Moon is weak and therefore can be neglected in a first order calculation of our system. The solutions of θ_f and θ_s from the Cassini states found from the method derived in the previous chapter can be used to find the values of $\mathcal{K}_{cmb}^t$ and $\mathcal{K}_{icb}^t$.

3.1.3 Constraints on viscous torque from LLR observations

Constraints from viscous friction at the CMB of the Moon at present day can be derived from LLR observations [*Williams et al.*, 2001]. The rotational model of the Moon used to fit LLR data simply consists of a rigid mantle and a fluid core. Viscous dissipation is incorporated into the model by adding a viscous torque on the mantle in the form

$$\Gamma_{cmb} = \mathcal{K}(\Delta \omega_{cmb}) \ , \tag{3.11}$$

where $\mathcal{K}$ is a dimensionless coupling coefficient between the mantle and fluid core, and $\Delta\omega_{cmb}$ is the differential angular velocity at the CMB. From LLR data, along with data from the GRAIL mission, a recent estimate of $\frac{\mathcal{K}}{C}$ is [*Williams et al.*, 2014]

$$\frac{\mathcal{K}}{C} = (1.64 \pm 0.17) \times 10^{-8} \text{days}^{-1} = (1.9 \pm 0.20) \times 10^{-13} \text{s}^{-1} \ , \tag{3.12}$$

where C is the polar moment of inertia of the whole Moon. Note that this model is derived assuming no solid inner core, meaning that both $\mathcal{K}^t_{cmb}$ and $\mathcal{K}^t_{icb}$ are mapped into this single value of $\frac{\mathcal{K}}{C}$. Unfortunately, separating this friction coefficient into CMB and ICB components is complicated and beyond the scope of this thesis and will be left for a future study. We will use $\frac{\mathcal{K}}{C}$ as given by Eq. (3.12), in order to derive, in an order of magnitude sense, a numerical value for the friction parameter f that enters Eqs. (3.10). Defining the differential angular velocity at the CMB associated with the Cassini state as

$$\Delta\omega = \Omega_0 \sin\theta_f \ , \tag{3.13}$$

and equating the torque in Eq. (3.11) to our definition of the torque at the CMB given in Eq. (3.5a) we obtain

$$Im(\mathcal{K}^t_{cmb}) = -\frac{\mathcal{K}}{C}\frac{C}{C_f}\frac{1}{\Omega_0} \ . \tag{3.14}$$

Approximating the ratio between polar moment of inertia of the whole moon and fluid outer core (C/C_f) as $\bar{A}/\bar{A}_f$, Eq. (3.14) can be expressed as

$$Im(\mathcal{K}^t_{cmb}) = -1.976\frac{\pi}{\sqrt{2}}\frac{r_f^5\rho_f^{cmb}}{\bar{A}_f}f\left|\sin\theta_f\right| \ . \tag{3.15}$$

Using the definition of $\mathcal{K}^t_{cmb}$ given in Eq. (3.10a), f is found to be equal to

$$f = \frac{\mathcal{K}}{C}\frac{\bar{A}\sqrt{2}}{1.976\Omega_0\pi r_f^5\rho_f^{cmb}\sin\theta_f} \ . \tag{3.16}$$

It is worth noting that in the above equation, we are trying to match the parameter f for today's Lunar system, and in doing so need to use present day values for Ω_0 and θ_f, where $\Omega_0 \approx 2.6616 \times 10^{-6} \text{ s}^{-1}$. We can easily calculate θ_f values using our non-linear Cassini state model described in the previous chapter, however since θ_f for today is about $-1.6°$ and doesn't vary much with Lunar model, we will assume that $\theta_f = -1.6°$ for todays value in the calculation of f. For each interior model that we use, the present day value of f that we calculate is consistent with the observations from GRAIL and LLR. We then assume that this friction parameter defines properties of the solid-fluid boundary and has remained unchanged going back in the past.

3.1.4 Dissipation

Viscous dissipation can be calculated as the product of the torque and the angular velocity at a given boundary,

$$Q = \mathbf{\Gamma} \cdot \Delta\boldsymbol{\omega} \; , \tag{3.17}$$

where $\Delta\boldsymbol{\omega}$ is the differential angular velocity. At the CMB, $|\Delta\boldsymbol{\omega}| = \Omega_0 \sin\theta_f$. Taking the real part of Γ_{cmb} in Eq. (3.5a) and $\mathcal{K}^t_{cmb}$ from Eq. (3.10a) gives us the dissipation at the CMB

$$Q_{cmb} = 1.976 \frac{\pi}{\sqrt{2}} r_f^5 \rho_f f \left| \Omega_0 \sin\theta_f \right|^3 \; . \tag{3.18}$$

In a similar fashion, the dissipation at the ICB can be calculated from Γ_{icb} in Eq. (3.5b) and $\mathcal{K}^t_{icb}$ from Eq. (3.10b):

$$Q_{icb} = 1.976 \frac{\pi}{\sqrt{2}} r_s^5 \rho_f f \left| \Omega_0 \sin(\theta_f - \theta_s) \right|^3 \; . \tag{3.19}$$

The dissipation can now be estimated on the basis of the solutions of θ_s and θ_f from our Cassini state model of chapter 2. The one parameter which is highly uncertain in this calculation is the friction coefficient f. Even though our estimate of this parameter is retrieved from LLR, it needs to be emphasized that it only represents an order of magnitude at best. Hence, our calculations of the dissipation at the CMB and ICB presented in the next section should be viewed as order of magnitude estimates.

3.2 Results

As in the previous chapter on the Cassini state of the inner core, we have a rather large parameter space to investigate, especially when considering how these variables change over Lunar history. The main focus of this study is to see how dissipation and magnetic field intensity vary over time. First, we determine which orbital parameters have changed and how they vary as a function of time. Next, the relationship between the dissipation at the CMB and the ICB, as well as their associated magnetic fields will be investigated as a function of time, and compared to the model by *Dwyer et al.* [2011]. Finally, we will take distinct periods in the past to see how the dissipation and the resulting magnetic fields vary as a function of Lunar parameters at specific moments throughout Lunar history.

3.2.1 Evolution of the Lunar orbit

In chapter 2, we used numerical values appropriate for today's Lunar orbital inclination of $I = 5.145°$, precession frequency of $\Omega_p = 2\pi/18.6 \text{ yr}^{-1}$ and sidereal frequency of $\Omega_0 = 2\pi/27.322 \text{ days}^{-1}$. However I, Ω_p and Ω_0 had different values in the past. To calculate the past Lunar Cassini states we must first determine how the aforementioned variables have varied through time. *Touma and Wisdom* [1994] have carried out numerical integrations of the tidal evolution of the Earth-Moon system and have constrained many orbital and rotational parameters thus allowing the extension of our model int the past. For instance, Figs. 3.2 and 3.4 show how the precession period and inclination I have changed as a function of Earth-Moon distance.
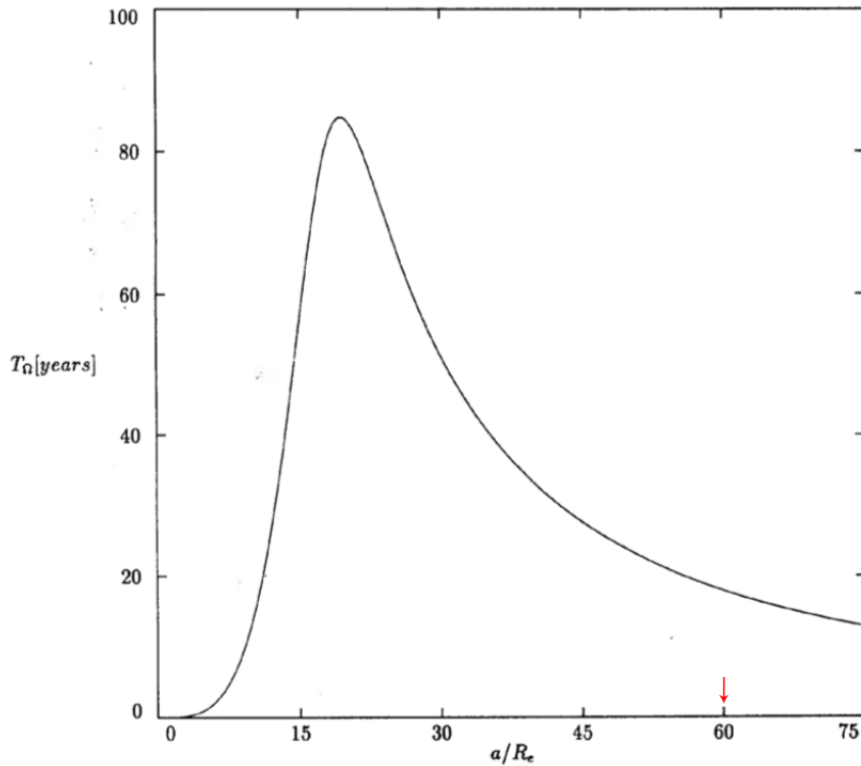

Figure 3.2: Precession period of the Moon, with both Lunar and solar tides accounted for, as a function of semi-major axis expressed in Earth radii. Present day orbital radius shown with the red arrow. From *Touma and Wisdom* [1994].

As Fig. 2.5 in chapter 2 shows, the impact of orbital inclination on the Cassini state of the inner core can be rather significant. However, Fig. 3.4 shows that changes in I

have not been significant after $a_L > 33\ R_E$, where R_E is the Earth's radius. To simplify, we will assume that I has remained constant (and equal to 5.145°) and restrict our investigation in the past to Lunar orbital radii greater than 33 R_E. The same assumption was made by *Dwyer et al.* [2011].

As for the mean sidereal period, Ω_0, assuming the Moon to be tidally locked into a 1:1 spin orbit resonance, using Kepler's 3rd law, the rotational frequency of the Moon in the past $(\Omega_0(a_L))$ when the Moon was orbiting at a distance of a_L is given by

$$\Omega_0(a_L) = \left[\frac{a_0}{a_L}\right]^{3/2} \Omega_0(a_0)\ , \tag{3.20}$$

where a_0 is the present-day semi-major axis. Relating the semi-major axis to time is a difficult problem and many different models exist. The temporal evolution of the Lunar orbit depends highly on tidal dissipation on the Earth. Geological observations of dissipation span up until about 0.6 Gyr ago, prior to which little can be accurately constrained [*Williams*, 2000]. Consequently the evolution of the Earth-Moon system in its early stages remains uncertain. For this reason, we will only show how our results vary as a function of Lunar orbital radius, and will not attempt to translate them in terms of a specific timescale. This means that the exact time correlation of our predicted magnetic field and paleomagnetic data cannot be calculated with great certainty. A few models showing how the semi-major axis evolved as a function of time are shown in Fig. 3.3, which delineates the non-uniqueness when converting Lunar semi-major axis into time before present.

3.2.2 Evolution of Lunar Cassini states

Before delving into power dissipation and magnetic field intensities, we find it useful to examine the evolution of the Cassini states as a function of orbital radius. Using the same model as in chapter 2 but with different values of Ω_p (from Fig. 3.2), Ω_0 (from Eq. (3.20)) as a function of a_L, Fig. 3.5 shows an example of how the tilt angle of the mantle (θ_p), the spin axis of the fluid core (θ_f) and the inner core (θ_s) have evolved. This particular Moon model has a fluid outer core radius of $r_f = 350$ km and a solid inner core radius of $r_s = 250$ km. The densities of the inner core and crust are set at $\rho_s = 7700$ kg/m^3 and $\rho_c = 2550$ kg/m^3, respectively, with a crust thickness of 38.5 km. Fig. 3.5 shows the magnitude of the tilt angle of the mantle can reach up to 45°, consistent with the results shown in *Ward* [1975]. The variation of θ_f is slightly larger and tracks the changes in θ_p, though with the reverse sign. Recall that θ_f is measured from the mantle frame, so the rotation axis of the fluid core remains close to the ecliptic normal, except
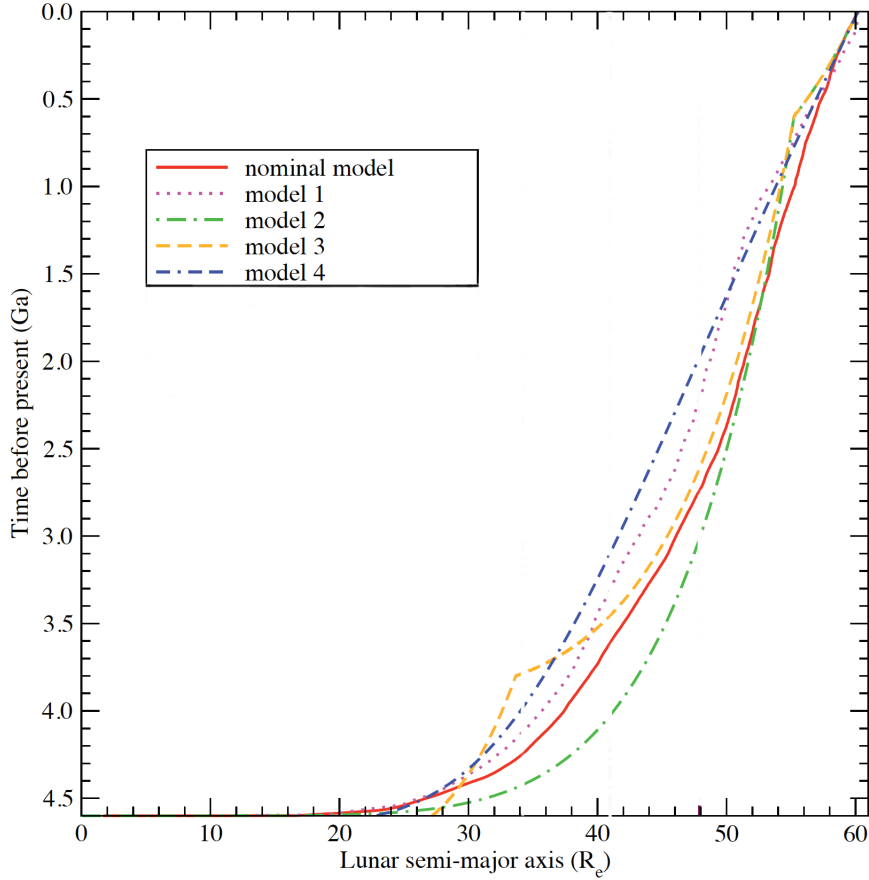
Figure 3.3: A variety of models displaying the evolution of Lunar semi-major axis as a function of time. The model in red is the one chosen for the study done by *Dwyer et al.* [2011]. Figure from *Dwyer et al.* [2011].

for $a_L < 40$ R_E where it may have been offset by up to 10° (Fig. 3.5, bottom). In the same manner that Fig. 2.3 in chapter 2 shows that the different branches of the Cassini state associated with the inner core can be accessed depending on the FICN frequency, Fig. 3.5 shows that different branches can also be accessed by changing Ω_p and Ω_0. Note also that there are multiple Cassini states that the solid inner core can inhabit in the recent past, but for this specific Moon model, only state B was possible for $a_L < 53$ R_E. Assuming that the lowest energy state is favoured, this implies that as the Moon moved away from the Earth, a transition at around 53 R_E would have occurred.

Whether such a Cassini state transition occurred depends on the interior Moon model, more specifically it depends on whether the FICN frequency of the Lunar model
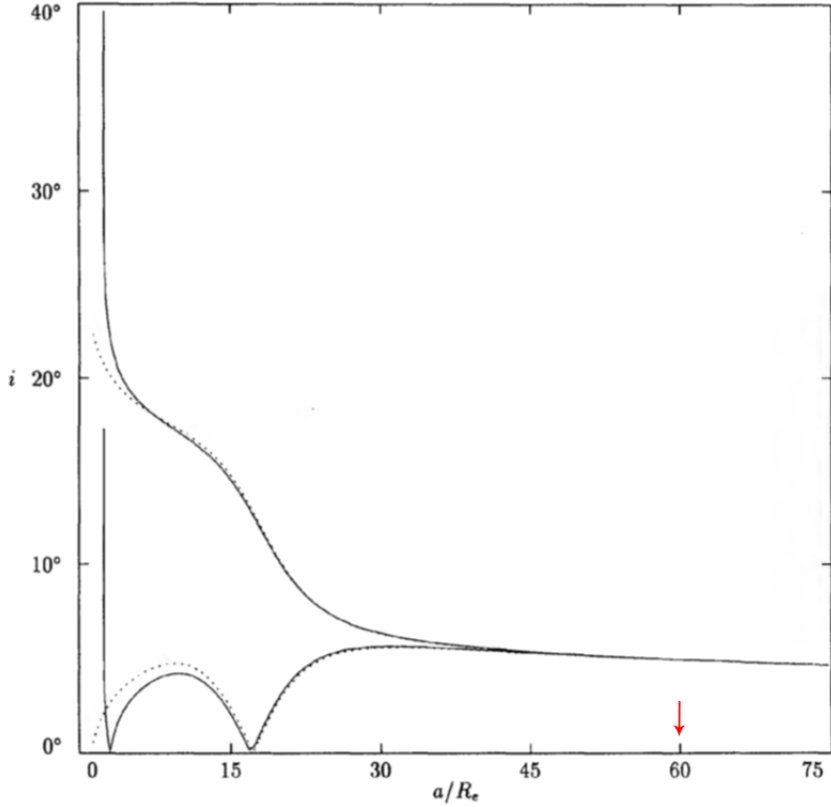
Figure 3.4: Orbital inclination vs semi-major axis expressed in Earth radii. A significant variation can be seen prior to $a_L < 33\ R_E$, after which little change occurs. Present day orbital radius shown with the red arrow. From *Touma and Wisdom* [1994].

crosses the transition frequency (closely related to the Poincaré number). In chapter 2 we concluded that FICN values below the transition frequency will result in a single Cassini state, while values greater could yield three (Fig. 2.3). But this transition frequency changes with Ω_p and Ω_0. The evolution of the Cassini states associated with the solid inner core of two models are shown in Fig. 3.6, first the model with $r_f = 350$ km, $r_s = 250$ km shown in Fig. 3.5 which features a Cassini state transition at $a_L \approx 53\ R_E$. Second, a model with $r_f = 340$ km, $r_s = 250$ km which does not undergo transition (it remains in state B). We also show in Fig. 3.6 how the transition frequency (i.e. the frequency that coincides with the merging of states A and C) has change with a_L, along with how the FICN frequency of each model has changed with a_L. The FICN frequency changes because the parameter α_g depends on Ω_0 (see Eqs. (2.18) and (2.24)). Fig. 3.6 shows
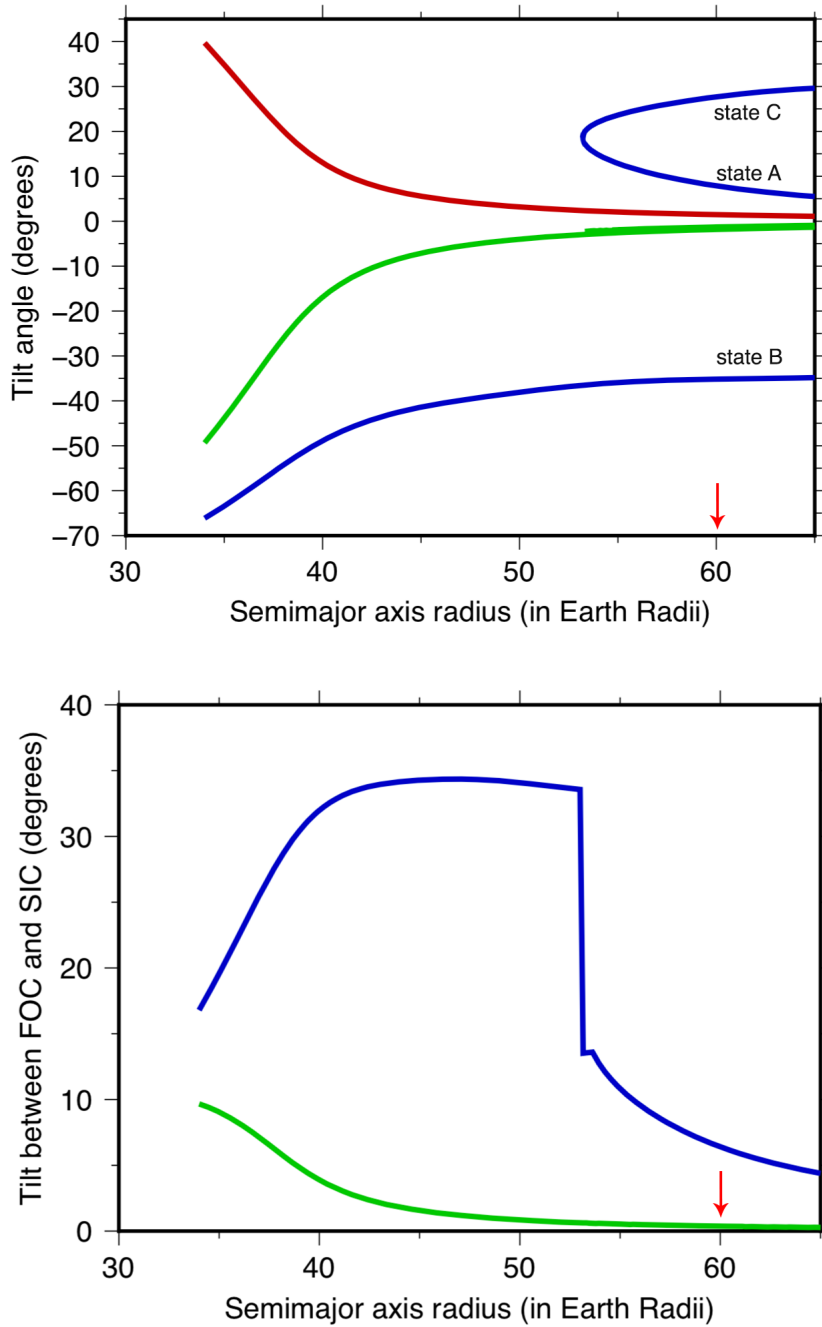
Figure 3.5: Top: The evolution of the Cassini states of a given Moon model (fluid outer core = 350 km, solid inner core = 250 km). θ_p is shown in red, θ_f in green and θ_s in blue. Bottom: The absolute angle of offset between the ecliptic normal and the spin axis of the fluid outer core (green) and the spin axis of the fluid outer core and that of the solid inner core (blue) as a function of Earth-Moon distance. Present day orbital radius shown with the red arrow.

that a transition occurs when the FICN frequency matches the transition frequency, which occurs at $a_L \approx 53$ R_E for the first model. No crossing has occurred for the second model, though one would eventually occur for $a_L > 70$ R_E.
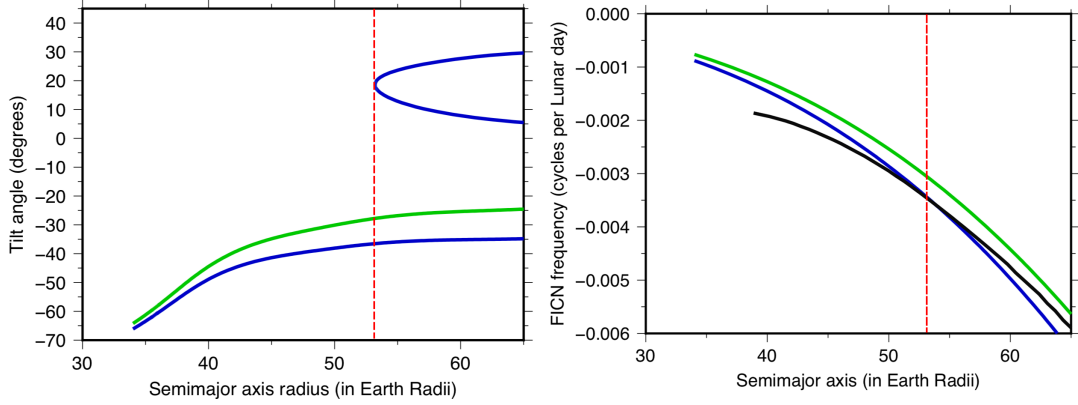

Figure 3.6: Left: Evolution of the Cassini state of the inner core for two different Lunar models, one with fluid outer core radius of 350 km (blue) and the other with an fluid outer core radius of 340 km (green), both having a solid inner core radius of 250 km. Right: Evolution of the FICN frequency (in cycles per Lunar day) for the same two models. The black curve shows the evolution of the point of merging between states A and C as a function of time. The vertical dashed red line displays the point at which the FICN frequency of the model shown in blue crosses the transition frequency (black).

These transitions can have large implications for the dissipation at the ICB. As seen in Fig. 3.6, changing Cassini states can result in a sudden change in the tilt angle of the spin axis of the inner core (from $-40°$ to $10°$), the consequences of which will be discussed further in the next section.

3.2.3 Power dissipation over Lunar history

Through Eqs. (3.18) and (3.19), the power dissipation at the CMB and ICB can be expressed as a function of semi-major axis. Let us now investigate dissipation for the same Lunar model of $r_f = 350$ km and $r_s = 250$ km, whose tilt angles evolutions are shown in Fig. 3.5. The power dissipation calculated at the CMB from this model is shown in Fig. 3.7. We also show the dissipation model by *Dwyer et al.* [2011] for comparison, which is computed from

$$Q_{cmb} \approx 3 \times 10^{20} W \times \frac{\sin^3 \theta_p}{(a_L(t)/R_E)^{(9/2)}} \ , \tag{3.21}$$

The difference between the two models originates from two sources. First, Eq. (3.21) is based on a dissipation at present day of $Q_{cmb}^{today} \approx (6.0 \pm 1.6) \times 10^7$ W which is itself derived from a viscous coupling coefficient of $\mathcal{K}/C \approx 1.122 \pm 0.257 \times 10^{-8}$ day^{-1}. Using instead the updated value of $\mathcal{K}/C$ given in Eq. (3.12) gives us a larger present day dissipation of $8.60 \pm 0.91 \times 10^7$ W. The higher dissipation from our model is due in part to this. Second, the model used in *Dwyer et al.* [2011] makes the implicit assumption that the fluid core has remained aligned with the ecliptic normal. As Fig. 3.5 (bottom) shows, the fluid core is not simply aligned with the ecliptic normal ($|\theta_f| > |\theta_p|$), in fact it is tilted in the opposite direction of the mantle slightly, resulting in an even larger angle of offset between the mantle and fluid outer core. This difference is larger the further we go back in time and explains why our dissipation values are larger.

The dynamo threshold value is described in *Dwyer et al.* [2011] as the power required to sustain an adiabat within the fluid core, below which no dynamo can exist. The threshold value (Q_{th}) has a value of 4.7×10^9 W and is shown in Fig. 3.7 as the black dashed line. The intersection between Q_{cmb} and Q_{th} occurs at about $a_L \approx 49$ R_E, or about 3 Gyr before present, depending on which temporal evolution model is used (see supplementary information, *Dwyer et al.* [2011]).

When $Q_{cmb} \leq Q_{th}$, not enough energy is present to sustain a dynamo. Hence, for the model shown in Fig. 3.7, the dynamo shuts off at $a_L \approx 49$ R_E. We also show on Fig. 3.7 the power dissipated at the ICB. Not only is dissipation at the ICB higher than the CMB for $a_L > 40$ R_E, it remains above the threshold value for a much longer period of time, therefore allowing for a much longer period of dynamo action. The sudden drop in Q_{icb} at $a_L \approx 53$ R_E is due to a transition of the Cassini state of the inner core, from state B to state A. The differential rotation is much smaller in state A than in state B, thus causing the sharp drop in Q_{icb}. Note that a large scale flow reorganization in the core may accompany this Cassini transition, which would lead to a spike in Q_{icb} (and also Q_{cmb}), before settling to the lower energy state. However, we cannot model this with our simplified description of a rigidly precessing flow.

The changes of Q_{icb} with a_L vary greatly with the choice of parameters, ultimately depending on the FICN of the system. Fig. 3.8 depicts the dissipation at the ICB of four different Lunar models, with fluid outer core radii spanning 340 to 370 km, and all sharing the same solid inner core radius of 250 km.

The difference in fluid outer core radius results in very different FICN profiles (recall that the FICN varies as a function of semi-major axis as well (Fig. 3.6)). In Fig. 3.7 we see that the solid inner core experiences a Cassini state transition at about 53 R_E. In the previous section we attributed the transition of Cassini states to the FICN of the system
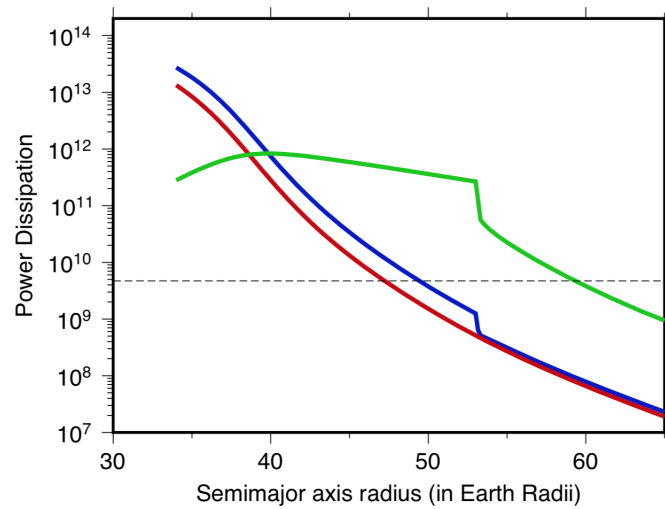
Figure 3.7: Power available to drive a dynamo estimated from viscous dissipation at the CMB (blue) and the ICB (green) as a function of semi-major axis. The dissipation at the CMB from the model presented by *Dwyer et al.* [2011] is shown in red. Lunar model with a fluid outer core and solid inner core radius of 350 km and 250 km was used, respectively. Threshold power below which dynamo will cease is shown as the black dashed line.
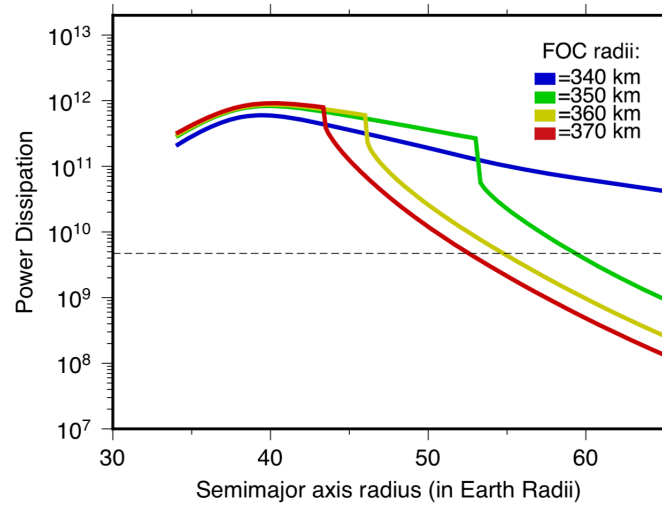
Figure 3.8: Dissipation at the ICB for multiple Lunar models, ranging in fluid outer core radius from 340 to 370 km. Solid inner core radius for all models kept at 250 km. Threshold power below which dynamo will cease is shown as the black dashed line.

becoming greater than the transition frequency (Fig. 3.6). This is precisely the cause of this rapid decline in dissipation in three of the models in Fig. 3.8. The smaller the fluid outer core radius, the later in Lunar history the transition occurs. For the model with $r_f = 340$ km, the transition has not yet occurred.

3.2.4 Paleomagnetic intensity from power dissipation

To convert dissipation into magnetic field intensity *Dwyer et al.* [2011] used a scaling law derived in *Christensen et al.* [2009], on the basis of numerical dynamo models powered by convection. This scaling may not be entirely suitable for a dynamo generated by mechanical stirring at the CMB, but no equivalent scaling law exists for precessional dynamos. It should be noted that, while heat dissipated at the CMB is not available to drive convection, heat dissipated through stirring at the ICB may be used to power a conventional thermally driven dynamo. Hence, the scaling law derived in *Christensen et al.* [2009] is more appropriate for dissipation at the ICB. We will be using the notation B_{cmb} and B_{icb} to describe the magnetic field intensity resulting from dissipation at the CMB and ICB, respectively. The conversion of power dissipation to magnetic field strength at the Lunar surface (given in micro-Teslas) is

$$B \approx 6d \left[\frac{Q_{dyn}(t)}{3 \times 10^{11}W} \right]^{1/3} , \tag{3.22}$$

where d is the ratio of the dipolar magnetic field to the total field at the CMB [*Dwyer et al.*, 2011]. For simplicity we set it equal to 1. The $Q_{dyn}(t)$ in the equation above is the dissipation readily available to power the dynamo

$$Q_{dyn} = Q_{cmb} - Q_{th} , \tag{3.23}$$

and similarly for the ICB using Q_{icb}. For values of Q_{cmb} and $Q_{icb} \leq Q_{th}$ the dynamo shuts off and magnetic field intensity would decrease to 0. Fig. 3.9 shows the predicted magnetic field strength from dissipation at the CMB and at the ICB as a function of a_L, for the different Moon models shown in Fig. 3.8.
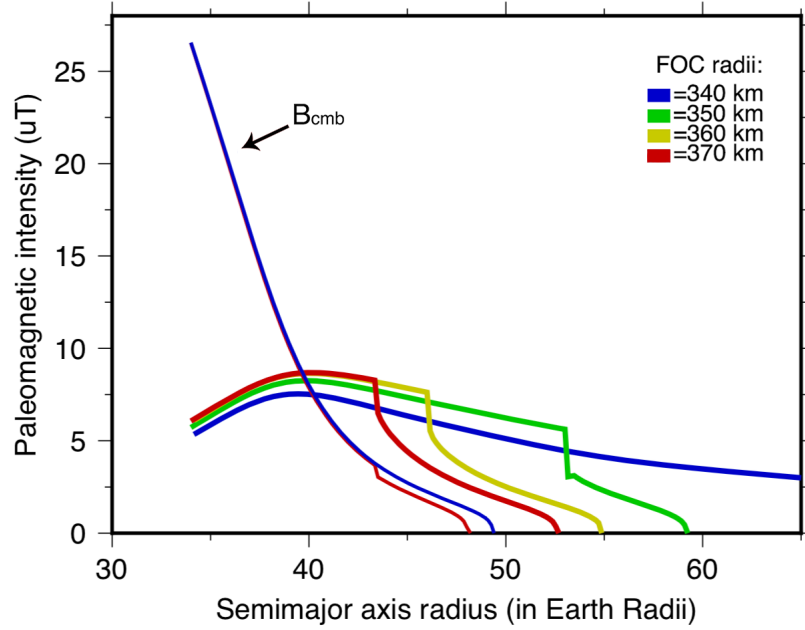

Figure 3.9: Paleomagnetic field intensities as a function of Earth-Moon distance for a range of fluid outer core (FOC in figure) radii (340-370 km). Thick coloured lines: Based on dissipation at the ICB; thin lines: B_{cmb} from viscous dissipation at the CMB (for r_f=340 and 370 km)

Dissipation at the CMB leads to a significant magnetic field, upwards of 25 μT, however it quickly becomes negligible as Q_{cmb} approaches Q_{th}. Note also that a transition in

Cassini states decreases the period of dynamo action at the CMB slightly as well, resulting in an earlier shutoff. Conversely, while not as strong as the CMB dynamo earlier in Lunar history, the dynamo at the ICB is stable for a much longer period. Supposing that the scaling law of Eq. (3.22) is appropriate, the estimates of the magnetic field strength shown in Fig. 3.9 are upper bounds because they are based on $d = 1$. The ratio of dipolar to total field at the CMB is undoubtedly smaller than 1. Since the strength of B scales linearly with d, the predictions of Fig. 3.9 would decrease in proportion with d. Furthermore, the dissipation and magnetic field strength at the ICB are shown for a large inner core radius of 250 km. Since Q_{icb} scales with r_s^5 (see Eq. (3.19)) and thus B_{icb} scales with $r_s^{5/3}$ (from Eq. (3.22)), it is clear that smaller choices of ICB radius would yield smaller Q_{icb} and B_{icb}. We need to evaluate how the size of the inner core affects the prediction of Q_{icb}, Q_{cmb}, B_{icb} and B_{cmb}, which is done in the next section.

3.2.5 Power dissipation and magnetic field intensity for different Lunar models

The previous section showed that the amplitude of the dissipation and magnetic field from differential rotation at the ICB depends sensitively on the interior Lunar model. Likewise, the Lunar model is also important for dissipation at the CMB. Let us now investigate how Q_{cmb}, Q_{icb}, B_{cmb} and B_{icb} vary for a range of interior Lunar models. We do so by focusing on three specific snapshots in Lunar history at $a_L = 33\ R_E$, $a_L = 49\ R_E$ and $a_L = 60\ R_E$.

First, as our results from the previous section show, Q_{cmb} tends to increase the further we go back in time (decreasing a_L). Therefore the maximum values of Q_{cmb} and by extension B_{cmb} would occur at the smallest a_L, which for our model is at $a_L = 33\ R_E$. Fig. 3.10 (top) shows Q_{cmb} at $a_L = 33\ R_E$ as a function of fluid outer and solid inner core radius. The dissipation at the CMB does not vary greatly as a function of r_f and r_s, staying constant at approximately 3.2×10^{13} Watts. This is mainly because θ_f does not change substantially for all combinations of r_f and r_s. A complementary way to show these results is to show how Q_{cmb} changes as a function of FICN frequency and inner core radius (Fig. 3.10 bottom). The white shaded areas mark regions where a given combination of r_s and FICN frequency would require the density of the fluid core to be higher than the inner core, or below densities that are deemed acceptable [*Matsuyama et al.*, 2016]. These would not be viable Lunar models and have therefore been neglected in our calculations. This is the way we will be presenting our models proceeding forward.

The dissipation at the ICB at $a_L = 33\ R_E$ as a function of r_s and FICN frequency is shown in Fig. 3.11. A major difference compared with Q_{cmb} is the range of change
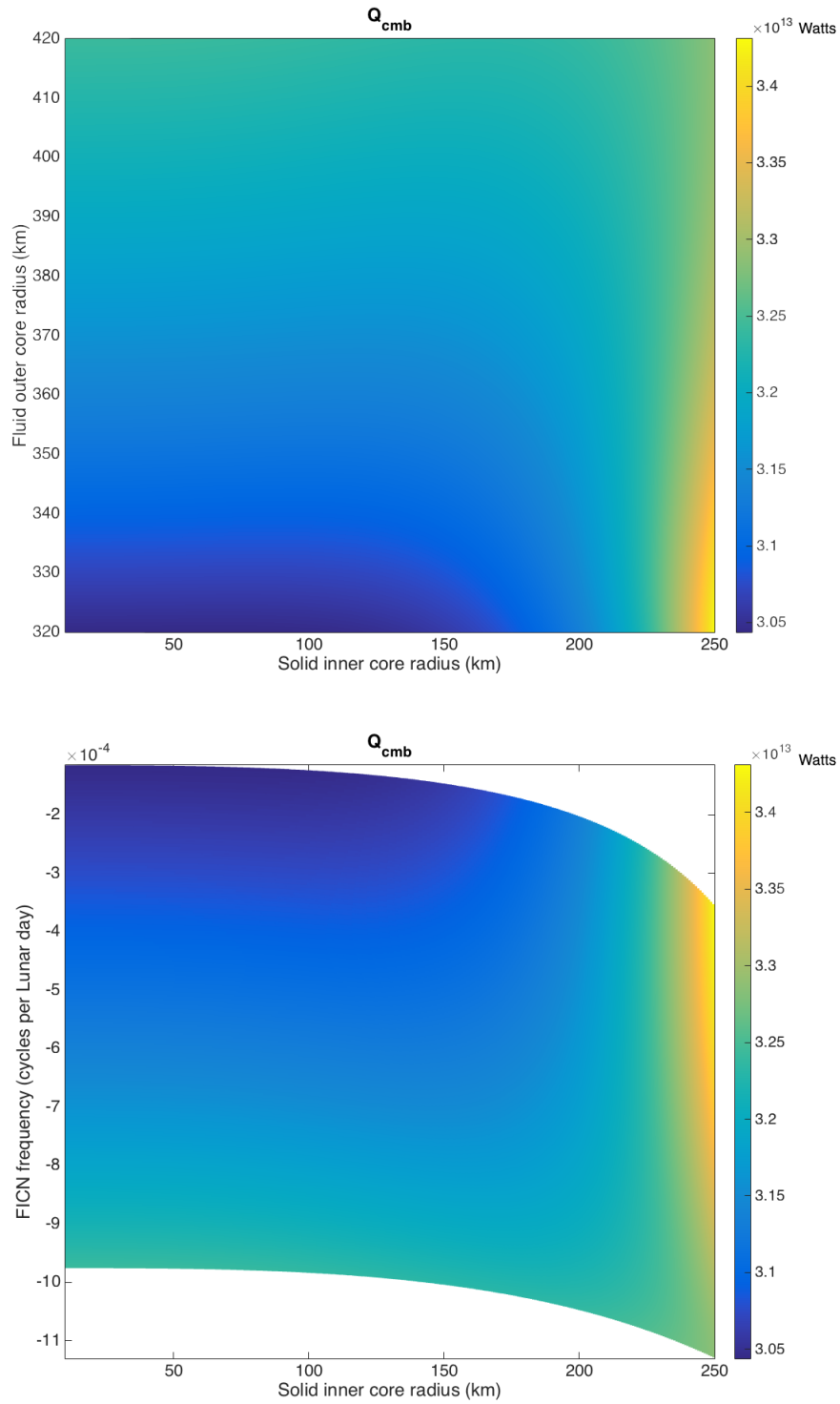
Figure 3.10: Viscous dissipation (in Watts) at the CMB at $a_L = 33\ R_E$ estimated from Eq. (3.18) as a function of r_s and r_f (top) and FICN frequency and r_s (bottom).

of Q_{icb} for different Lunar model; from approximately 10^2 to 10^{11} W. The red contour shows Q_{th}, below which a dynamo is not expected to be present, meaning that for some Lunar models dissipation is insufficient to power a dynamo. This is the case notably for $r_s \leq 120$ km. A requirement for a dynamo powered by dissipation at the ICB is thus that the inner core radius must be larger than ≈ 120 km.
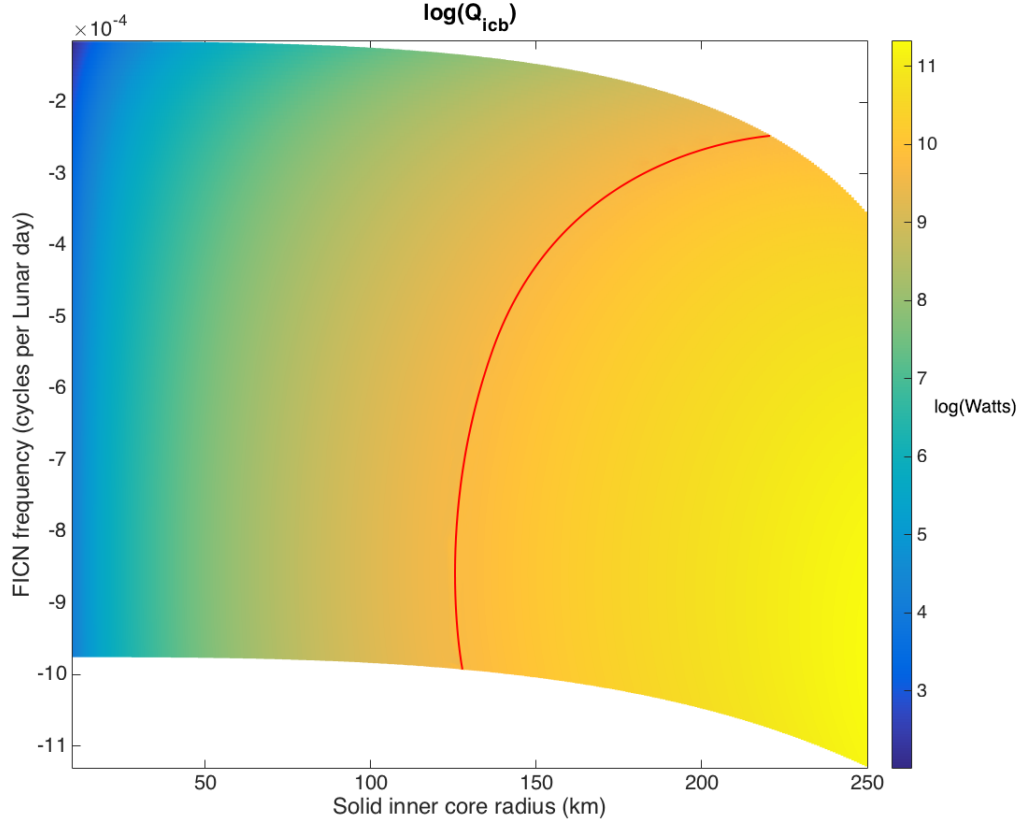

Figure 3.11: Viscous dissipation (in Watts) at the ICB at $a_L = 33 \ R_E$ estimated from Eq. (3.19) as a function of FICN frequency and r_s. $Q_{th} = 4.7 \times 10^9$ W is shown by the red line.

The corresponding magnetic fields from both Figs. 3.10 and 3.11 are shown in Fig. 3.12. As expected (and shown in Fig. 3.7), the magnetic field intensity generated at the CMB is invariably larger than that at the ICB, with values ranging from about 28 to 29.2 μT. In regions of the parameter space where Q_{icb} is below Q_{th}, the predicted magnetic intensity falls to zero. When it is above, the magnetic field intensity can be as high as 5.3 μT. For all interior Lunar models at $a_L = 33 \ R_E$, the inner core is in Cassini state B.
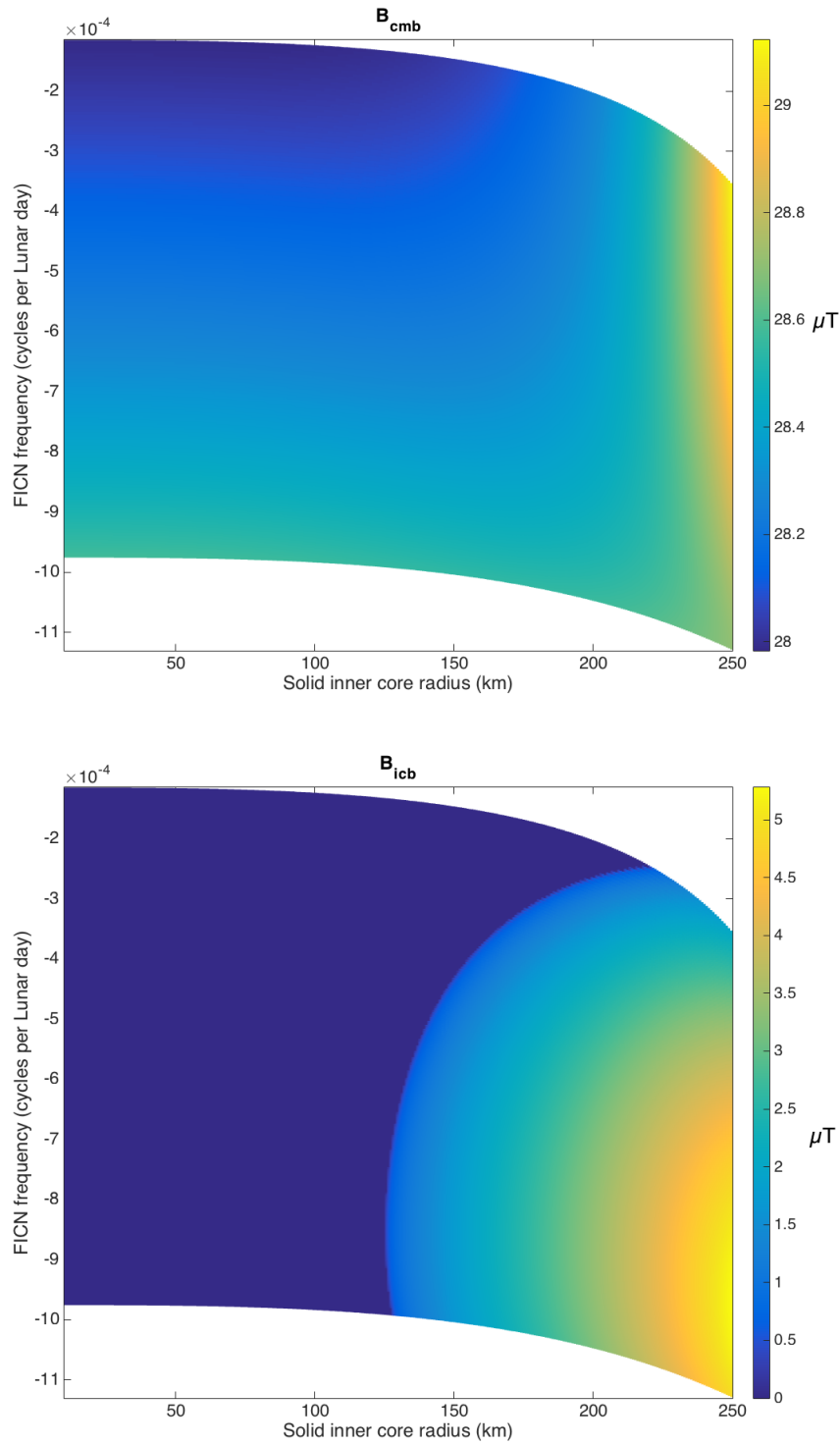
Figure 3.12: Magnetic field intensities (in μT) at $a_L = 33\ R_E$ estimated from Eq. (3.22) as a function of FICN frequency and r_s, from dissipation at the CMB (top) and ICB (bottom).

The next epoch that we investigate is right after the cessation of the dynamo from dissipation at the CMB, at $a_L = 49$ R_E. For all Lunar models at this epoch, Q_{cmb} is below Q_{th}. Fig. 3.13 shows how Q_{icb} and the corresponding magnetic field intensity, B_{icb}, vary with FICN frequency and r_s.

Two major differences between B_{icb} at $a_L = 33$ and 49 R_E are immediately discernible. First, the magnitude of the magnetic field has increased from a maximum of 5.8 μT at $a_L = 33$ R_E to a maximum of 6.3 μT at 49 R_E. This is due to the fact that the angle of offset between the fluid outer core and the solid inner core is larger at $a_L = 49$ R_E. The second difference is the narrower parameter space of models for which dynamo action is possible. In particular, only models for which the FICN frequency is between approximately -1.6×10^{-3} to -3.5×10^{-3} are above threshold.

For completeness we also include a model of Q_{icb} and B_{icb} at $a_L = 60$ R_E, representing the current state of the Lunar system. Again, $Q_{cmb} < Q_{th}$ for every Lunar model at this epoch. Predictably, Q_{icb} and B_{icb} at $a_L = 60$ R_E follow the same pattern as the two previous epochs. The magnitude of the maximum magnetic field has decreased to 4.1 μT, and the region of parameter space of dynamo above threshold has narrowed, further restricted to $r_s \geq 150$ km and FICN frequencies between -3.7×10^{-3} and -4.4×10^{-3}. However there is still a range of models that allow for dynamo action today, more specifically models for which the inner core remains in Cassini state B (Fig. 3.6) and have a higher differential velocity at the ICB.

3.3 Discussion: Mechanical stirring as a source of dynamo action

We have shown that the magnetic field strength estimated from viscous dissipation at the CMB may have been as high as 25-29 μT when $a_L = 33$ R_E. The precise amplitude depends on the interior Lunar model. This estimate is slightly larger than predicted in *Dwyer et al.* [2011] (closer to 20 μT) and this is for two reasons. First, we used an updated and slightly larger estimate of the dissipation in the present-day Moon. Second, we take into account in our model the fact that the spin axis of the fluid core is not aligned with the ecliptic but further misaligned from the mantle axis by as much as $\approx 10°$ at $a_L = 33$ R_E (Fig. 3.5, bottom). Though the choice of interior model affects the amplitudes of the magnetic field and when dynamos may have shut off, the dependence is weak and for all Lunar models, B_{cmb} has shut off by $a_L = 49$ R_E.

The novel contribution from our study concerns the contribution of a similar estimate of a magnetic field but from a dynamo powered by viscous dissipation at the ICB. We
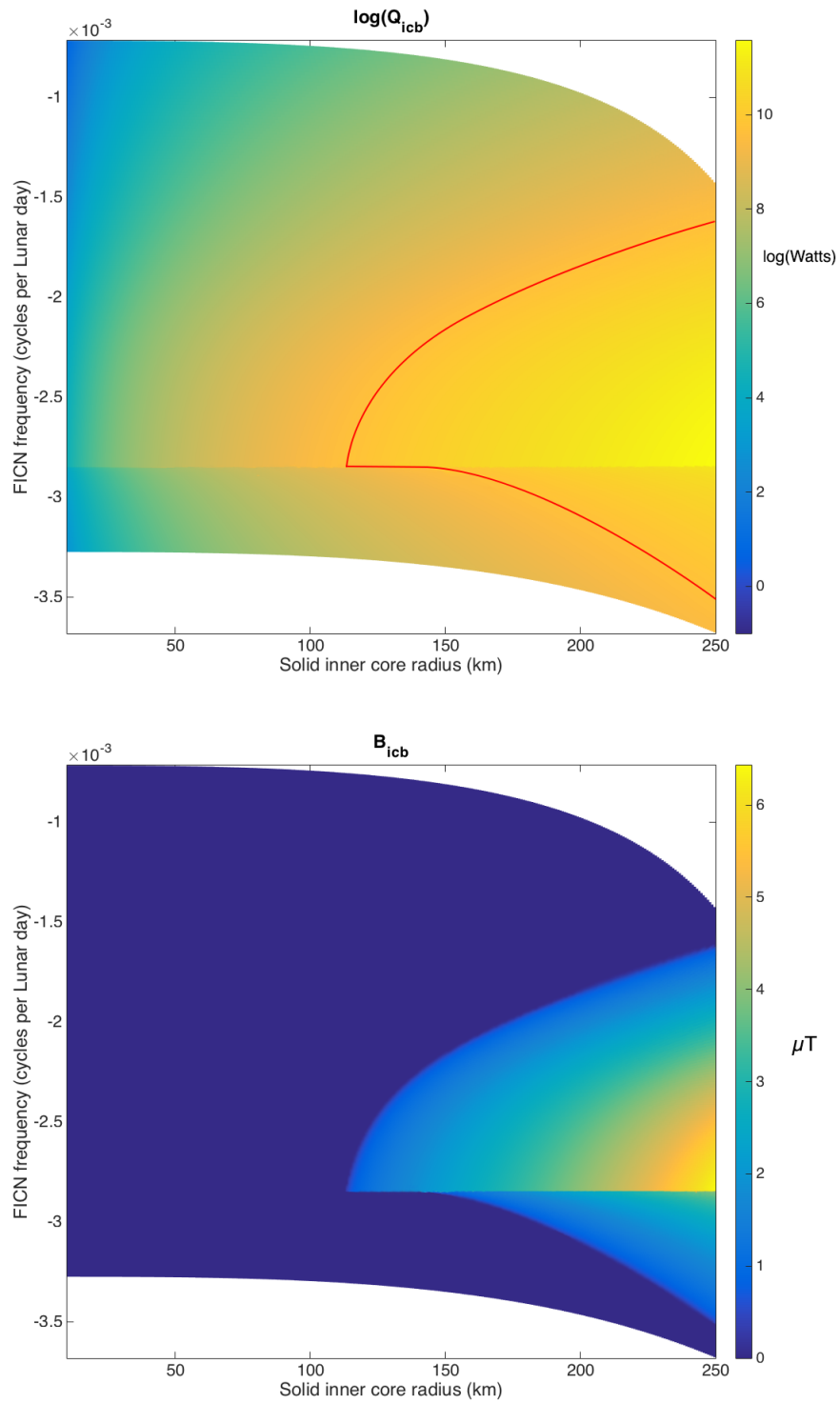
Figure 3.13: Viscous dissipation at the ICB (top in Watts), B_{icb} (bottom, in μT) at $a_L = 49\ R_E$ as a function of FICN frequency and r_s.
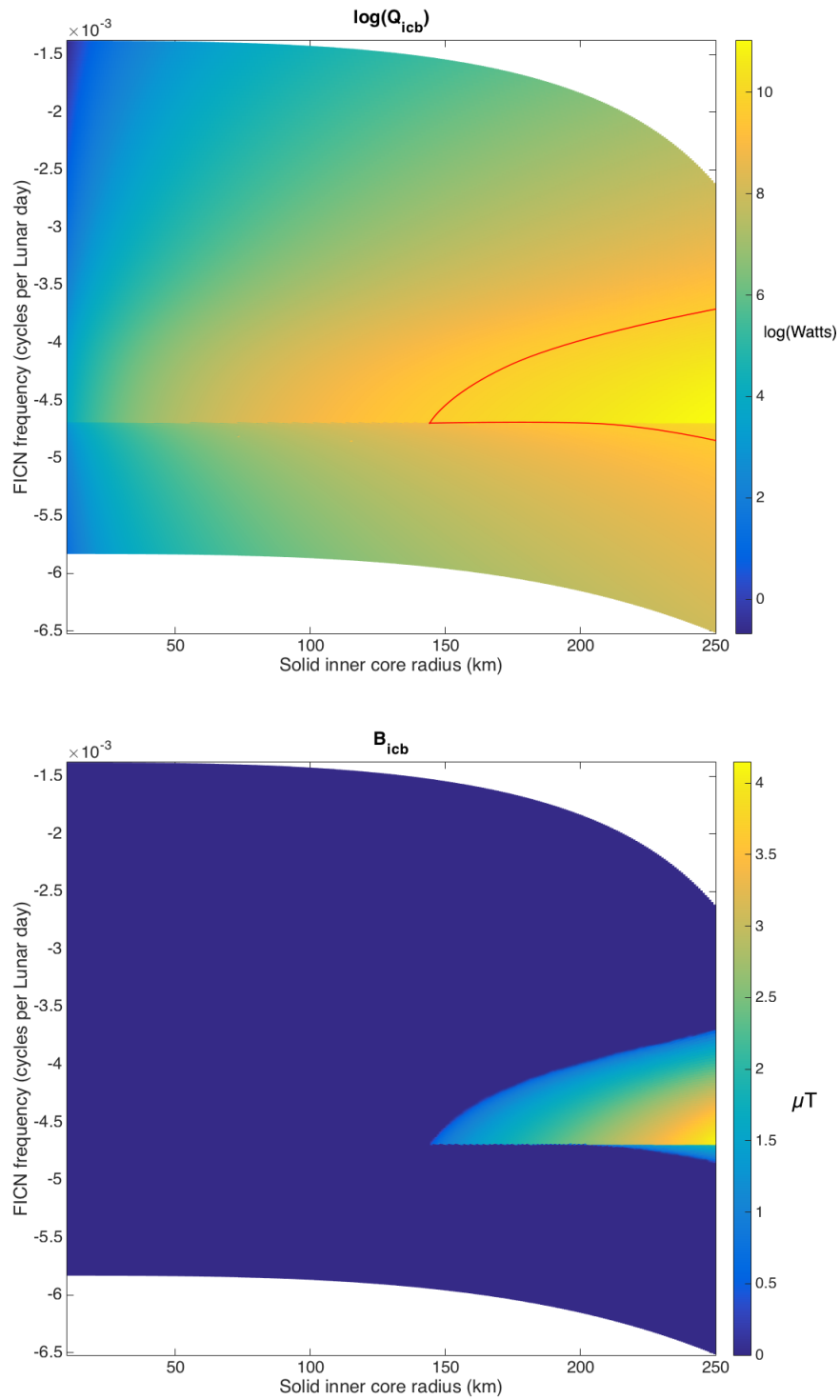
Figure 3.14: Viscous dissipation at the ICB (top in Watts), B_{icb} (bottom, in μT) at $a_L = 60~R_E$ as a function of FICN frequency and r_s.

have shown that whether the dissipation is above the threshold depends sensitively on the Cassini state of the inner core. Furthermore, we have shown that a transition of the Cassini state associated with the inner core may have occurred as the Lunar orbit evolved, marking a significant and sudden transition from a high energy state (state B), to a low energy state (state A) (Fig. 3.5 top). Whether a Cassini state transition occurred depends on the evolution of the FICN frequency relative the the transition frequency, as discussed in the previous section (Fig. 3.6). For all plausible Lunar models, the solid inner core inhabited the higher energy state as the system progressed further back in time, which was tilted opposite to the spin-symmetry axis of the mantle.

The largest amplitudes of magnetic field predicted by our model are of the order of 8.5 μT, which occur at $a_L \approx 40$ R_E. Though smaller than B_{cmb}, it can persist for much longer. The two main criteria for dissipation at the ICB to be above the dynamo threshold are: one, the inner core must be larger than approximately 100 km; two, the inner core must be in Cassini state B (although it is possible to be above threshold in state A, the field amplitudes are weaker).

The amplitude of B_{icb} was also found to be very dependent on the Lunar model chosen. Models that feature a Cassini transition reached higher peak paleomagnetic intensities but died off earlier due to the transition to a lower energy state. Meanwhile, models that did not exhibit a transition stayed on the same state (Fig. 3.6), resulting in the paleointensity to slowly decay over time, keeping above the threshold dissipation (Q_{th}) for a long period of time. Even at present there are models that could theoretically sustain a magnetic field generated at the ICB, with an intensity of up to 3.7 μT. The fact that the Moon does not have an on-going dynamo implies then that: one, the inner core radius is smaller than than 150 km; or, two, that the FICN frequency for the present day Moon does not fall between -3.7×10^{-3} and -4.9×10^{-3}. However, if the FICN frequency is outside but close to this interval and if $r_s > 150$ km, a Lunar dynamo powered by precession at the ICB may have shut down only very recently. Hence it is possible that such a dynamo may be responsible for the longevity of the Lunar magnetic field (Fig. 1.6). The amplitude of the magnetic field that we predict are consistent with the paleomagnetic intensities of the order of 5-10 μT at the Lunar surface that persist after 3 Gyr on Fig. 1.6 [*Weiss and Tikoo*, 2014]. Though this is encouraging, we need to recall that these are obtained while making the assumption that all the magnetic energy is being used in the dipole component. More realistically, only a fraction of the magnetic energy is in the dipole field, and our estimates should be then reduced by the same fraction.

Accordingly, this suggests that differential motion at the ICB cannot generate sufficient

energy to explain the field intensities in the Lunar paleomagnetic data. However, we need to remember that our magnetic field estimates only takes into account the heat dissipated at the ICB which is then available to power a convective dynamo. In addition to this, the precession motion of an elliptical inner core will generate flow by mechanical stirring. If such flows lead to global instabilities and large scale eddies [*Lin et al.*, 2016], they may contributed to dynamo action. If so, the magnetic field produced as a result of differential motion at the ICB may be larger than we have estimated.

Further complicating the picture is the fact that, once a magnetic field is present in the Lunar core, electromagnetic coupling at the ICB will act to reduce the differential rotation between the fluid and solid cores (DW16). On one hand, this will reduce the differential rotation at the ICB and thus reduce the viscous dissipation, reducing the energy available to power a dynamo and the resulting magnetic field. On the other hand, dissipation associated with the electromagnetic torque would likely be much larger than that from viscous torque. Hence, for the same angle of differential rotation, it would deposit a larger amount of heat at the ICB. Taking into account the reduction in the differential rotation that electromagnetic coupling would entail, it is unclear whether this would lead to larger or smaller dissipation at the ICB and thus the magnetic intensity estimates.

As shown by *Dwyer et al.* [2011] and further illustrated in our study, viscous dissipation at the CMB alone fails to explain the largest paleomagnetic intensities inferred from Lunar rocks. The addition of the magnetic field generated from viscous dissipation at the ICB could help supplement B_{cmb} in the early stages. Although the largest values we get from B_{icb} are of the order of 10 μT, added to B_{cmb} it could explain many of the data points seen between 4-3 Gyr in Fig. 1.6. But the more impactful result of our study is that we have shown that dissipation at the ICB could explain the peculiar long lasting Lunar dynamo, with intensities on the order of 5-10 μT well beyond 3 Gyr, up to nearly present day. The narrowing parameter space of Lunar models which predicts a dynamo with time can explain why there is no dynamo generated field on the Moon at present.

We have neglected inner core growth from crystallization in our study, however this is not entirely correct. The radius of the solid inner core should increase as a function of time. The precise history of the inner core growth depends among other things on the initial composition of the fluid core and on the evolution of the heat flux at the CMB [eg. *Laneuville et al.*, 2014]. The shortest Earth-Moon distance in our study, $a_L = 33$ R_E, should correspond to approximately 4 Gyr before present, possibly before the inner core had started nucleating. Taking inner core growth into account, the amplitude of the magnetic field on Fig. 3.9 should be weaker for smaller Earth-Moon distances, and

null before the ICB radius got larger than ≈ 100 km. On the one hand, this implies that the largest magnetic field predictions from our model at $a_L \approx 40$ R_E, are likely much smaller, and dynamo action from dissipation at the ICB may only have started once a_L was larger than 40 R_E. On the other hand, if the gap in paleomagnetic intensities in Fig. 1.6 between 1.5 and 3 Gyr before present reflect the absence of Lunar dynamo in that time interval, perhaps the late Lunar dynamo after 1.5 Gyr ago reflects when the inner core reached critical size to power a precession dynamo at the ICB.

Chapter 4

Conclusions

In the second chapter of this study we have shown that:

- The tilt angle of the inner core of the Moon can reach large angles even at present-day (upwards of 10°).

- The rotational dynamics of the mantle are influenced by the Cassini states of the fluid core, and the inner core to a lesser extent.

- The Cassini states of the inner core ultimately depend on ω_{ficn}, the frequency of the FICN.

- The orbital inclination influences the shape of the Cassini states of the solid inner core. Orbital tilt angles larger than 0° will increase the FICN frequency at which the transition occurs.

- As a result of tidal dissipation, the inner core would most likely inhabit the Cassini state with the smallest absolute angle of offset.

- Predictions from this model may be used in conjunction with gravitational data in order to further constrain the size of the solid inner core.

.

In the third chapter we have shown that:

- The dissipation at the CMB due to viscous torque arising from differential velocity was very high in the distant past ($a_L = 33$ R_E) however decreased as the fluid core and mantle became more aligned.

- The dissipation at the ICB is dependent on whether the inner core undergoes a Cassini state transition through the evolution of the Earth-Moon system, which is ultimately dependent on the FICN frequency.

- Models with smaller fluid outer core radii tend to stay in the higher energy Cassini state for longer periods of time, thus displaying higher power dissipation for longer.

- B_{cmb} can reach relatively high values, of nearly 30 μT, however die off at around $a_L = 49 \ R_E$.

- B_{icb} reaches a maximum of 8.5 μT and can stay active for a much longer period of time.

- Variation in Lunar interior parameters does not have a large effect on B_{cmb}, however is very significant in B_{icb}.

- Many Lunar models do not permit dynamo action at the ICB, even at $a_L = 33 \ R_E$, however there are still models today that allow for dynamo action.

- It is possible for mechanical stirring at the ICB to explain the long lasting, low intensity paleomagnetic observations seen in Fig. 1.6.

Future research:

- Include elastic deformation and viscous relaxation in our Cassini state model in order to more accurately calculate Cassini states.

- Investigate further the melting and solidification cycle of the tilted inner core.

- Allow for changes in I in order to extend the dynamo model further into the past.

- Study the consequences of a Cassini state transition on the fluid dynamics of the fluid outer core.

- Apply electromagnetic coupling to our initial Cassini state model, which could significantly impact the Cassini state evolution. Electromagnetic coupling could also be an important source of dissipation in order to power a dynamo.

- Apply our Cassini state model to other planets or the icy shell satellites of other planets in order to provide insight into the precession dynamics of these bodies.

Appendix A

Description of the Lunar orbit, rotation and references frames used in our model

The Moon is rotating around Earth on an eccentric orbit inclined by an angle $I = 5.145°$ with respect to the ecliptic plane. This orbital plane is precessing about the ecliptic normal in a retrograde direction with a frequency of $\Omega_p = 2\pi/18.6$ yr^{-1}. To describe the position of the Moon as it orbits about the Earth, we define a coordinate system attached to the inertial reference frame, centred on Earth, and specified by unit vectors $(\hat{e}_1, \hat{e}_2, \hat{e}_3)$. Direction $\hat{e}_3$ is aligned with the normal to the ecliptic. The normal to the orbital plane, defined by a normal unit vector $\hat{e}_3^I$, is then precessing about $\hat{e}_3$ at frequency $-\Omega_p$.

As shown in Fig. A.1a, the position of the Moon is described by an angle F, the mean angle from the orbit's ascending node, and by an angle Ω, the longitude of the ascending node with respect to $\hat{e}_1$. The rate of change of Ω is related to the precession frequency by $\frac{d\Omega}{dt} = -\Omega_p$. The time it takes for the Moon to complete one orbit with respect to the inertial frame is defined as the sidereal period and is equal to 27.322 days. The sidereal frequency is equal to the mean motion, $n = 2\pi/27.322$ day^{-1}. Since the Moon is in a tidally locked 1:1 spin-orbit resonance, the rate of the Moon's rotation around itself averaged over one orbit is closely related to n, though not exactly equal, as we develop below.

Because the orbit is precessing, the Moon does not return to the same point in inertial space after one sidereal period. The time it takes for the Moon to return to the ascending node of the orbit is slightly shorter than the sidereal period, and is equal to 27.212 days. Defining this orbital frequency by $\Omega_c = 2\pi/27.212$ day^{-1}, the mean rate of change of F averaged over one orbit is related to Ω_c by $\frac{dF}{dt} = \Omega_c$. The mean motion is linked to Ω_c and Ω_p by $n = \Omega_c - \Omega_p$.

The half-period modulation of the gravitational torque by Earth over one orbit and the eccentricity of the orbit lead to small latitudinal and longitudinal librations of the
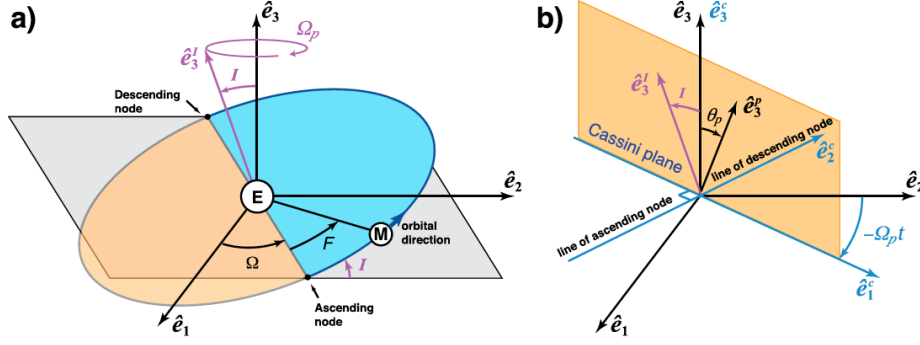
Figure A.1: a) The orbit of the Moon (M) around Earth (E) as seen in the inertial frame $(\hat{e}_1, \hat{e}_2, \hat{e}_3)$. The normal to the orbital plane is defined by $\hat{e}_3^I$ and is offset from $\hat{e}_3$ by an angle $I = 5.145°$. $\hat{e}_3^I$ precesses about $\hat{e}_3$ in a retrograde direction at frequency $\Omega_p = 2\pi/18.6$ yr^{-1}. F is the mean angle from the orbit's ascending node. Ω is the longitude of the ascending node with respect to $\hat{e}_1$. The blue (orange) shaded region indicates portions of the orbit when the Moon is above (below) the ecliptic plane, the latter being represented by the grey shade. b) The Cassini frame $(\hat{e}_1^c, \hat{e}_2^c, \hat{e}_3^c)$ is rotating at frequency $-\Omega_p$ about $\hat{e}_3 = \hat{e}_3^c$ with respect to the inertial frame, with $\hat{e}_2^c$ aligned with the line of the descending node. The symmetry axis of the mantle $\hat{e}_3^p$ is offset from $\hat{e}_3$ by $\theta_p = 1.543°$. Both $\hat{e}_3^I$ and $\hat{e}_3^p$ remain in the Cassini plane, the plane defined by $\hat{e}_1^c$ and $\hat{e}_3^c$ delimited by the orange shaded region. a) and b) do not correspond to the same snapshot in time.

Moon in space. These are neglected in our study, as we focus on the long timescale equilibrium described by the Cassini state. In other words, in the description of the Cassini state that follows, even when not specifically stated, we always consider quantities that are averaged over one orbit.

The Moon is in a Cassini state, which describes the fact that the symmetry axis (defined by a unit vector $\hat{e}_3^p$), though inclined by $\theta_p = 1.543°$ with respect to $\hat{e}_3$, remains co-planar with both $\hat{e}_3$ and $\hat{e}_3^I$. The plane containing all three vectors is rotating with frequency $-\Omega_p$ about $\hat{e}_3$ with respect to the inertial frame. This description is only valid when the orientation of $\hat{e}_3^p$ is averaged over one orbit, which is assumed in our discussion. To describe the Cassini state, it is convenient to introduce a second reference frame which we refer to as the Cassini frame. The Cassini frame is specified by unit vectors $(\hat{e}_1^c, \hat{e}_2^c, \hat{e}_3^c)$, with $\hat{e}_3^c$ aligned with the ecliptic normal $(\hat{e}_3^c = \hat{e}_3)$, and is rotating with frequency $-\Omega_p$ about $\hat{e}_3$ with respect to the inertial frame (Fig. A.1b). The orientation

of the Cassini frame is chosen such that direction $\hat{e}_2^c$ remains aligned with the line of the descending node of the orbit on the ecliptic plane. It is convenient to place the origin of the Cassini frame at the centre of the Moon. Setting an alignment $\hat{e}_1^c = \hat{e}_2$ at time $t = 0$, the relationship between the Cassini and inertial reference frames is expressed by

$$\hat{e}_1^c = \quad \sin(-\Omega_p t)\hat{e}_1 \ + \ \cos(-\Omega_p t)\hat{e}_2 \,, \tag{A.1a}$$

$$\hat{e}_2^c = -\cos(-\Omega_p t)\hat{e}_1 \ + \ \sin(-\Omega_p t)\hat{e}_2 \,, \tag{A.1b}$$

$$\hat{e}_3^c = \quad \hat{e}_3 \,. \tag{A.1c}$$

As viewed in the Cassini frame, both the direction of the orbit normal $\hat{e}_3^I$ and the symmetry axis $\hat{e}_3^p$ remain at fixed positions. It is convenient to refer to the plane defined by $\hat{e}_1^c$ and $\hat{e}_3^c$ as the "Cassini plane" (Fig. A.1b). Because the Moon possesses a fluid and (most likely) a solid core, formally $\hat{e}_3^p$ represents the symmetry axis of the mantle only. The orientation of the symmetry axis of the inner core, denoted by $\hat{e}_3^s$ also lies on the Cassini plane, and also remains at a fixed position in the Cassini frame (see Fig. 2.1a of the main text).

We define the rotation vector of the Moon's mantle by $\boldsymbol{\Omega}$. The vector $\boldsymbol{\Omega}$ also lies on the Cassini plane, though it is not aligned exactly with the symmetry axis $\hat{e}_3^p$ but is offset by a small angle θ_m (see Fig. 2.1b of the main text). To preserve a synchronous rotation, $\boldsymbol{\Omega}$ as seen in the Cassini frame is given by

$$\boldsymbol{\Omega} = \Big[-\Omega_p + \Omega_c \cos(\theta_p) \Big]\hat{e}_3^c + \Omega_c \sin(\theta_p)\, \hat{e}_1^c \,, \tag{A.2}$$

and, upon using Eqs. (A.1), by

$$\boldsymbol{\Omega} = \Big[-\Omega_p + \Omega_c \cos(\theta_p) \Big]\hat{e}_3 + \Omega_c \sin(\theta_p)\Big[\sin(-\Omega_p t)\hat{e}_1 + \cos(-\Omega_p t)\hat{e}_2 \Big] \,. \tag{A.3}$$

when seen in the inertial frame.

The model of the rotational dynamics of the Moon that we develop in the main text is defined with respect to a reference frame attached to the rotating mantle. We must then express how this reference frame is connected to the inertial and Cassini frames defined above. Let us define the mantle frame by unit vectors $(\hat{e}_1^p, \hat{e}_2^p, \hat{e}_3^p)$. We have already defined $\hat{e}_3^p$ to be aligned with the maximum (polar) moment of inertia of the mantle. $\hat{e}_1^p$ and $\hat{e}_2^p$ are aligned, respectively, with the minimum and intermediate moments of inertia (both in equatorial directions). As seen in the Cassini frame, although $\hat{e}_3^p$ remains at

a fixed orientation, $\hat{e}_1^p$ and $\hat{e}_2^p$ are time-dependent because the Moon is rotating about itself. This is depicted in Figs. 2.1a,b of the main text.

As seen in the Cassini frame, the time it takes for $\hat{e}_1^p$ and $\hat{e}_2^p$ to complete one full rotation must coincide with the time it takes for these vectors to return to the same alignment with respect to Earth. In other words, the rate of rotation of $\hat{e}_1^p$ and $\hat{e}_2^p$ about $\hat{e}_3^p$ is equal to the orbital frequency Ω_c.

Setting an alignment $\hat{e}_2^p = \hat{e}_2^c$ at time $t = 0$, the time-dependent orientation of the mantle axes as seen in the Cassini frame is expressed by

$$\hat{e}_1^p = \quad \cos(\theta_p)\cos(\Omega_c t)\hat{e}_1^c \; + \; \sin(\Omega_c t)\hat{e}_2^c \; - \; \sin(\theta_p)\cos(\Omega_c t)\hat{e}_3^c \,, \tag{A.4a}$$

$$\hat{e}_2^p = -\cos(\theta_p)\sin(\Omega_c t)\hat{e}_1^c \; + \; \cos(\Omega_c t)\hat{e}_2^c \; + \; \sin(\theta_p)\sin(\Omega_c t)\hat{e}_3^c \,, \tag{A.4b}$$

$$\hat{e}_3^p = \quad \cos(\theta_p)\hat{e}_3^c \; + \; \sin(\theta_p)\hat{e}_1^c \,. \tag{A.4c}$$

Using Eqs. (A.1), the time-dependent orientation of the mantle axes as seen in the inertial frame is expressed by

$$
\begin{aligned}
\hat{e}_1^p = & \; \Big[\cos(\theta_p)\cos(\Omega_c t)\sin(-\Omega_p t) \; - \; \sin(\Omega_c t)\cos(-\Omega_p t)\Big]\hat{e}_1 \\
& + \Big[\cos(\theta_p)\cos(\Omega_c t)\cos(-\Omega_p t) \; + \; \sin(\Omega_c t)\sin(-\Omega_p t)\Big]\hat{e}_2 \\
& - \sin(\theta_p)\cos(\Omega_c t)\hat{e}_3 \,,
\end{aligned}
\tag{A.5a}
$$

$$
\begin{aligned}
\hat{e}_2^p = & \; \Big[-\cos(\theta_p)\sin(\Omega_c t)\sin(-\Omega_p t) \; - \; \cos(\Omega_c t)\cos(-\Omega_p t)\Big]\hat{e}_1 \\
& + \Big[-\cos(\theta_p)\sin(\Omega_c t)\cos(-\Omega_p t) \; + \; \cos(\Omega_c t)\sin(-\Omega_p t)\Big]\hat{e}_2 \\
& + \sin(\theta_p)\sin(\Omega_c t)\hat{e}_3 \,,
\end{aligned}
\tag{A.5b}
$$

$$\hat{e}_3^p = \quad \sin(\theta_p)\Big[\sin(-\Omega_p t)\hat{e}_1 + \cos(-\Omega_p t)\hat{e}_2\Big] + \cos(\theta_p)\hat{e}_3 \,. \tag{A.5c}$$

The reverse relationships, the time-dependent direction of the inertial frame as seen in the mantle frame, is expressed by

$$\hat{e}_1 = \left[\cos(\theta_p) \cos(\Omega_c t) \sin(-\Omega_p t) - \sin(\Omega_c t) \cos(-\Omega_p t) \right] \hat{e}_1^p$$
$$+ \left[-\cos(\theta_p) \sin(\Omega_c t) \sin(-\Omega_p t) - \cos(\Omega_c t) \cos(-\Omega_p t) \right] \hat{e}_2^p$$
$$+ \sin(\theta_p) \sin(-\Omega_p t) \hat{e}_3^p , \tag{A.6a}$$

$$\hat{e}_2 = \left[\cos(\theta_p) \cos(\Omega_c t) \cos(-\Omega_p t) + \sin(\Omega_c t) \sin(-\Omega_p t) \right] \hat{e}_1^p$$
$$+ \left[-\cos(\theta_p) \sin(\Omega_c t) \cos(-\Omega_p t) + \cos(\Omega_c t) \sin(-\Omega_p t) \right] \hat{e}_2^p$$
$$+ \sin(\theta_p) \cos(-\Omega_p t) \hat{e}_3^p , \tag{A.6b}$$

$$\hat{e}_3 = \sin(\theta_p) \left[-\cos(\Omega_c t) \hat{e}_1^p + \sin(\Omega_c t) \hat{e}_2^p \right] + \cos(\theta_p) \hat{e}_3^p . \tag{A.6c}$$

The relationships of Eqs. (A.5-A.6) allow one to express any vectorial quantity defined in the inertial frame in its equivalent form as seen in the mantle frame, or vice-versa. In particular, the rotation vector of the mantle $\mathbf{\Omega}$ is defined in the inertial frame by Eq. (A.3). Using Eqs. (A.6), we can express how $\mathbf{\Omega}$ changes as a function of time, as seen in the frame attached to the mantle. Using standard trigonometric identities, it is straightforward (although somewhat tedious) to show that

$$\mathbf{\Omega} = \left[\Omega_c - \Omega_p \cos(\theta_p) \right] \hat{e}_3^p + \Omega_p \sin(\theta_p) \left[\cos(\Omega_c t) \hat{e}_1^p - \sin(\Omega_c t) \hat{e}_2^p \right]. \tag{A.7}$$

Although we have used a different notation, this latter expression is equivalent to Eq. (1) of *Eckhardt* [1981] when an exact Cassini state is maintained. For an observer fixed to the mantle frame, the orientation of the rotation vector $\mathbf{\Omega}$ is offset from the figure axis $\hat{e}_3^p$ and precesses about the latter in a retrograde direction at frequency Ω_c. Let us define Ω_o as the amplitude of the rotation vector given by

$$\Omega_o = |\mathbf{\Omega}| = \left[\Omega_c^2 + \Omega_p^2 - 2\Omega_c \Omega_p \cos(\theta_p) \right]^{1/2}. \tag{A.8}$$

Since $\Omega_c \gg \Omega_p$, to a good approximation, we can write

$$\Omega_o \approx \Omega_c - \Omega_p \cos(\theta_p). \tag{A.9}$$

Defining θ_m as the angle of offset between $\mathbf{\Omega}$ and $\hat{e}_3^p$, we can write Eq. (A.7) as

$$\mathbf{\Omega} = \Omega_o \cos(\theta_m) \hat{e}_3^p + \Omega_o \sin(\theta_m) \hat{e}_\perp^p(t) , \tag{A.10}$$

where the vector $\hat{e}_\perp^p(t)$ is given by

$$\hat{e}_{\perp}^{\boldsymbol{p}}(t) = \left[\cos(\omega\Omega_o t)\hat{e}_{\boldsymbol{1}}^{\boldsymbol{p}} + \sin(\omega\Omega_o t)\hat{e}_{\boldsymbol{2}}^{\boldsymbol{p}} \right]. \tag{A.11}$$

and where the frequency ω, expressed in units of cycles per Lunar day, is defined as

$$\omega = -\frac{\Omega_c}{\Omega_o} = -1 - \cos(\theta_p)\frac{\Omega_p}{\Omega_o}. \tag{A.12}$$

The unit vector $\hat{e}_{\perp}^{\boldsymbol{p}}(t)$ expresses the rotation at frequency $\omega\Omega_o$ of the orientation of $\boldsymbol{\Omega}$ about $\hat{e}_{\boldsymbol{3}}^{\boldsymbol{p}}$ as seen by an observer in the mantle frame. As ω is negative, the rotation is retrograde. Since $\boldsymbol{\Omega}$ is in the Cassini plane, $\hat{e}_{\perp}^{\boldsymbol{p}}(t)$ describes more generally the retrograde rotation about $\hat{e}_{\boldsymbol{3}}^{\boldsymbol{p}}$ of the longitude of the Cassini plane as seen by an observer in the mantle frame, and is depicted in Figs. 2.1c,d of the main text. Furthermore, it is easy to show that

$$\hat{e}_{\boldsymbol{3}}^{\boldsymbol{p}} \times \hat{e}_{\perp}^{\boldsymbol{p}}(t) = \left[-\sin(\omega\Omega_o t)\hat{e}_{\boldsymbol{1}}^{\boldsymbol{p}} + \cos(\omega\Omega_o t)\hat{e}_{\boldsymbol{2}}^{\boldsymbol{p}} \right], \tag{A.13a}$$

$$\frac{d}{dt}\hat{e}_{\perp}^{\boldsymbol{p}}(t) = \omega\Omega_o\left[-\sin(\omega\Omega_o t)\hat{e}_{\boldsymbol{1}}^{\boldsymbol{p}} + \cos(\omega\Omega_o t)\hat{e}_{\boldsymbol{2}}^{\boldsymbol{p}} \right], \tag{A.13b}$$

where the time derivative is taken in the mantle frame, and therefore we can write

$$\frac{d}{dt}\hat{e}_{\perp}^{\boldsymbol{p}}(t) = \omega\Omega_o\left(\hat{e}_{\boldsymbol{3}}^{\boldsymbol{p}} \times \hat{e}_{\perp}^{\boldsymbol{p}}(t) \right). \tag{A.13c}$$

Note that the direction of the vector $\hat{e}_{\boldsymbol{3}}^{\boldsymbol{p}} \times \hat{e}_{\perp}^{\boldsymbol{p}}(t)$ is perpendicular to the Cassini plane, towards $\hat{e}_{\boldsymbol{2}}^{\boldsymbol{c}}$ (see Fig. 2.1 of the main text).

The rotation vectors of the fluid core ($\boldsymbol{\Omega_f}$) and inner core ($\boldsymbol{\Omega_s}$) can be defined similarly. They also remain at fixed orientations when viewed in the Cassini frame (see Fig. 2.1b of the main text) and are also precessing at frequency $\omega\Omega_o = -\Omega_c$ when seen by an observer in the mantle frame. The development used above for the mantle can be used identically for the inner core, with the orientation of the inner core's symmetry axis (with respect to the ecliptic normal) given by $\theta_p + \theta_n$ and the orientation of its rotation vector (with respect to the mantle frame) given by $\theta_m + \theta_s$. The fluid core does not need to remain in synchronous rotation, but we can represent its rotation rate in a similar manner. Although it does not have a symmetry axis per say, we can use $\theta_m + \theta_f$ to represent the orientation of both its rotation vector and symmetry axis with respect to the mantle frame to develop an expression for its rotation vector. The rotation vectors of the fluid core and inner core are then

$$\mathbf{\Omega_f} = \Omega_o^f \cos(\theta_m + \theta_f)\hat{\boldsymbol{e}}_{\mathbf{3}}^{\boldsymbol{p}} + \Omega_o^f \sin(\theta_m + \theta_f)\hat{\boldsymbol{e}}_{\perp}^{\boldsymbol{p}}(t) \,, \tag{A.14a}$$

$$\mathbf{\Omega_s} = \Omega_o^s \cos(\theta_m + \theta_s)\hat{\boldsymbol{e}}_{\mathbf{3}}^{\boldsymbol{p}} + \Omega_o^s \sin(\theta_m + \theta_s)\hat{\boldsymbol{e}}_{\perp}^{\boldsymbol{p}}(t) \,, \tag{A.14b}$$

with

$$\Omega_o^f \approx \Omega_c - \Omega_p \cos(\theta_p + \theta_m + \theta_f) \,, \tag{A.14c}$$

$$\Omega_o^s \approx \Omega_c - \Omega_p \cos(\theta_p + \theta_n) \,. \tag{A.14d}$$

Note that the amplitude of rotation of the mantle, fluid core and inner core are not equal to one another. However, their amplitude differ by no more than the Poincaré number given by the ratio $\Omega_p/\Omega_c = 4.022 \times 10^{-3}$, and except for very large values of θ_n, their difference is typically much smaller than that. Thus, to a good approximation, we can set $\Omega_o^f \approx \Omega_o^s \approx \Omega_o$, in the definition of our rotation vectors, which simplifies the mathematical development of our model.

Appendix B

The Cassini state in the inertial frame

As seen in the inertial frame $(\hat{\boldsymbol{e}}_1, \hat{\boldsymbol{e}}_2, \hat{\boldsymbol{e}}_3)$ defined in Appendix A, the angular momentum equation describing the rotational dynamics of a single-body Moon is expressed by

$$\frac{d}{dt}\boldsymbol{H} = \boldsymbol{\Gamma} \tag{B.1}$$

where $\boldsymbol{H}$ is the angular momentum of the whole Moon and $\boldsymbol{\Gamma}$ is the gravitational torque from Earth. Assuming a negligible misalignment between the rotation vector and the maximum (polar) principal moment of inertia C, we can write $\boldsymbol{H} = C\boldsymbol{\Omega}$, where $\boldsymbol{\Omega}$ is the rotation vector of the single-body Moon, given by Eq. (A.3). Taking the time derivative of $\boldsymbol{H}$ yields

$$\frac{d}{dt}\boldsymbol{H} = -C\Omega_c\Omega_p \sin(\theta_p)\Big[\cos(-\Omega_p t)\hat{\boldsymbol{e}}_1 - \sin(-\Omega_p t)\hat{\boldsymbol{e}}_2\Big]. \tag{B.2}$$

Focusing, as we do throughout our study, on the long time scale equilibrium, the gravitational torque by Earth averaged over one orbit is in the same direction as the time-derivative of $\boldsymbol{H}$ and is given by

$$\boldsymbol{\Gamma} = -n^2(\Phi_\beta^p \bar{A}\beta + \Phi_\gamma^p \bar{A}\gamma)\Big[\cos(-\Omega_p t)\hat{\boldsymbol{e}}_1 - \sin(-\Omega_p t)\hat{\boldsymbol{e}}_2\Big], \tag{B.3}$$

where we have used Eqs. (2.16b) and (2.20) of the main text, without the inner core contribution. Setting Eqs. (B.2) and (B.3) equal to one another, we find

$$C\frac{\Omega_p \Omega_c}{n^2}\sin(\theta_p) = \Phi_\beta^p \bar{A}\beta + \Phi_\gamma^p \bar{A}\gamma. \tag{B.4}$$

Since $n = \Omega_c - \Omega_p$ and $\Omega_p \ll \Omega_c$, we can approximate $\Omega_c/n \approx 1$, and we retrieve (in our notation) the condition on θ_p given in Eq. (19) of *Peale* [1969] that defines the Cassini state of a single body Moon

$$C\frac{\Omega_p}{n}\sin(\theta_p) = \Phi^p_\beta \bar{A}\beta + \Phi^p_\gamma \bar{A}\gamma. \tag{B.5}$$

By following a similar procedure, we can construct an expression for the Cassini state of the solid inner core of the Moon. As seen in the inertial frame, the angular momentum of the inner core ($\boldsymbol{H_s}$) obeys

$$\frac{d}{dt}\boldsymbol{H_s} = \boldsymbol{\Gamma_s} \tag{B.6}$$

where $\boldsymbol{\Gamma_s}$ is the total torque on the inner core. Once more assuming a negligible misalignment between the rotation vector $\boldsymbol{\Omega_s}$ and the maximum (polar) principal moment of inertia C_s, we can write $\boldsymbol{H_s} = C_s\boldsymbol{\Omega_s}$. The rotation vector of the inner core is given by an expression analogous to Eq. (A.3) but also includes the tilt of the inner core figure θ_n with respect to the mantle,

$$\boldsymbol{\Omega_s} = \Big[-\Omega_p + \Omega_c\cos(\theta_p+\theta_n)\Big]\boldsymbol{\hat{e}_3} + \Omega_c\sin(\theta_p+\theta_n)\Big[\sin(-\Omega_p t)\boldsymbol{\hat{e}_1} + \cos(-\Omega_p t)\boldsymbol{\hat{e}_2}\Big]. \tag{B.7}$$

Taking the time derivative of $\boldsymbol{H_s}$ yields

$$\frac{d}{dt}\boldsymbol{H_s} = -C_s\Omega_c\Omega_p\sin(\theta_p+\theta_n)\Big[\cos(-\Omega_p t)\boldsymbol{\hat{e}_1} - \sin(-\Omega_p t)\boldsymbol{\hat{e}_2}\Big]. \tag{B.8}$$

Using Eqs. (2.17b) and (2.20), and the approximation $\Omega_o \approx n$, the torque on the inner core is

$$\boldsymbol{\Gamma_s} = -n^2\bar{A}_s\Big(\ \Phi^n_\beta\beta_s\alpha_3\ +\ \Phi^n_\gamma\gamma_s\alpha_3\ +\ e_s\alpha_3\alpha_g\sin(\theta_n)\cos(\theta_n)$$
$$-\ e_s\alpha_1\sin(\theta_n+\theta_p)\cos(\theta_n+\theta_p)\Big)\cdot\Big[\cos(-\Omega_p t)\boldsymbol{\hat{e}_1} - \sin(-\Omega_p t)\boldsymbol{\hat{e}_2}\Big], \tag{B.9}$$

where we have assumed $\theta_m + \theta_f = -\theta_p$, the latter corresponding to a fluid core rotation vector aligned with the ecliptic normal. Setting Eq. (B.8) equal to Eq. (B.9) yields

$$\frac{C_s}{\bar{A}_s}\frac{\Omega_p\Omega_c}{n^2}\sin(\theta_p+\theta_n) =$$
$$\Phi^n_\beta\beta_s\alpha_3\ +\ \Phi^n_\gamma\gamma_s\alpha_3\ +\ e_s\alpha_3\alpha_g\sin(\theta_n)\cos(\theta_n)\ -\ e_s\alpha_1\sin(\theta_n+\theta_p)\cos(\theta_n+\theta_p). \tag{B.10}$$

The first two terms on the right-hand side of Eq. (B.10) capture the gravitational torque from Earth averaged over one orbit; they involve products of sines and cosines

of $(I + \theta_p + \theta_n)$ (see Eq. 2.20). The third and fourth terms capture, respectively, the gravitational torque that the rest of the Moon exert on the inner core and the pressure torque from the misaligned rotation vectors of the fluid and solid cores at the ICB. For a given I and θ_p, Eq. (B.10) gives the condition that the tilt angle θ_n must obey in order for the inner core to precess about the ecliptic normal at the same rate as the Lunar orbit. In other words, it represents the balance that determines the Cassini state of the inner core of the Moon.

In the present-day Moon, the internal torque from the mantle and fluid core on the inner core dominates the gravitational torque from Earth. Setting $\Phi_\beta^n = \Phi_\gamma^n = 0$ in Eq. (B.10) and, since θ_n is typically much larger than $\theta_p = 1.543°$ (see Fig. 2.3), we can use the following approximation

$$\sin(\theta_n + \theta_p)\cos(\theta_n + \theta_p) \approx \sin(\theta_n)\cos(\theta_n), \tag{B.11}$$

which allows to simplify Eq. (B.10) to

$$\frac{C_s}{\bar{A}_s}\frac{\Omega_p}{n}\sin(\theta_p + \theta_n) = -\omega_{ficn}\sin(\theta_n)\cos(\theta_n), \tag{B.12}$$

where ω_{ficn} is the frequency of the FICN given by Eq. (2.24) and where we have removed a factor $\Omega_c/n \approx 1$ on the left-hand side. Since the dynamical ellipticity of the inner core is small, $C_s \approx \bar{A}_s$, the tilt angle θ_n in the Cassini state of the inner core depends on the interior structure only insofar as it affects the FICN frequency; different interior density models of the Moon that have the same FICN frequency will have the same tilt angle θ_n.

Bibliography

Araki, H., S. Tazawa, H. Noda, Y. Ishihara, S. Goossens, and S. Saski, Lunar global shape and polar topography derived from Kaguya-LALT laser altimetry, *Science*, *323*, 897–900, 2009.

Cameron, A. G. W., and B. G. Marsden, *The Earth-Moon system*, Plenum Press, 1966.

Canup, R. M., Forming a Moon with an Earth-like composition via a giant impact, *Science*, *338*, 1052–1054, 2012.

Canup, R. M., and E. Asphaug, Origin of the Moon in a giant impact near the end of the Earth's formation, *Nature*, *412*, 708–712, 2001.

Cébron, D., R. Laguerre, J. Noir, and N. Schaeffer, Precessing spherical shells: flows, dissipation, dynamo and the Lunar core, *Geophysical Journal International*, 2018.

Chamberlin, T. C., and F. R. Moulton, The development of the planetesimal hypothesis, *Science*, *30*, 642–645, 1909.

Chapront-Touzé, M., and J. Chapront, The Lunar ephemeris, *Astronomy and Astrophysics*, *124*, 50–62, 1983.

Christensen, U. R., V. Holzwarth, and A. Reiners, Energy flux determines magnetic field strength of planets and stars, *Nature*, *457*, 167–169, 2009.

Cuk, M., and S. T. Stewart, Making the Moon from a fast-spinning Earth: a giant impact followed by resonant despinning, *Science*, *338*, 1047–1052, 2012.

Darwin, G. H., A tidal theory of the evolution of satellites, *The observatory*, *3*, 79–84, 1879.

Dickey, J. O., et al., Lunar Laser Ranging: A continuing legacy of the Apollo program, *Science*, *265*, 482–490, 1994.

Dumberry, M., and M. A. Wieczorek, A forced precession of the Moon's inner core, *Journal of geophysical research*, *121*, 1264–1292, 2016.

Dwyer, C. A., D. J. Stevenson, and F. Nimmo, A long-lived lunar dynamo driven by continuous mechanical stirring, *Nature*, *479*, 212–215, 2011.

Eckhardt, D. H., Theory of the librations of the Moon, *Moon and the Planets*, *25*, 3–49, 1981.

Garcia, R. F., J. G. Beyneix, S. Chevrot, and P. Lognonné, Very preliminary reference Moon model, *Physics of the Earth and planetary interiors*, *118*, 96–113, 2011.

Harada, Y., S. Goossens, K. Matsumoto, J. Yan, J. Ping, H. Noda, and J. Haruyama, Strong tidal heating in an ultralow-viscosity zone at the core-mantle boundary of the Moon, *Nature Geoscience*, *7*, 569–572, 2014.

Hartmann, W. K., and D. R. Davis, Satellite-sized planetesimals and Lunar origin, *Icarus*, *24*, 504–515, 1975.

Heiken, G. H., D. T. Vaniman, and B. M. French, *Lunar sourcebook*, Press Syndicate of the University of Cambridge, 1991.

Jeffreys, H., The resonance theory of the origin of the Moon, *Monthly notices of the royal astronomical society*, *91*, 169–174, 1930.

Jones, C. A., Thermal and compositional convection in the outer core, *Treatise on Geophysics*, 2015.

Kipp, M. E., and H. J. Melosh, Origin of the Moon: a preliminary numberical study of colliding planets, *Lunar and planetary science*, *17*, 420–421, 1986.

Konrad, W., and T. Spohn, Thermal history of the Moon: Implications for an early core dynamo and post-accretional magmatism, *Advances in space research*, *19*, 1511–1521, 1997.

Laneuville, M., M. A. Wieczorek, D. Breuer, J. Aubert, G. Morard, and T. Ruckriemen, A long-lived Lunar dynamo powered by core crystallization, *Earth and Planetary sceicen letters*, *401*, 251–260, 2014.

Lin, Y., P. Marti, J. Noir, and A. Jackson, Precession-driven dynamos in a full sphere and the role of large cyclonic vortices, *Physics of fluids*, *28*, 2016.

Malkus, W. V. R., Precession of the Earth as a cause of Geomagnetism, *Science*, *160*, 259–264, 1968.

Mathews, P. M., and J. Y. Guo, Viscoelectromagnetic coupling in precession-nutation theory, *Journal of geophysical research*, *110*, 1–16, 2005.

Mathews, P. M., B. A. Bufffett, T. A. Herring, and I. I. Shapiro, Forced nutations of the Earth: Influence on inner core dynamics, *Journal of geophysical research*, *96*, 8219–8242, 1991.

Matsuyama, I., F. Nimmo, J. T. Keane, N. H. Chan, G. J. Taylor, M. A. Wieczorek, W. S. Kiefer, and J. G. Williams, GRAIL, LLR, and LOLA constraints on the interior structure of the Moon, *Geophysical Research Letters*, *43*, 8365–8375, 2016.

Meyer, J., and J. Wisdom, Precession of the Lunar Core, *Icarus*, *211*, 921–924, 2011.

Munhemezulu, C., L. Combrinck, and J. O. Botai, A review of the lunar laser ranging technique and contribution of timing systems, *South african journal of science*, *112*, 1–9, 2016.

Nimmo, F., Thermal and compositional evolution of the core, *Treatise on Geophysics*, 2015.

Peale, S. J., Generalized Cassini's laws, *The astronomical journal*, *74*, 483–489, 1969.

Peale, S. J., Excitation and relaxation of the wobble, precession and libration of the Moon, *Journal of geophysical research*, *81*, 1813–1827, 1974.

Pedlosky, J., An inertial theory of equatorial undercurrent, *Journal of physical oceanography*, *17*, 1978–1985, 1987.

Petrova, N., A. Gusev, N. Kawano, and H. Hanada, Free librations of te two-layer Moon and the possibilities of their detection, *Advances in space research*, *42*, 1398–1404, 2008.

Rogister, Y., and B. Valette, Influence of liquid core dynamics on rotational modes, *Geophysical Journal International*, *176*, 368–388, 2009.

Runcorn, S. K., An ancient Lunar magnetic dipole field, *Nature*, *253*, 701–703, 1975.

Smith, D. E., M. T. Zuber, G. A. Neumann, F. G. Lemoine, E. Mazarico, and M. H. Torrence, Initial observations from the Lunar Orbiter Laser Altimeter (LOLA), *Geophysical Research Letters*, *37*, 1–6, 2010.

Stegman, D. R., A. M. Jellinek, S. A. Zatman, J. R. Baumgardner, and M. A. Richards, An early lunar dynamo driven by thermochemical mantle convection, *Nature*, *421*, 143–146, 2003.

Stys, C., and M. Dumberry, The Cassini state of the Moon's inner core, *Journal of geophysical research*, 2018.

Tilgner, A., Precession driven dynamos, *Physics of fluids*, *17*, 1–6, 2005.

Tilgner, A., Rotational dynamics of the core, *Treatise on Geophysics*, 2015.

Touma, J., and J. Wisdom, Evolution of the Earth-Moon system, *The astronomical journal*, *108*, 1943–1961, 1994.

Van Hoolst, T., and V. Dehant, Influence of triaxiality and second-order terms in flattenings on the rotation of terrestrial planets, *Physics of the Earth and planetary interiors*, *134*, 17–33, 2002.

Ward, W. R., Past orientation of the Lunar spin axis, *Science*, *189*, 377–379, 1975.

Weber, R. C., P. Y. Lin, E. J. Garnero, Q. Williams, and P. Lognonné, Seismic detection of the Lunar core, *Science*, *331*, 309–312, 2011.

Weiss, B. P., and S. M. Tikoo, The Lunar dynamo, *Science*, *346*, 1246,753, 2014.

Wieczorek, M. A., et al., The constitution and structure of the Lunar interior, *Review in mineralogy and geochemistry*, *60*, 221–364, 2006.

Williams, G. E., Geological constraints on the precambrian history of the Earth's rotation and the Moon's orbit, *Reviews of Geophysics*, *38*, 37–59, 2000.

Williams, J. G., A scheme for Lunar inner core detection., *Geophysical Research Letters*, *34*, 2007.

Williams, J. G., The deep lunar interior from GRAIL, *In 46th Lunar and planetary conference*, 2015.

Williams, J. G., and J. O. Dickey, Lunar geophysics, geodesy and dynamics, *13th international workshop on laser ranging*, 2002.

Williams, J. G., D. H. Boggs, C. F. Yoder, J. T. Ratcliff, and J. O. Dickey, Lunar rotational dissipation in solid body and molten core, *Journal of geophysical research*, *106*, 27,933–27,968, 2001.

Williams, J. G., A. S. Boggs, C. F. Yoder, J. T. Ratcliff, and J. O. Dickey, Lunar interior properties from the GRAIL mission, *Journal of geophysical research*, *119*, 1546–1578, 2014.

Wise, D. U., An origin of the Moon by rotational fission during formation of the Earth's core, *Journal of geophysical research*, *68*, 1547–1554, 1963.

Yoder, C. F., The free librations of a dissipative Moon, *Philosophical transactions of the royal society*, *303*, 327–338, 1981.

Zuber, M., D. Smith, D. Lehman, T. Hoffman, S. Asmar, and M. Watkins, Gravity recovery and interior laboratory (GRAIL): mapping the lunar interior from crust to core, *Space Science Reviews*, *178*, 1–22, 2013.